

AWARD NUMBER: W81XWH-15-1-0728

TITLE: MYC RNAi-Pt Combination Nanotherapy for Metastatic Prostate Cancer Treatment

PRINCIPAL INVESTIGATOR: Dr. Jinjun Shi

CONTRACTING ORGANIZATION: Brigham and Women's Hospital

REPORT DATE: Dec 2019

TYPE OF REPORT: Final Report

PREPARED FOR: U.S. Army Medical Research and Development Command  
Fort Detrick, Maryland 21702-5012

DISTRIBUTION STATEMENT: Approved for Public Release;  
Distribution Unlimited

The views, opinions and/or findings contained in this report are those of the author(s) and should not be construed as an official Department of the Army position, policy or decision unless so designated by other documentation.

REPORT DOCUMENTATION PAGE				Form Approved OMB No. 0704-0188	
Public reporting burden for this collection of information is estimated to average 1 hour per response, including the time for reviewing instructions, searching existing data sources, gathering and maintaining the data needed, and completing and reviewing this collection of information. Send comments regarding this burden estimate or any other aspect of this collection of information, including suggestions for reducing this burden to Department of Defense, Washington Headquarters Services, Directorate for Information Operations and Reports (0704-0188), 1215 Jefferson Davis Highway, Suite 1204, Arlington, VA 22202-4302. Respondents should be aware that notwithstanding any other provision of law, no person shall be subject to any penalty for failing to comply with a collection of information if it does not display a currently valid OMB control number. <b>PLEASE DO NOT RETURN YOUR FORM TO THE ABOVE ADDRESS.</b>					
1. REPORT DATE Dec 2019		2. REPORT TYPE Final		3. DATES COVERED 30 Sep 2015 – 29 Sep 2019	
4. TITLE AND SUBTITLE MYC RNAi-Pt Combination Nanotherapy for Metastatic Prostate Cancer Treatment				5a. CONTRACT NUMBER	
				5b. GRANT NUMBER W81XWH-15-1-0728	
				5c. PROGRAM ELEMENT NUMBER	
6. AUTHOR(S) Omid Farokhzad (initiating PI), Angelo De Marzo (partnering PI), Charles Bieberich (partnering PI), Srinivasan Yegnashubramanian (co-I), Jinjun Shi (co-I, interim initiating PI)  E-Mail: ofarokhzad@bwh.harvard.edu; jshi@bwh.harvard.edu				5d. PROJECT NUMBER	
				5e. TASK NUMBER	
				5f. WORK UNIT NUMBER	
7. PERFORMING ORGANIZATION NAME(S) AND ADDRESS(ES)  Brigham and Women's Hospital, Boston, MA 02115  The Johns Hopkins University School of Medicine, Baltimore, MD 21205  University of Maryland, Baltimore County, Baltimore, MD 21250				8. PERFORMING ORGANIZATION REPORT NUMBER	
9. SPONSORING / MONITORING AGENCY NAME(S) AND ADDRESS(ES)  U.S. Army Medical Research and Development Command Fort Detrick, Maryland 21702-5012				10. SPONSOR/MONITOR'S ACRONYM(S)	
				11. SPONSOR/MONITOR'S REPORT NUMBER(S)	
12. DISTRIBUTION / AVAILABILITY STATEMENT  Approved for Public Release; Distribution Unlimited					
13. SUPPLEMENTARY NOTES					
14. ABSTRACT The main objective of this project is to develop an innovative nanotherapy modality by combining platinum (Pt) chemotherapy and MYC-targeting RNA interference (RNAi) for more effective treatment of metastatic prostate cancer (PCa). Over the entire period of this project, we made significant accomplishments in each of the proposed tasks. We successfully developed, characterized, and optimized a reduction-responsive nanoparticle (NP) platform for effective delivery of siRNA and cisplatin prodrug. The siMYC NPs and siMYC-Pt NPs were extensively tested in vitro using different PCa cell lines including Pt-resistant cells, and the combination nanotherapy showed potent anti-tumor efficacy in subcutaneously xenografted PCa mouse model without obvious in vivo toxicities. We also established and characterized the phenotypic features of murine cell lines derived from sites of metastasis of <i>B13<sup>MYC/Cre</sup> Pten<sup>fl/fl</sup></i> (BMPC) genetically engineered mouse (GEM) model, which were used for in vitro and RNAseq studies to assess whether the MYC signature is being modulated in the BMPC mice and cell lines. In the BMPC GEM model, the siRNA NPs were able to accumulate in the prostate tumor tissues and silencing MYC expression after intravenous injection. We further determined the anti-tumor efficacy of siMYC NPs, cisplatin prodrug NPs, and siMYC-Pt NPs in BMPC GEM mice, which demonstrated significant anti-tumor efficacy, leading to a quantifiable reduction in tumor burden.					
15. SUBJECT TERMS Nanotechnology, nanoparticle, siRNA delivery, platinum, MYC, prostate cancer, drug resistance, mouse model, pathology, genomics					
16. SECURITY CLASSIFICATION OF:			17. LIMITATION OF ABSTRACT  Unclassified	18. NUMBER OF PAGES	19a. NAME OF RESPONSIBLE PERSON USAMRMC
a. REPORT Unclassified	b. ABSTRACT Unclassified	c. THIS PAGE Unclassified			19b. TELEPHONE NUMBER (include area code)

## TABLE OF CONTENTS

	<u>Page</u>
1. Introduction	4
2. Keywords	5
3. Accomplishments	6
4. Impact	15
5. Changes/Problems	16
6. Products	17
7. Participants & Other Collaborating Organizations	18
8. Special Reporting Requirements	21
9. Appendices	22

## 1. INTRODUCTION

The main objective of this project is to develop an innovative nanotherapy modality by combining platinum (Pt) chemotherapy and MYC-targeting RNA interference (RNAi) for more effective treatment of metastatic prostate cancer (PCa). Two specific aims are proposed in this study, including (i) development and optimization of MYC siRNA-Pt nanoparticles (NPs), and (2) determination of the efficacy of select NPs in the *B13<sup>MYC/Cre</sup>|Pten<sup>fl/fl</sup>* engineered PCa mouse model. This project is directed by an interdisciplinary team in the PCa research field, including Initiating PI Dr. Omid Farokhzad from Brigham and Women's Hospital (BWH)/Harvard Medical School (HMS), Partnering PIs Dr. Charles Bieberich from the University of Maryland Baltimore County (UMBC) and Dr. Angelo De Marzo from the John Hopkins University (JHU), and two co-investigators (Dr. Srinivasan Yegnasubramanian from JHU and Dr. Jinjun Shi from BWH/HMS). Please also note that Dr. Farokhzad took unpaid sabbatical leave from 3/2018, and Dr. Shi served as the interim initiating PI till the end of this project (9/29/2019).

## **2. KEYWORDS**

Nanotechnology, lipid, polymer, hybrid nanoparticle, siRNA delivery, platinum, MYC, prostate cancer, drug resistance, mouse model, pathology, genomics

### 3. ACCOMPLISHMENTS

#### ➤ What were the major goals of the project?

The project has two specific aims. The major tasks and subtasks in the SOW are shown below.

Specific Aim 1: Development and optimization of MYC siRNA-Pt NPs

*Major Task 1. Rational design and creation of siRNA-Pt NPs:* (i) NP optimization for effective gene silencing; (ii) Synthesis of cisplatin prodrugs; and (iii) siRNA-Pt NP development

*Major Task 2. In vitro evaluation and mechanism studies:* (i) Cellular cytotoxicity of MYC siRNA-Pt NPs; and (ii) Mechanism study of the MYC role in Pt resistance

*Major Task 3. In vivo test and optimization:* (i) In vivo studies of select hybrid NPs; and (ii) In vivo evaluation of siRNA-Pt NPs

Specific Aim 2: Determination of the efficacy of select RNAi-Pt NPs in the  $B13^{MYC/Cre}|Pten^{fl/fl}$  engineered PCa mouse model

*Major Task 4. Evaluation of MYC silencing in the genetically engineered mouse model:* (i) NP BioD and MYC silencing; and (ii) Assessment of a MYC gene expression signature to track pharmacodynamic response of MYC siRNA-Pt NP therapy

*Major Task 5. Investigation of tumor development/progression to metastasis and side effects after NP administration:* (i) Effect of MYC siRNA-Pt NPs on PCa progression to metastasis; (ii) Effect of siRNA-Pt NPs on survival in  $B13^{MYC/Cre}|Pten^{fl/fl}$  males with late stage disease; and (iii) Side effects of the combination nanotherapy

#### ➤ What was accomplished under these goals?

Over the entire research period of this project (9/2015 – 9/2019), we made significant accomplishments in each of the proposed tasks. We successfully developed, characterized, and optimized a reduction-responsive NP platform for effective delivery of siRNA and cisplatin prodrug. The siMYC NPs and siMYC-Pt NPs were extensively tested in vitro using different PCa cell lines including Pt-resistant cells, and the combination nanotherapy showed potent anti-tumor efficacy in subcutaneously xenografted PCa mouse model without obvious in vivo toxicities. We also established and characterized the phenotypic features of murine cell lines derived from sites of metastasis of  $B13^{MYC/Cre}|Pten^{fl/fl}$  (BMPC) genetically engineered mouse (GEM) model, which were used for in vitro and RNAseq studies to assess whether the MYC signature is being modulated in the BMPC mice and cell lines. In the BMPC GEM model, the siRNA NPs were able to accumulate in the prostate tumor tissues and silencing MYC expression after intravenous injection. We further determined the anti-tumor efficacy of siMYC NPs, cisplatin prodrug NPs, and siMYC-Pt NPs in BMPC GEM mice, which demonstrated significant anti-tumor efficacy, leading to a quantifiable reduction in tumor burden.

Below are the achievements for each task. For the achievements that were already reported or published, please see the details in the cited articles in the Appendix or in the previous annual reports; for the new unpublished achievements obtained in Year 3 and the no-cost extension (NCE) year, we showed the results under the subtasks.

*Major Task 1. Rational design and creation of siRNA-Pt NPs*

(i) NP optimization for effective gene silencing (Farokhzad and Shi, BWH)

We successfully completed this subtask in Year 1 and 2. We designed and prepared a library of reduction-responsive poly(disulfide amide) (PDSA)-based NPs. We also extensively investigated the effects of formulation parameters and lipid-PEGs on NP properties *in vitro* and *in vivo*. By adjusting the polymer structure and NP formulation, we obtained the optimal NP platform for delivery of siRNA and cisplatin prodrug. Please see the attached *Theranostics* 2017 and *Small* 2018 papers, as well as Year 1 and 2 annual reports, for more details.

(ii) Synthesis of cisplatin prodrugs (Farokhzad and Shi, BWH)  
We designed and synthesized a series of cisplatin prodrugs, and validated the chemical structures by the nuclear magnetic resonance (NMR) analyses. Please see our Year 1 annual report for more details.

(iii) siRNA-Pt NP development (Farokhzad and Shi, BWH)  
In Year 1 and 2 (please see the annual reports), we identified the optimal NP formulation (PDSA8-2 NP) for encapsulation of the cisplatin prodrug Pt-8C and siRNA. In Year 3, we detected the size and morphology of siMYC-Pt NPs, siMYC NPs, and Pt NPs. As shown in Figure 1, the hydrodynamic diameters of siMYC-Pt NPs, siMYC NPs, and Pt NPs are  $62.9 \pm 0.7$ ,  $69.6 \pm 0.6$ , and  $55.3 \pm 0.3$  nm, while the apparent diameters estimated from the transmission electron microscopy (TEM) images were about 60, 65, and 50 nm, respectively. All the NP formulations showed the spherical morphologies. These NPs were used for in vitro tests and for in vivo studies with both xenografted and GEM models of PCa.

## Major Task 2. In vitro evaluation and mechanism studies

(i) Cellular cytotoxicity of MYC siRNA-Pt NPs (Farokhzad and Shi, BWH)  
We demonstrated that the PDSA NPs efficiently delivered siMYC to PCa cell line (PC3 cells) and silenced the MYC expression, and used these NPs to encapsulate Pt-8C and then revealed the cytotoxicity of Pt-8C-loaded PDSA NPs (Pt NPs) against PC3 cells (please see Year 1 and 2 reports). We then tested the cellular uptake and cytotoxicity of the siMYC-Pt NPs in PC3 cells. As can be seen in Figure 2A, the NP formulations markedly improved siMYC uptake as compared to free siMYC. Both cell viability and apoptosis results (Figure 2B and 2C) showed that the combination of siMYC with Pt in the NPs are more potent against PC3 cells than siMYC NPs or Pt NPs alone.

(ii) Mechanism study of the MYC role in Pt resistance (Farokhzad and Shi, BWH; De Marzo, JHU)

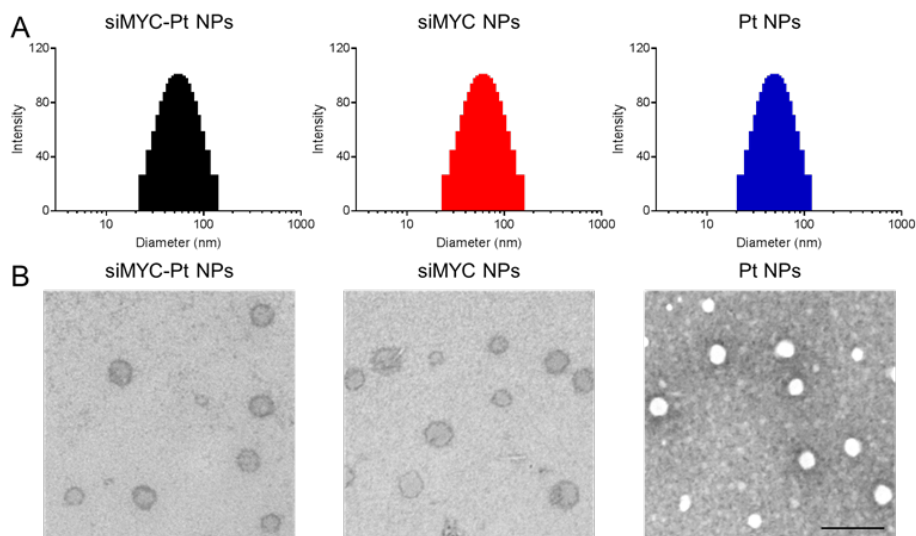


Figure 1. (A) Size and distribution and (B) TEM image of siMYC-Pt NPs, siMYC NPs, and Pt NPs.

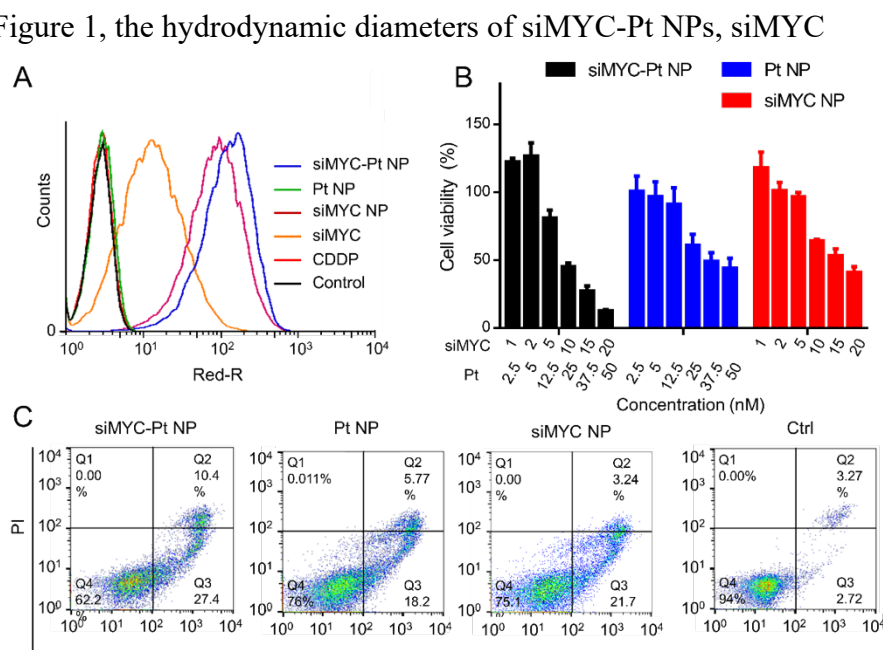


Figure 2. (A) Cell uptake after incubation with Pt+siMYC NP, Pt NP, siMYC NP, siMYC, cisplatin, or PBS as Ctrl for 2 h. siMYC is labeled with Cy5. (B) In vitro cytotoxicity of siMYC-Pt NP, siMYC NP, and Pt NP in PC3 cells after incubation for 48 h. (C) Cellular apoptosis after incubation with siMYC-Pt NP, siMYC NP, or Pt NP.

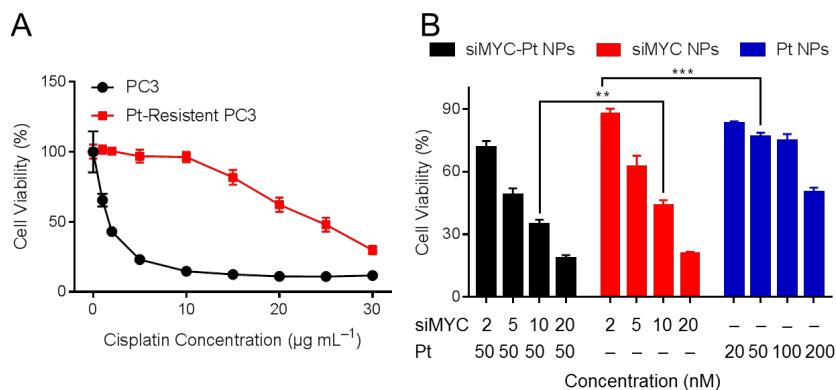


Figure 3. (A) Cisplatin resistance assessment of Pt-resistant PC3 cells after establishment. (B) Cytotoxicity of siMYC-Pt NPs, siMYC NPs, and Pt NPs toward Pt-resistant PC3 cells ( $n = 3$ ;  $**P < 0.01$ ,  $***P < 0.001$ ).

We investigated whether the MYC silencing sensitized Pt-resistant PC3 cells to the treatment with cisplatin. We examined the cytotoxicity of siMYC-Pt NPs toward the Pt-resistant PC3 cells we established. The half maximal inhibitory concentration ( $IC_{50}$ ) of cisplatin against PC3 cells is  $1.78 \mu\text{g mL}^{-1}$ , while the  $IC_{50}$  toward Pt-resistant PC3 cells ( $22.80 \mu\text{g mL}^{-1}$ ) is about 13 times higher, indicating the successful establishment of the Pt-resistant cells (Figure 3A). After that, the cell proliferation inhibition efficacy of siMYC-Pt NPs, siMYC NPs, and Pt NPs were assessed toward Pt-resistant PC3 cells, as shown in Figure 2B. With the siMYC dose of 10.0 nM and Pt dose of 50.0 nM, the cell viabilities are  $34.6 \pm 2.4$ ,  $44.0 \pm 2.3$ , and  $76.7 \pm 1.9$  in the groups of siMYC-Pt NPs, siMYC NPs, and Pt NPs, respectively (Figure 3B). These results demonstrated that the co-administrated siMYC and Pt formulation showed better antitumor efficacy *in vitro*. We also demonstrated that the Pt-resistant cells showed higher MYC expression than that of the parental cells (Year 2 report). We hypothesize that the reversal of Pt resistance by silencing MYC in PCa cells might be through upregulating the expression of cyclin-dependent kinase inhibitor p21 and decreasing the level of proliferating cell nuclear antigen (PCNA).

### Major Task 3. *In vivo* test and optimization

(i) *In vivo* studies of select hybrid NPs (Farokhzad and Shi, BWH; De Marzo, JHU)

This subtask was primarily completed in Year 2 of this project. We assessed the pharmacokinetics (PK) of siRNA NPs and revealed that the circulating half-life ( $t_{1/2}$ ) of DY677-siRNA NPs ( $\sim 4.92$  h) was significantly prolonged compared to that of the free DY677-siRNA ( $\sim 10$  min) in normal BALB/c mice. In addition, we demonstrated that the siRNA-loaded NPs showed about 6-fold higher accumulation in the subcutaneously xenografted PCa tumors than free siRNA. Moreover, the administration of the MYC siRNA-loaded NPs leads to  $\sim 55\%$  knockdown in MYC expression compared to the control NPs *in vivo*. The immunohistochemical (IHC) analyses also confirmed the effective MYC silencing by siMYC NPs *in vivo*. The results were published in *Small* 2018.

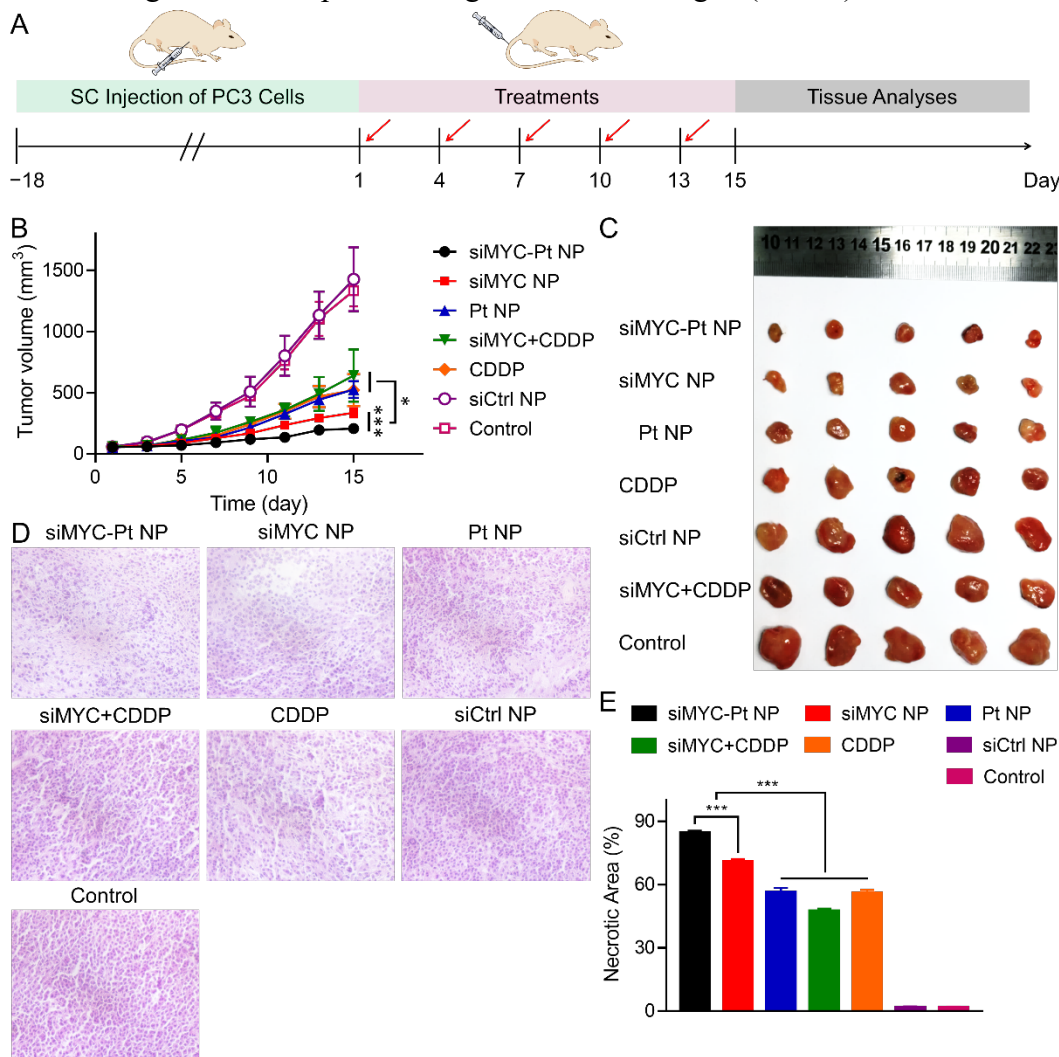


Figure 4. (A) Timeline for animal model construction, treatment, and tumor tissue evaluation of subcutaneous PCa. (B) Tumor volume changes during the treatments with siMYC and Pt formulations ( $n = 5$ ,  $*P < 0.05$ ,  $***P < 0.001$ ). (C) Photos of tumors after all treatments. (D) H&E image of tumor tissues after treatment with siMYC and Pt formulations (magnification: 200 $\times$ ). (E) Semi-quantitative necrotic areas of tumor sections from H&E images.

(ii) *In vivo* evaluation of siRNA-Pt NPs (Farokhzad and Shi, BWH; De Marzo, JHU)

With these results of MYC silencing, cell proliferation inhibition, and PK/BioD described above, we further evaluated the antitumor efficacy of siMYC and Pt nanoparticle formulations *in vivo*. As shown in Figure 4A, after subcutaneous inoculation of PC3 cells in athymic nude mice, the NPs and controls were administered every three days with the siMYC dose of 1.0 nmol per mouse and the Pt dose of 8.0  $\mu\text{mol per kg}$  body weight. After all the treatments, siMYC-Pt NPs showed the most effective tumor inhibition efficacy with the final average tumor volume at  $\sim 200 \text{ mm}^3$ , while average tumor volume in the control groups reached around 1,400

mm<sup>3</sup>, as shown in Figure 4B. The tumor inhibition rates of siMYC-Pt NPs, siMYC NPs, Pt NPs, siMYC+Cisplatin, Cisplatin, siCtrl NPs, and Ctrl were 84.5% ± 2.6%, 74.8% ± 8.3%, 60.6% ± 8.0%, 51.9% ± 17.4%, 60.9% ± 15.4%, 0 ± 1.3%, 0 ± 0.1%, respectively. Furthermore, the antitumor efficacy of NP loading siMYC and/or Pt, especially siMYC-Pt NPs, were confirmed by the photos of all the tumors (Figure 4C). The above results indicated the outstanding anti-tumor efficacy of siMYC-Pt NPs.

We also demonstrated the anti-tumor efficacy of siMYC NPs, Pt NPs, and siMYC-Pt NPs by the hematoxylin and eosin (H&E) staining and the terminal deoxyribonucleotidyl transferase (TDT)-mediated dUTP-digoxigenin nick end labeling (TUNEL) assays. As shown in Figure 4D and 4E, the siMYC-Pt exhibited the highest ratio of an area with severe nucleus shedding (about 85%) in the tumor tissue after treatment. Furthermore, the cell apoptosis levels of tumor tissues after all treatments of siMYC and Pt formulations were established by TUNEL assays. As shown in Figure 5, all the groups of siMYC and Pt formulations, especially the siMYC-Pt group, showed the obvious apoptosis signals in the tumor section. The apoptosis ratios in the tumor section after treatment with siMYC-Pt NPs, siMYC NPs, Pt NPs, siMYC+Cisplatin, Cisplatin, siCtrl NPs, or Ctrl were 27.7% ± 1.2%, 22.9% ± 0.6%, 15.8% ± 1.0%, 14.6% ± 0.6%, 15.2% ± 0.7%, 1.8% ± 0.3%, and 0.7% ± 0.2%, respectively (Figure 5B).

MYC silencing and regulation of the related downstream signals, including p21, Bcl-2, and PCNA, were characterized by immunofluorescence detection. As shown in Figure 6, the treatment with various siMYC-loaded nanoformulations could significantly silence the expression of MYC protein. The quantitative result in Figure 6B demonstrated that Pt+siMYC NP and siMYC NP suppressed the MYC expression significantly, while free siMYC did not work. The MYC silencing also improved the sensitivity of PC3 cells to Pt, presumably through the down-regulation of Bcl-21 and PCNA and

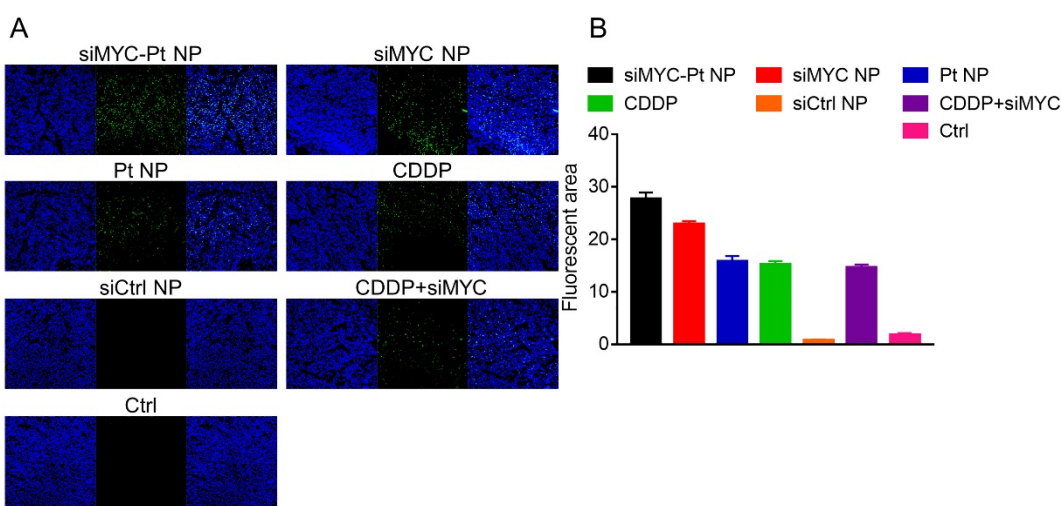


Figure 5. (A) TUNEL staining of tumor tissues after treatments with siMYC and Pt formulations; and (B) semi-quantitative analysis ( $n=3$ ; \*\*\* $P<0.001$ ).

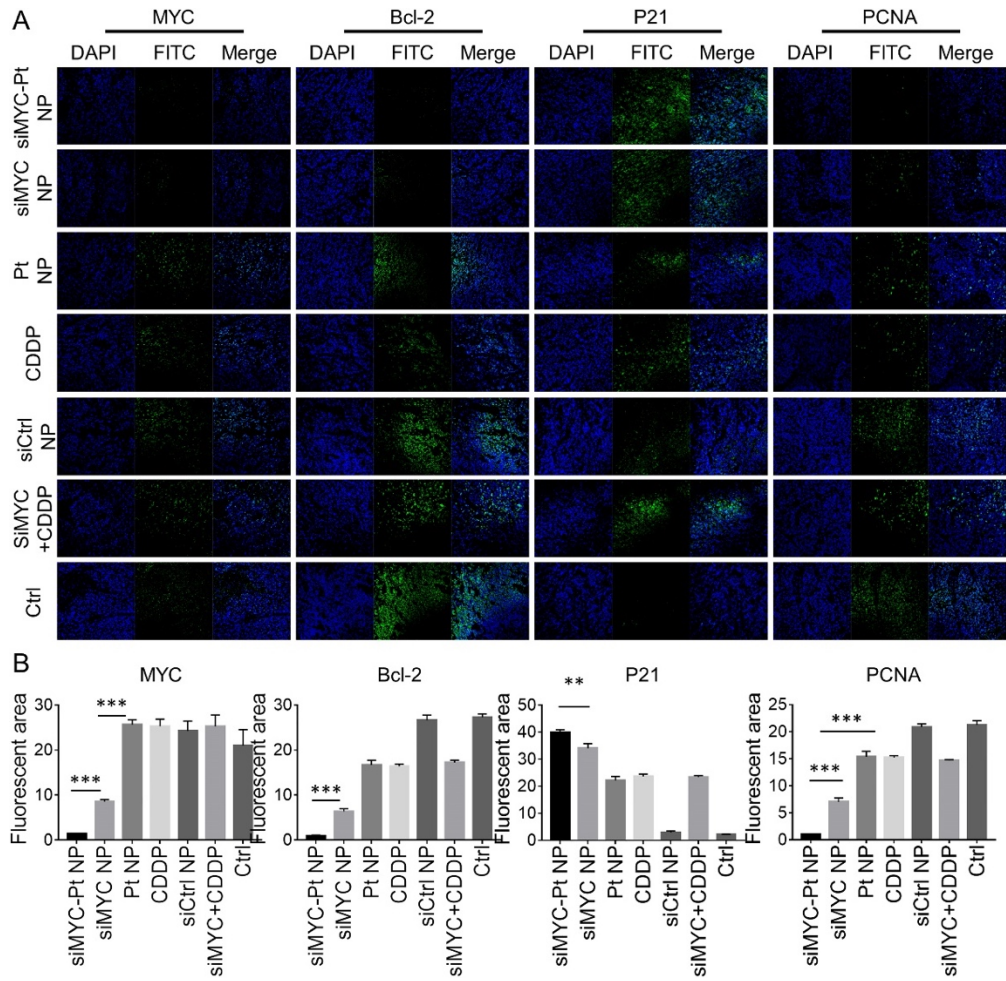


Figure 6. (A) Immunofluorescence images of MYC, Bcl-2, p21, and PCNA and (B) semi-quantitative analysis of tumor sections after treatments with siMYC and Pt formulations.

the up-regulation of p21. Moreover, we tested the biosafety of the siMYC-Pt NPs. All the biochemical indicators associated with the function of the heart [creatinine kinase (CK)], liver [alanine aminotransferase (ALT) and aspartate aminotransferase (AST)], and kidney [blood urea nitrogen (BUN) and creatinine (Cr)] maintained in the normal ranges after all the treatments (Figure 7). These results indicated that the siMYC-Pt NPs were safe under the tested dose and administration frequency.

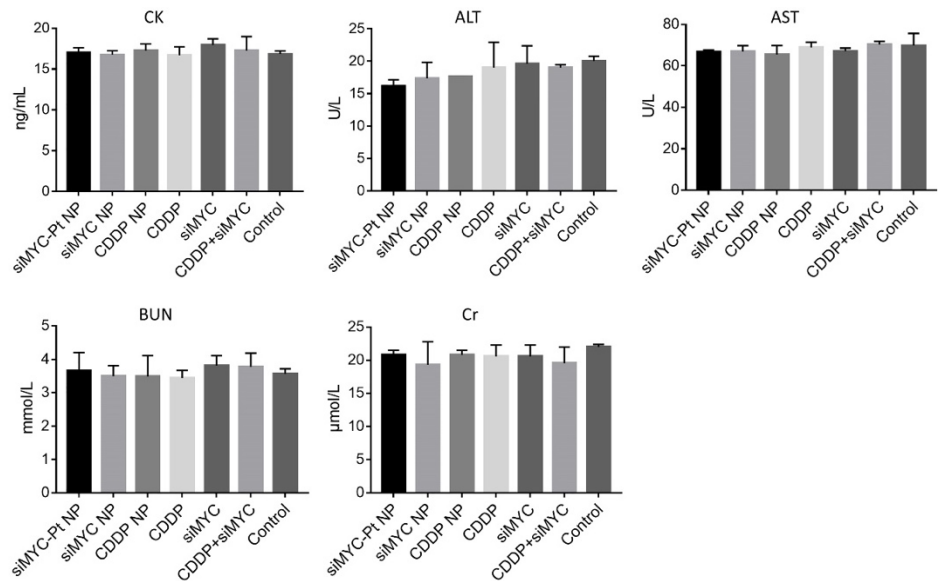


Figure 7. Evaluation of CK, ALT, AST, BUN, and Cr levels after various treatments.

#### Major Task 4. Evaluation of MYC silencing in the genetically engineered mouse model:

(i) NP BioD and MYC silencing (Bieberich, UMBC; De Marzo; and Yegnasubramanian JHU; Farokhzad and Shi, BWH)

##### Further characterization of BMPC1 and BMPC2 cell lines

Given the effect of R1881 on AR protein levels in BMPC1 that we reported in the year 2 progress report, we examined the effect of both R1881 supplementation and anti-androgen treatment in a series of in vitro growth experiments. We examined the cell growth of both BMPC1 and BMPC2 in the presence and absence of the anti-androgen, enzalutamide (Figure 8A). BMPC1 and BMPC2 cell growth was not affected by the addition of enzalutamide, comparable to the effect on the AR-negative, human prostate cancer cell line, PC3. As AR protein levels were stabilized in the presence of androgen, we sought to determine the growth effect of androgen supplementation. BMPC1 and BMPC2 cells were grown in media supplemented with charcoal stripped serum which reduced the growth of all cell lines tested, including PC3 (Figure 8). The addition of 10 nM R1881 rescued the growth of the androgen-sensitive, mouse cell line, MYC-CaP, but did not affect the growth of BMPC1, BMPC2, or PC3 cells. Please see the attached *Prostate* 2018 paper for more details.

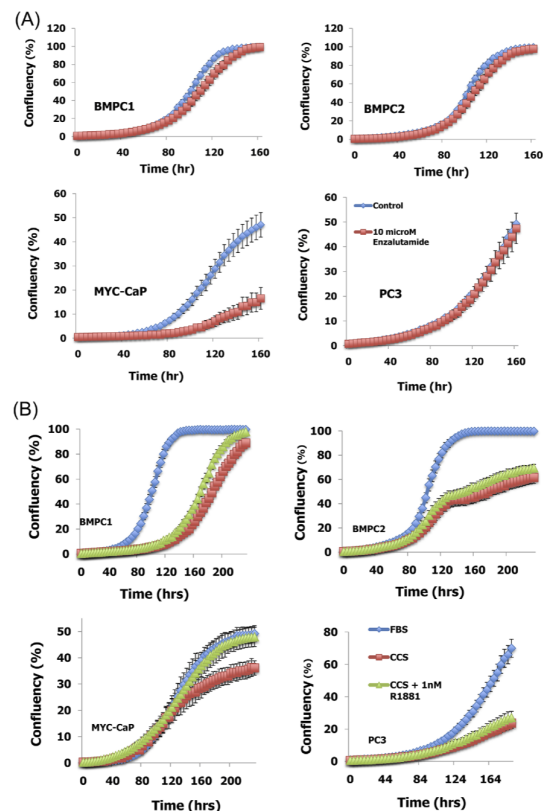


Figure 8. Effect of R1881 and enzalutamide on BMPC1 and BMPC2 Cell Growth. Using Incucyte imaging software, cell growth (% confluency) was measured over a time course of up to 200 h following treatment with (A). Enzalutamide 10 μM and (B) 1 nM and 10 nM R1881. Growth of BMPC1 and BMPC2 cell lines were not significantly affected by treatment with an anti-androgen or restoration of androgen.

##### NP BioD in the BMPC model

In Year 2 of this project, we revealed that the Cy7-siRNA NPs showed much higher accumulation in the primary tumors with the volumes of about 4000 mm<sup>3</sup> than that of the free Cy7-siRNA. In Year 3, we assessed the BioD of Cy7-siRNA NPs in the primary tumor models with smaller tumor size (~ 300 mm<sup>3</sup>). As shown in Figure 9, Cy7-siRNA NPs even accumulated more efficiently in the smaller primary tumors at 24 h after intravenous injection.

##### MYC silencing in the allograft and GEM models

In Year 2 of this project, we examined the NP-mediated MYC silencing in the BMPC1 cells. The siMYC NPs significantly silenced the MYC expression in BMPC1 cells at a dose of 40 nM and inhibited the proliferation.

Moreover, the siMYC NPs efficiently reduced around 60% MYC expression in the BMPC1 PCa tumor, which was revealed by Western blot and IHC. In Year 3, we examined MYC silencing in BMPC tumors. A key consideration in this analysis is assuring that the BMPC tumors in mice receiving the siMYC NPs are at similar stages of disease progression. To this end, we reported in the Year 2 annual report that we developed a non-invasive

method to accurately determine BMPC tumor size using manual palpation. Animals are briefly restrained by hand and the peri-pubic area is gently squeezed using thumb and forefingers until the bladder, prostate, and seminal vesicles are located. This approach obviates the need for repeated administration of anesthesia and analysis by micro-CT. To determine the utility of this method, a cohort of BMPC mice was palpated weekly to follow tumor progression from the 0.5 g stage until 5 g (the IACUC-approved criterion for euthanasia).

To determine the effect of MYC siRNA NP treatment in BMPC tumors, three animals with 0.5 g tumors were administered MYC siRNA NPs (PDSA-siMYC or PLGA-siMYC via tail vein injection. PDSA NPs loaded with Luciferase siRNA served as a negative control. Each mouse received three treatments on a one on, on off schedule and was euthanized 24 hours after the final NP injection. Western blot analysis showed ~50% knockdown of MYC steady-state levels in both animals that received siMYC NPs (Figure 10). These data demonstrate that MYC siRNA can be effectively delivered to BMPC tumors to down-regulate MYC expression in BMPC tumors.

#### (ii) MYC signature analysis in BMPC mice (Yegnasubramanian and De Marzo, JHU; Bieberich, UMBC)

During Year 3 to better decipher the effects of MYC knockdown using the nanoparticles in the BMPC mice we have performed more extensive bioinformatics analyses on the anterior mouse lobes of the FVB wild-type, the *B13<sup>Cre</sup>|Pten<sup>fl/fl</sup>* males with PIN lesions and the BMPC males with PIN lesions (Figure 11). RNA-seq analysis was performed to understand the contribution of MYC in early carcinogenesis that might set the stage for the cooperation of MYC gain and PTEN loss in driving the rapid and aggressive progression to high volume invasive and metastatic disease. These analyses revealed that precursor PIN lesions in PTEN null animals show significantly altered (mostly upregulated) expression of immunogenic genes, which was largely lost by the addition of MYC gain in the BMPC PIN lesions, likely setting the stage for immune evasion and rapid disease progression.

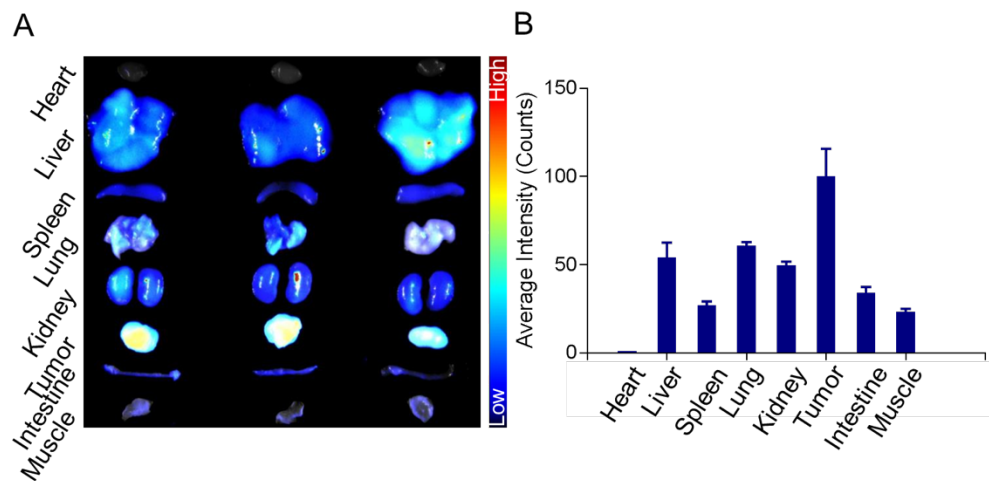


Figure 9. (A) Overlaid fluorescent image of tumors and main organs of primary PCa tumor-bearing GEM mice sacrificed at 24 h postinjection of the Cy7-siRNA NPs; and (B) semi-quantitative analysis ( $n=3$ ;  $***P < 0.001$ ).

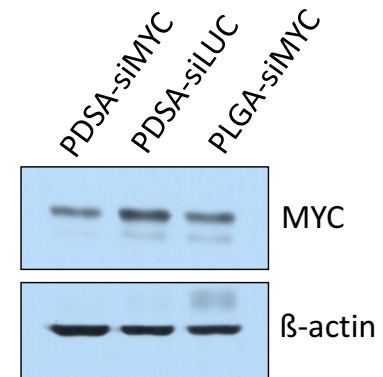


Figure 10. Western blot analysis of MYC expression in BMPC tumors after siMYC NP treatment. NP treatment diminished MYC expression in BMPC mice.

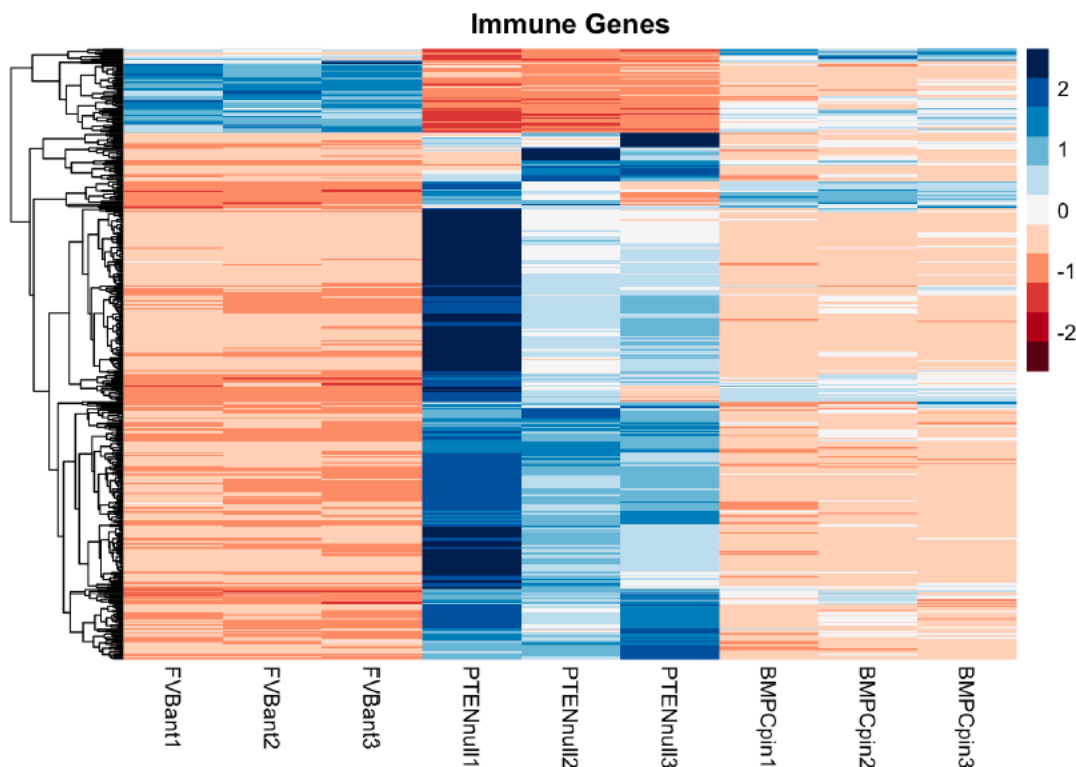


Figure 11. PIN lesions in BMPC animals significantly attenuate the altered expression of immunogenic pathways that are activated in the PIN lesions from PTEN null animals. In this heatmap, the expression of genes from the Gene Ontology (GO) term Immune System Process were plotted. Note that PTEN null PIN lesions (middle 3 columns) significantly upregulate the majority of these genes compared to the normal FVB. Interestingly, the BMPC-PIN lesions largely lose this altered immune system pathway expression, reflecting a contribution of MYC in attenuating immunogenic pathways, perhaps allowing these precursors to progress through immune evasion.

NPs	siCntrl	siMYC	siMYC+Pt	Pt
BMPCs enrolled	5	5	5	5

Major Task 5.  
Investigation of tumor

Table 1. siMYC-Pt NP efficacy trial in BMPC mice.

development/progression to metastasis and side effects after NP administration: (i) Effect of MYC siRNA-Pt NPs on PCa progression to metastasis; (ii) Effect of siRNA-Pt NPs on survival in  $B13^{MYC/Cre}|Pten^{fl/fl}$  males with late stage disease; and (iii) Side effects of the combination nanotherapy

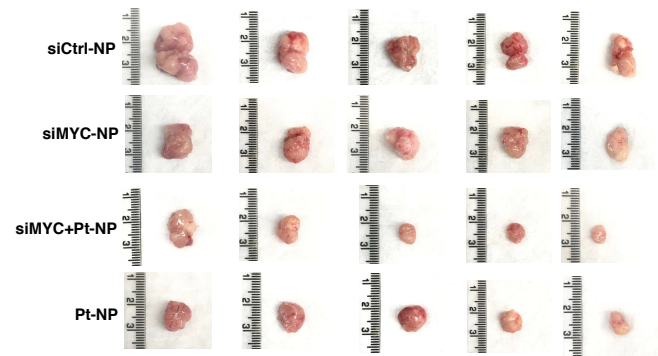


Figure 12. Whole mount BMPC prostate tumors after treatment with NPs.

In Year 3, we initiated a trial to test the therapeutic efficacy of MYC siRNA-Pt NPs in BMPC mice. Due to the relatively large number of BMPC mice required to complete this study, and the fact that each mouse carries four transgene alleles, we opted to perform this study by enrolling mice on a rolling basis as they develop 0.5 g prostate tumors. Following a cohort of ~50 BMPC mice by weekly palpation, we enrolled 11 mice in the four groups shown in Table 1 in Year 3, and the remaining 9 in Year 4.

To determine the effects on disease progression of administering siMY NPs, Pt NPs, and siMYC + Pt NPs to

tumor-bearing BMPC mice, NPs were delivered i.v. on a one-on, two-off regimen for 15 days. Prostate tumors dissected from NP-treated mice were weighed and the extent of metastatic disease was determined (Figure 12). Treatment with siMYC NPs resulted in an obvious decrease in wet weight of autochthonous BMPC prostate tumors (Figure 13), although comparison to the control cohort revealed that statistical significance was just barely not achieved ( $p=0.052$ ). It is important to note that this is a remarkable result given the relatively small

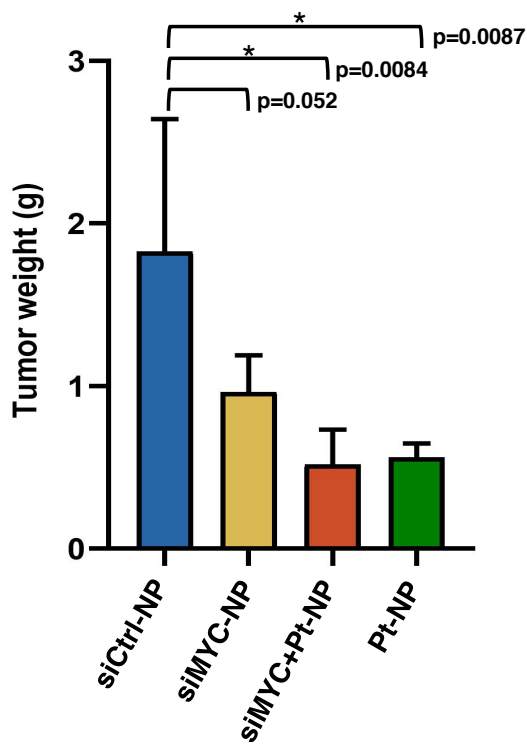


Figure 13. Average tumor weight from each group shown in Figure 12.

sample size and the high degree of variance in prostate tumor size in the control cohort. In contrast, treatment with NPs loaded with both siMYC and Pt resulted in a highly statistically significant reduction in tumor weight (Figure 13). However, treatment with Pt-alone NPs achieved a similar diminution of prostate tumor size. Given that the estimated tumor volume upon treatment initiation was 0.5 g, it is clear that both Pt NPs alone and siMYC + Pt NPs completely blocked tumor expansion. As a result, we were not able to determine whether siMYC treatment potentiates the therapeutic response to Pt, or vice versa. These data indicate that it will be necessary in future experiments to perform a single agent dose-response study to optimize the dose of siMYC and Pt NPs in a range that will permit observation and quantification of combinatorial effects. No differences were observed in the extent of metastatic disease among the four treatment groups. This is most likely due to the presence of metastatic lesions prior to the initiation of treatment. NP treatments were generally well tolerated, however, two unexplained deaths occurred in the Pt NP group, further suggesting that future experiments will be required to determine the optimal Pt NP dose.

### ➤ What opportunities for training and professional development has the project provided?

While the Brigham and Women's Hospital (BWH) does not have an institutional policy requiring individual development plans for postdoctoral fellows and graduate students, the hospital is very committed to training its students and fellows to meet their research and career goals. The hospital supports a centralized career development office, *Office for Research Careers of BWH Brigham Research Institute*, which offers seminars ranging from career development to responsible conduct of research to how to secure NIH and other external funding. The office also addresses the specific needs of postdoctoral fellows and faculty investigators in the research community at BWH, and supports BWH researchers across the academic continuum, by providing resources to support career and professional development, by encouraging professional responsibility, enhancing the training experience and fostering effective mentoring. As a teaching affiliate of Harvard Medical School, BWH students and fellows have access to career development and support services offered by Harvard. Within my group, the postdoctoral fellows and students have routine meetings with me to discuss research project, skill and career development, and other needs they may have, and they present research work in the biweekly group meeting. The postdoctoral fellows and students are also encouraged and supported to attend local seminars, workshops, national conferences, and advanced education courses to present their research work, interact with colleagues, and enhance professional knowledge and skills, all of which will be helpful for their career development.

At Johns Hopkins there are a number of excellent opportunities for the professional development of our trainees related to this project. The pathology fellow is learning the histopathology of our prostate cancer mouse models and xenografts and also learning about IHC staining, in situ hybridization, automated whole slides scanning and digital image analysis. Also, one of our oncology fellows has been central in developing and characterizing the BMPC cell lines in which he has been involved in cell culture, cell cloning and phenotyping. We meet weekly with the pathology and oncology fellows in which we discuss their research and they present results. Also, we hold weekly and biweekly lab meetings with other collaborating labs, including Drs. Yegnasubramanian's lab. In terms of bioinformatics opportunities, Dr. Yegnasubramanian is mentoring a number of trainees who are working on the RNAseq data analysis and gene signatures. All trainees also have access to a number of lectures on cancer including our Fall Course on Cancer Biology given in the oncology department that meets twice per

week and covers major topics related to cancer biology and treatment. Dr. Bieberich holds weekly meetings with his participating students and they are afforded a number of excellent opportunities. Drs. Bieberich, De Marzo and Yegnasubramanian hold periodic meetings to discuss the project and fellows and students often take part in these discussions.

➤ **How were the results disseminated to communities of interest?**

Nothing to report.

➤ **What do you plan to do during the next reporting period to accomplish the goals?**

Nothing to report

#### **4. IMPACT**

➤ **What was the impact on the development of the principal discipline(s) of the project?**

The new generation of redox-responsive lipid-polymer hybrid nanoparticle (NP) platform has shown unique features for systemic siRNA delivery with effective in vivo gene silencing. This may be impactful for the field of RNAi cancer therapy. The combination of siMYC NPs with Pt prodrugs also led to highly effective anti-tumor growth, which may shed new insight on combinatorial therapy of prostate cancer. In addition, we have established new cell lines from the BMPC transgenic mouse model. These cell lines could be useful for fundamental biology study of prostate cancer. Moreover, the RNAseq experiments on the BMPC that will lay the groundwork for deriving our MYC signature that could potentially be used as a pharmacodynamics marker in subsequent studies, and will help provide mechanistic insights into the synergy that results as a result of combined MYC activation and PTEN loss that drives prostate cancer disease aggressiveness and metastases.

➤ **What was the impact on other disciplines?**

Nothing to report.

➤ **What was the impact on technology transfer?**

Nothing to report.

➤ **What was the impact on society beyond science and technology?**

Nothing to report.

## **5. CHANGES/PROBLEMS**

### **➤ Changes in approach and reasons for change**

Nothing to report.

### **➤ Actual or anticipated problems or delays and actions or plans to resolve them**

Nothing to report.

### **➤ Changes that had a significant impact on expenditures**

Nothing to report.

### **➤ Significant changes in use or care of human subjects, vertebrate animals, biohazards, and/or select agents**

Nothing to report.

### **➤ Significant changes in use or care of human subjects**

Nothing to report.

### **➤ Significant changes in use or care of vertebrate animals**

Nothing to report.

### **➤ Significant changes in use of biohazards and/or select agents**

Nothing to report.

## 6. PRODUCTS

### ➤ Publications, conference papers, and presentations

Journal publications:

1. One manuscript under preparation for the combination therapy of siMYC-Pt NPs.
2. Xu X, Wu J, Liu S, Saw PE, Tao W, Li Y, Krygsman L, Yegnasubramanian S, De Marzo AM, Shi J, Bieberich C.J, Farokhzad OC. Redox-Responsive Nanoparticle-Mediated Systemic RNAi for Effective Cancer Therapy. **Small** 2018; 14 (41), e1802565. (Acknowledgement of federal support: Yes)
3. Markowski MC, Hubbard GK, Hicks JL, Zheng Q, King A, Esopi D, Rege A, Yegnasubramanian S, Bieberich CJ, De Marzo AM. Characterization of novel cell lines derived from a MYC-driven murine model of lethal metastatic adenocarcinoma of the prostate. **Prostate**. 2018 Sep;78(13):992-1000. (Acknowledgement of federal support: Yes)
4. Zhu X, Tao W, Liu D, Wu J, Guo Z, Ji X, Bharwani Z, Zhao L, Zhao X, Farokhzad OC, Shi J. Surface De-PEGylation Controls Nanoparticle-Mediated siRNA Delivery In Vitro and In Vivo. **Theranostics** 2017; 7(7):1990-2002. (Acknowledgement of federal support: yes)
5. Shi J, Kantoff PW, Wooster R, Farokhzad OC. Cancer Nanomedicine: Progress, Challenges and Opportunities. **Nat Rev Cancer** 2017; 17:20-37. (Acknowledgement of federal support: yes)
6. Xu X, Wu J, Liu YL, Zhao L, Zhu X, Bhasin S, Li Q, Shi J, Farokhzad OC. Ultra pH-Responsive and Tumor-Penetrating Nanoplatform for Targeted siRNA Delivery with Robust Anti-Cancer Efficacy. **Angew Chem Int Ed** 2016; 55(25):7091-4. (Acknowledgement of federal support: yes)

### ➤ Website(s) or other Internet site(s)

Nothing to report.

### ➤ Technologies or techniques

Nothing to report.

### ➤ Inventions, patent applications, and/or licenses

Stimuli-Responsive Nanoparticles for Biomedical Applications; Inventors: Xiaoding Xu, Jinjun Shi, Omid C. Farokhzad; PCT / US2017 / 025772.

### ➤ Other Products

Nothing to report.

## 7. PARTICIPANTS & OTHER COLLABORATING ORGANIZATIONS

### ➤ What individuals have worked on the project?

**BWH** (Please also note that Dr. Farokhzad took unpaid sabbatical leave from 3/2018, and Dr. Shi served the interim initiating PI till the end of this project.)

Name:	<i>Omid C. Farokhzad</i>
Project Role:	<i>Initiating PI</i>
Researcher Identifier (e.g. ORCID ID):	
Nearest person month worked:	<i>0.6</i>
Contribution to Project:	<i>Dr. Farokhzad oversees the whole project.</i>
Funding Support:	

Name:	<i>Jinjun Shi</i>
Project Role:	<i>Co-investigator</i>
Researcher Identifier (e.g. ORCID ID):	
Nearest person month worked:	<i>1.2</i>
Contribution to Project:	<i>Dr. Shi supervised the design and development of the hybrid siRNA NPs and siRNA-Pt NPs.</i>
Funding Support:	

Name:	<i>Jianxun Ding</i>
Project Role:	<i>Postdoctoral Research Fellow</i>
Researcher Identifier (e.g. ORCID ID):	
Nearest person month worked:	<i>12</i>
Contribution to Project:	<i>Dr. Ding led the polymer synthesis, Pt prodrug synthesis, siRNA-Pt NP development, and the corresponding characterizations.</i>
Funding Support:	

Name:	<i>Xiaoding Xu</i>
Project Role:	<i>Postdoctoral Fellow</i>
Researcher Identifier (e.g. ORCID ID):	
Nearest person month worked:	<i>12</i>
Contribution to Project:	<i>Dr. Xu led the siRNA NP development and characterization, polymer synthesis, Pt prodrug synthesis, and in vitro/in vivo testing</i>
Funding Support:	

Name:	<i>Yujing Li</i>
Project Role:	<i>PhD Student</i>
Researcher Identifier (e.g. ORCID ID):	
Nearest person month worked:	<i>6</i>
Contribution to Project:	<i>Ms. Li helped Dr. Xu with NP preparation and characterization, and in vitro testing</i>
Funding Support:	<i>Chinese Scholarship Council</i>

Name:	<i>Amanda Victorious</i>
Project Role:	<i>Undergraduate Student</i>
Researcher Identifier (e.g. ORCID ID):	<i>Ms. Victorious helped Dr. Xu with NP preparation and characterization, and in vitro testing</i>

Nearest person month worked:	8
Contribution to Project:	
Funding Support:	<i>Prostate Cancer Foundation</i>

## JHU

Name:	<i>Angelo De Marzo</i>
Project Role:	<i>Partnering PI</i>
Researcher Identifier (e.g. ORCID ID):	
Nearest person month worked:	0.6
Contribution to Project:	<i>Dr. De Marzo oversees all experiments at JHU for pathology and sequencing of NP-treated tumor tissues.</i>
Funding Support:	
Name:	<i>Srinivasan Yegnasubramanian</i>
Project Role:	<i>Co-investigator</i>
Researcher Identifier (e.g. ORCID ID):	
Nearest person month worked:	0.6
Contribution to Project:	<i>Dr. Yegnasubramanian has supervised the RNAseq experiments and the bioinformatics analyses.</i>
Funding Support:	
Name:	<i>Ajay Vaghasia</i>
Project Role:	<i>Technician</i>
Researcher Identifier (e.g. ORCID ID):	
Nearest person month worked:	2.4
Contribution to Project:	<i>Mr. Vaghasia worked on the mouse RNAseq bioinformatics analyses</i>

Name:	<i>Jessica Hicks</i>
Project Role:	<i>Technician</i>
Researcher Identifier (e.g. ORCID ID):	
Nearest person month worked:	0.6
Contribution to Project:	<i>Mrs. Hicks performed IHC assays on the NP treated tissues</i>
Funding Support:	

## UMBC

Name:	<i>Charles Bieberich</i>
Project Role:	<i>Partnering PI</i>
Researcher Identifier (e.g. ORCID ID):	
Nearest person month worked:	2
Contribution to Project:	<i>Dr. Bieberich oversees all experiments at UMBC to test nanotherapies in BPMC GEM models and in allograft-bearing mice.</i>
Funding Support:	<i>Prostate Cancer Foundation</i>

Name:	<i>Tejhsree Joglekar</i>
-------	--------------------------

Project Role:	<i>Graduate student</i>
Researcher Identifier (e.g. ORCID ID):	
Nearest person month worked:	<i>6</i>
Contribution to Project:	<i>Culture and injection of BMPC cells to generate allograft tumors; maintenance of BMPC colony to generate mice for NP efficacy analyses</i>
Funding Support:	

Name:	<i>Apurv Rege</i>
Project Role:	<i>Graduate student</i>
Researcher Identifier (e.g. ORCID ID):	
Nearest person month worked:	<i>12</i>
Contribution to Project:	<i>Genotypic analysis of BMPC mice</i>
Funding Support:	<i>UMBC graduate teaching assistantship</i>

- **Has there been a change in the active other support of the PD/PI(s) or senior/key personnel since the last reporting period?**

Nothing to report

- **What other organizations were involved as partners?**

**We have two partnering organizations in this project.**

Partnering PI: Angelo M. De Marzo; Co-I: Srinivasan Yegnasubramanian

Organization Name: The Johns Hopkins University

Organization Location: School of Medicine, 733 N Broadway Baltimore, MD 21205

Partner's Contribution: Collaboration

Partnering PI: Charles J. Bieberich

Organization Name: University of Maryland, Baltimore County

Organization Location: Department of Biological Sciences, 1000 Hilltop Rd, Baltimore, MD 21250

Partner's Contribution: Collaboration

## **8. SPECIAL REPORTING REQUIREMENTS**

### **➤ COLLABORATIVE AWARDS**

This collaborative award is led by Initiating PI (Dr. Farokhzad) and Partnering PIs (Drs. De Marzo and Bieberich). We prepared the report together, and the tasks are clearly marked with the responsible PI and research site as shown in **3. ACCOMPLISHMENTS**.

### **➤ QUAD CHARTS**

Nothing to report.

## 9. APPENDICES

Please see attached the three published papers (*Theranostics* 2017; *Small* 2018; and *Prostate* 2018).

## Research Paper

# Surface De-PEGylation Controls Nanoparticle-Mediated siRNA Delivery *In Vitro* and *In Vivo*

Xi Zhu<sup>1,2\*</sup>, Wei Tao<sup>1\*</sup>, Danny Liu<sup>1,3</sup>, Jun Wu<sup>1,4</sup>, Zilei Guo<sup>1</sup>, Xiaoyuan Ji<sup>1</sup>, Zameer Bharwani<sup>1</sup>, Lili Zhao<sup>1,5</sup>, Xiaoping Zhao<sup>2</sup>, Omid C. Farokhzad<sup>1,6</sup>✉, Jinjun Shi<sup>1</sup>✉

1. Center for Nanomedicine and Department of Anesthesiology, Brigham and Women's Hospital, Harvard Medical School, Boston, MA 02115, USA;
2. National Shanghai Center for New Drug Safety Evaluation and Research, Shanghai, 201203, China;
3. Department of Chemistry, University of Waterloo, Waterloo, Ontario N2L 3G1, Canada;
4. Department of Biomedical Engineering, School of Engineering, Sun Yet-sen University, Guangzhou, 510006, China;
5. Department of Endoscopy, the First Affiliated Hospital of Nanjing Medical University, Jiangsu Province Hospital, Nanjing, 210029, China;
6. King Abdulaziz University, Jeddah 21589, Saudi Arabia.

\* X.Z. and W.T. contributed equally to this work.

✉ Corresponding authors: Email: ofarokhzad@bwh.harvard.edu (O.C.F.), Email: jshi@bwh.harvard.edu (J.S.).

© Ivyspring International Publisher. This is an open access article distributed under the terms of the Creative Commons Attribution (CC BY-NC) license (<https://creativecommons.org/licenses/by-nc/4.0/>). See <http://ivyspring.com/terms> for full terms and conditions.

Received: 2016.10.29; Accepted: 2017.03.11; Published: 2017.05.12

## Abstract

The present work proposes a unique de-PEGylation strategy for controllable delivery of small interfering RNA (siRNA) using a robust lipid-polymer hybrid nanoparticle (NP) platform. The self-assembled hybrid NPs are composed of a lipid-poly(ethylene glycol) (lipid-PEG) shell and a polymer/cationic lipid solid core, wherein the lipid-PEG molecules can gradually dissociate from NP surface in the presence of serum albumin. The de-PEGylation kinetics of a series of different lipid-PEGs are measured with their respective NPs, and the NP performance is comprehensively investigated *in vitro* and *in vivo*. This systematic study reveals that the lipophilic tails of lipid-PEG dictate its dissociation rate from NP surface, determining the uptake by tumor cells and macrophages, pharmacokinetics, biodistribution, and gene silencing efficacy of these hybrid siRNA NPs. Based on our observations, we here propose that lipid-PEGs with long and saturated lipophilic tails might be required for effective siRNA delivery to tumor cells and gene silencing of the lipid-polymer hybrid NPs after systemic administration.

Key words: de-PEGylation, nanoparticle, self-assembly, siRNA delivery, cancer therapy.

## Introduction

Surface coating of poly(ethylene glycol) (PEG) has been extensively exploited to improve the pharmacokinetics (PK) of therapeutic nanoparticles (NPs) for cancer treatment, via significantly reducing the recognition of NPs by the mononuclear phagocyte system (MPS) [1-3]. With prolonged systemic circulation, PEGylated NPs have a higher chance to extravasate out of leaky tumor vasculature and accumulate in solid tumors through the enhanced permeability and retention (EPR) effect [4-6]. Notably, several PEGylated liposomes and polymeric NPs have been clinically approved for cancer therapy, and many are under clinical investigation [7-9]. Meanwhile, surface de-PEGylation might be equally

important for effective NP delivery into tumor cells due to various reasons [10, 11]. For instance, the surface PEG layer could negatively interfere with intracellular delivery of NPs [1, 11-13], which is particularly essential for the delivery of biomacromolecular therapeutics such as small interfering RNA (siRNA) that cannot readily cross cell membrane and require cytosolic transport for bioactivity [14-16]. Therefore, a balance between PEGylation and de-PEGylation is critical for siRNA NPs to simultaneously achieve both long-term blood circulation and sufficient intracellular uptake in the systemic delivery to tumors.

To address this dilemma, stimuli-triggered

de-PEGylation strategies have been developed by attaching PEG molecules on NP surface through labile bonds that are sensitive to the unique features of tumor microenvironment (TME) and/or intracellular environment, such as low pH, overexpressed enzymes, and altered redox potential [11, 17, 18]. Several pH-responsive linkers (e.g., orthoester [19], vinyl ether [20], and hydrazine [21-23]) were studied for the PEG shedding of NPs to enhance gene and drug delivery. Overexpressed enzymes in the tumor tissue (e.g., matrix metalloproteinase (MMP)) [24-27] and altered intracellular redox potential [28-32] were also explored as stimulating triggers. One example is the development of cleavable lipid-PEGs by conjugating PEG molecules and phospholipids together with a MMP substrate peptide [24, 25]. Lipid/siRNA NPs formulated with this cleavable lipid-PEG exhibited improved gene silencing efficacy in tumors as a result of enhanced cellular uptake and endosomal escape [25]. In addition, de-PEGylation can further be combined with other targeting or penetration-enhancing strategies for the development of multifunctional NPs [22, 23, 26, 32, 33]. *In vitro* proofs of concept have been well demonstrated for these PEG-shedding systems, and some also have been preliminarily tested in animal models [21, 23-25, 27, 32, 34-36]. For example, a recent work reported a pH-sensitive hydrazone linkage-mediated PEG shedding strategy for increased retention and high therapeutic efficacy of lipid/siRNA NPs in breast cancer mouse models [36]. Despite of all these advances, such stimuli-responsive de-PEGylation approaches might pose additional complexity in terms of design, synthesis, and scaling of therapeutic NPs [18].

Herein, we report a tunable and robust PEG shedding strategy mediated by serum albumin, and systematically investigate the effects of de-PEGylation on NP-mediated siRNA delivery *in vitro* and *in vivo*. The siRNA NP platform (Figure 1a) was formulated by self-assembling a lipid-PEG layer on the surface of a poly(lactide-co-glycolide) (PLGA) polymer core containing cationic lipid/siRNA complexes [37], via hydrophobic interactions between the lipophilic tails of lipid-PEG and the PLGA polymer. Albumin is the most abundant plasma protein and has been recognized as the main fatty acid transporter by providing different binding sites for fatty acids with moderate to high affinity, thus enhancing their solubility in aqueous solutions such as blood plasma and interstitial fluid [38, 39]. A recent work further demonstrated that albumin can bind avidly to diacyl lipids [40]. We thus hypothesized that the lipid-PEG molecules could dissociate from the hybrid NP surface in the presence of serum albumin, and the

dissociation kinetics may depend on the lipid-PEG properties. Our recent study discovered that the lipid segment (ceramide vs. DSPE) of lipid-PEG had a substantial effect on the de-PEGylation rate and the systemic circulation of the hybrid NPs, while PEG molecular weight might not be critical [37]. This observation inspired us to further clearly and systematically study how the lipid-PEG properties (e.g., lipid tail length, lipid tail saturation, and lipid charge) control the dissociation of lipid-PEGs from NP surface and affect siRNA NP delivery *in vitro* and *in vivo*, which we expect will provide significant insights for better understanding and design of the lipid-polymer hybrid NP platform. In this work, the de-PEGylation kinetics of eight lipid-PEG molecules with different alkyl chain length, saturation, and charge were measured with respective hybrid NPs. Furthermore, the tumor cell and macrophage uptake, gene silencing efficacy, and *in vivo* performance of these siRNA NPs were comprehensively examined and compared with the lipid-PEG dissociation rate. Results suggest that the alkyl chains of lipid-PEG determine the optimal de-PEGylation rates, by which the hybrid siRNA NPs can remain “stealth” long enough for high tumor extravasation and accumulation, and once reaching tumor tissue, can facilitate intracellular delivery to tumor cells for effective gene silencing.

## Results and Discussions

### Self-assembled lipid-polymer hybrid NPs

The lipid-polymer hybrid NPs loaded with siRNA were prepared through a robust and simple self-assembly nanoprecipitation method [37]. Aqueous siRNA was first mixed with water-miscible organic solution containing cationic lipid-like compound G0-C14 and PLGA polymer. The negatively charged siRNA molecules could then be self-assembled quickly with G0-C14 into lipid-siRNA nanocomplexes. Subsequently, the organic solution was rapidly added into an aqueous solution of lipid-PEG, in which the PLGA polymer and cationic lipid/siRNA complex were co-precipitated to form a solid polymeric NP core surrounded by a lipid-PEG shell (Figure 1a). Four polar aprotic solvents with different dielectric constants were tested for preparing the hybrid siRNA NPs, including dimethylformamide (DMF), dimethylsulfoxide (DMSO), acetone, and tetrahydrofuran (THF). As shown by the dynamic light scattering (DLS) results (Figure 1b), sub-100 nm NPs were obtained with DMF and DMSO, which possess relatively high dielectric constants. Larger NPs were formed when using solvents with lower dielectric constants (i.e., acetone and THF). This

observation is consistent with a previous study of developing similar lipid-polymer hybrid NPs for the delivery of chemotherapeutic drugs [41]. Low dielectric constant of a solvent implies its low polarity and poor water miscibility. Thus, when a low dielectric constant solvent is used, the organic solution of PLGA/nanocomplexes would have less efficient dispersion in the lipid-PEG aqueous solution. In the following studies, DMF was chosen for NP formulation, as the resulting smaller NPs may facilitate better tumor tissue accumulation through the EPR effect [42]. The hybrid siRNA NPs prepared with DMF also exhibited a spherical structure with a narrow size distribution as observed by TEM (Figure 1c).

### Kinetics of lipid-PEG dissociation

During the nanoprecipitation process, lipid-PEG would self-assemble on the NP surface through hydrophobic interactions between the lipophilic alkyl chains and the PLGA core. Different from covalently

conjugated PEG layer, physically adsorbed lipid-PEG molecules on NP surface are diffusible, which could thus result in de-PEGylation of the NPs over time. We hypothesized that both the assembly and the dissociation processes might be predominantly determined by the physicochemical properties of the lipid-PEG molecules. In this work, a series of eight lipid-PEGs with different alkyl chains and charges (Figure 2a) were used to evaluate their effect on the behaviors of the hybrid NPs for siRNA delivery, while keeping the PEG molecular weight (2 kDa) consistent. They are divided into two categories, neutral and anionic lipid-PEGs, according to the linkage (glycerol/serine vs. glycerol-3-phosphoethanolamine) between the lipophilic tails and the PEG chain. Both categories include three lipid-PEGs with saturated alkyl chains of different length (C14, C16 and C18) and one lipid-PEG with unsaturated chain(s) (ceramide or DOPE).

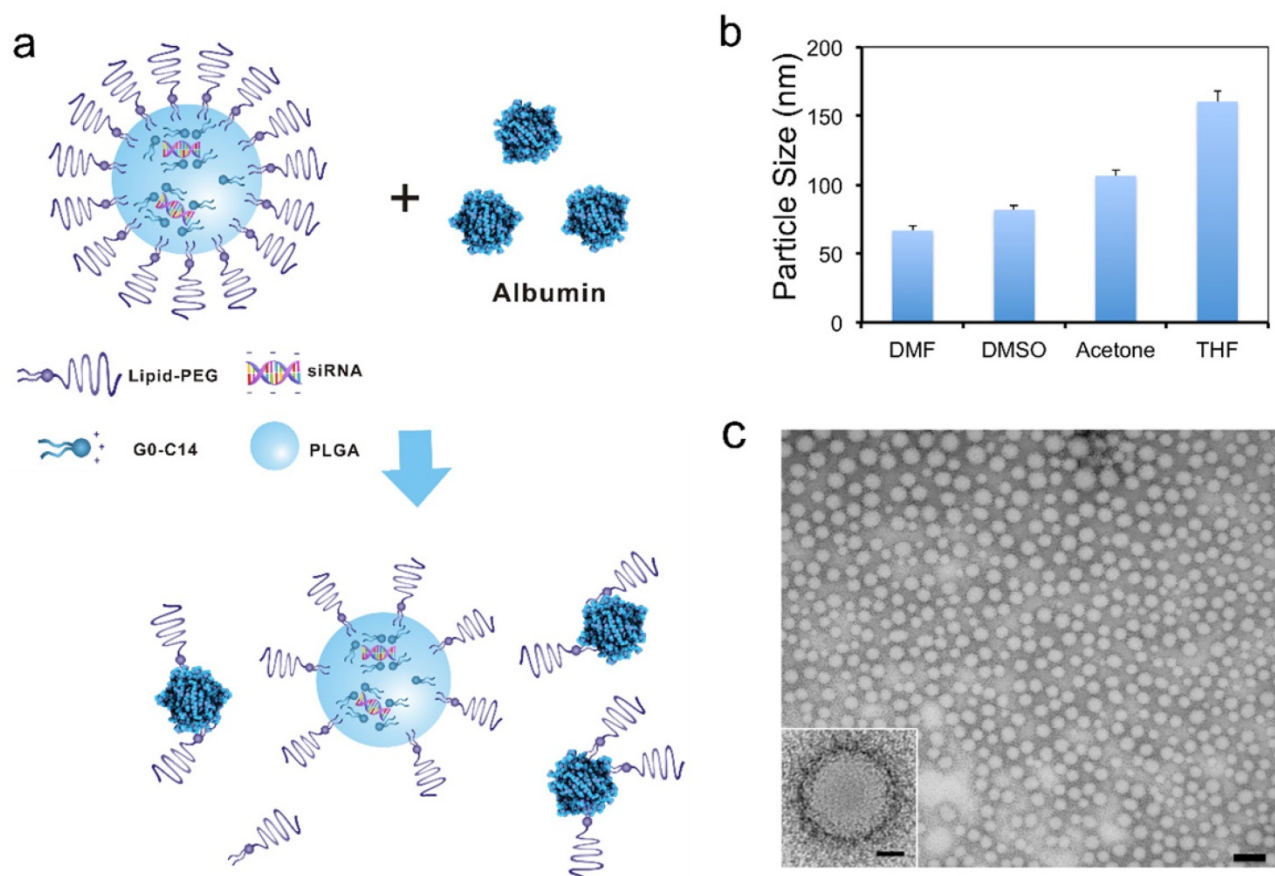


**Figure 1.** Lipid-polymer hybrid NPs for siRNA delivery. (a) Schematic of the NP structure and the lipid-PEG dissociation in the presence of serum albumin. (b) Size of the hybrid NPs prepared using different water-miscible organic solvents, as measured by DLS. (c) TEM image of the NPs prepared using DMF (scale bar: 100 nm). The scale bar is 20 nm for the insert image.

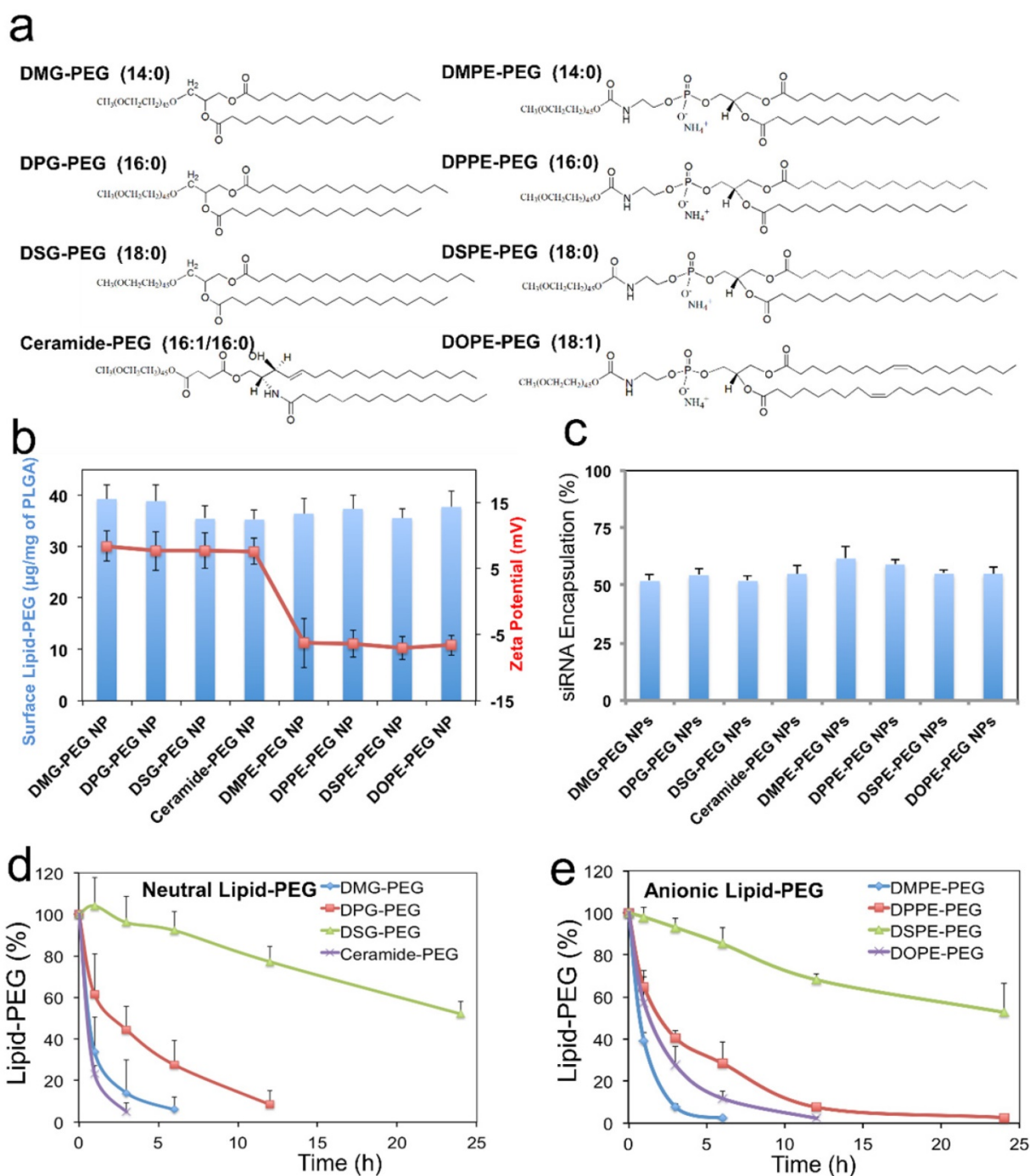


**Figure 2.** Effect of lipid-PEG on the properties and de-PEGylation of the hybrid siRNA NPs. (a) Chemical structure of eight different lipid-PEGs. (b) The amount of surface lipid-PEG relative to the PLGA polymer weight and the surface charge (zeta potential) on different NPs. (c) siRNA encapsulation efficiency of the NPs with different lipid-PEGs. Dissociation kinetics of (d) neutral lipid-PEGs and (e) anionic lipid-PEGs from respective NPs in the presence of serum albumin.

We first quantified the amount of lipid-PEG that self-assembled on the NPs using a method based on the spectrophotometric measurement of complexes formed by PEG and barium iodide [43, 44]. All NPs carried a similar amount of lipid-PEGs on the surface, which was  $\sim 35$ – $40$   $\mu\text{g}/\text{mg}$  of the PLGA polymer (Figure 2b). It is worth noting that this self-assembly nanoprecipitation method requires no surfactant/stabilizer (e.g., polyvinyl alcohol) in the

hybrid NP formulation, which was reported to significantly impede lipid-PEG association on the polymeric particle surface as a steric barrier [45]. This high surface lipid-PEG density may thus increase the NP stability in serum and reduce MPS recognition. The hybrid NPs prepared with neutral vs. anionic lipid-PEGs also carried different surface charges (Figure 2b). The NPs coated with neutral lipid-PEGs showed mildly positive zeta potential ( $\sim 8$  mV), while

those with anionic lipid-PEGs exhibited mildly negative charges ( $\sim -7$  mV). The choice of lipid-PEGs also had no significant influence on the particle size ( $\sim 60$ -70 nm) and the encapsulation efficiency of siRNA, which was  $\sim 50$ -60% for all the NPs (Figure 2c) as measured using fluorophore labeled siRNA (DY547-siRNA).

Considering that albumin is the main plasma protein in blood and has a strong binding with diacyl lipids [40], we utilized 4 w/v% serum albumin in phosphate buffered saline (PBS) to investigate the role of albumin on the de-PEGylation of the hybrid siRNA NPs. While all lipid-PEGs dissociated from NPs over time as shown in Figure 2d-e, the rate of dissociation was drastically different. For lipid-PEGs with saturated tails in both neutral and anionic categories, shorter alkyl chains resulted in faster dissociation. For example, after 24 h incubation with albumin, over 50% of DSG-PEG and DSPE-PEG (with C18 alkyl chains) were still remained on NP surfaces. As a comparison, the amount of DMG-PEG and DMPE-PEG (with C14 alkyl chains) dwindled below the detection limit after 6-12 h. This phenomenon might be explained by the higher phase transition temperature and lower fluidity of the lipid tails with longer saturated alkyl chains, which could result in stronger hydrophobic interactions with the PLGA core. Interestingly, much faster dissociation was observed for the unsaturated lipid-PEGs than the saturated ones with the same length of alkyl chain (ceramide vs. DPG, or DOPE vs. DSPE). DOPE-PEG, which carries two unsaturated C18 alkyl chains, was released at a rate even faster than DPPE-PEG with two saturated C16 alkyl chains. Similarly, ceramide-PEG (with one unsaturated C16) was released faster than DMG-PEG (saturated C14). This may be attributed to the fact that the unsaturation on alkyl chain can lower the chain melting transition temperature, and thus increase the lipid fluidity [46]. On the other hand, neutral and anionic lipid-PEGs with the same alkyl chains showed similar dissociation kinetics, suggesting that the charge in the linkage group between PEG and alkyl chains had negligible effect on the de-PEGylation of these NPs. We also calculated the dissociation rate constants ( $k_d$ ) and half-lives ( $t_{1/2}$ ) of the eight lipid-PEGs from respective NPs by fitting the dissociation profiles in Figure 2d-e to a first-order dissociation model (Table 1).

To further clarify the important role of albumin in de-PEGylation of the hybrid NPs, two anionic lipid-PEG NPs with the fastest vs. slowest dissociation rate (i.e. DMPE and DSPE) were chosen as models for further de-PEGylation study in PBS without albumin. As shown in Figure S1a, the de-PEGylation rates in the PBS control group were drastically reduced as

compared to that in PBS containing 4 w/v% albumin (Figure 2e), suggesting that the de-PEGylation effect for our hybrid NPs could be closely related with the presence of albumin. In addition, the de-PEGylation kinetics in FBS, which contains albumin and a number of other proteins and can more closely mimic the blood, were determined with DMPE-PEG and DSPE-PEG NPs (Figure S1b). The similar lipid-PEG dissociation rates to those in PBS containing albumin (Figure 2e) further provide evidences for the strong effect of albumin on de-PEGylation. It is also worth mentioning that other factors such as the sheer force of blood flow may also have potential effect on the dissociation of lipid-PEG.

**Table 1.** The dissociation rate constant ( $k_d$ ) and dissociation half-life ( $t_{1/2}$ ) of different lipid-PEGs from respective NPs

Neutral Lipid-PEG		DMG-PEG	DPG-PEG	DSG-PEG	Ceramide-PEG
	$K_d$ ( $h^{-1}$ )	0.52	0.21	0.025	1.05
	$T_{1/2}$ (h)	1.33	3.30	27.73	0.66
Anionic Lipid-PEG		DMPE-PEG	DPPE-PEG	DSPE-PEG	DOPE-PEG
	$K_d$ ( $h^{-1}$ )	0.68	0.17	0.028	0.33
	$T_{1/2}$ (h)	1.02	4.08	24.76	2.10

### Effect of lipid-PEG on *in vitro* siRNA delivery

For *in vitro* evaluation of the hybrid siRNA NPs with different surface lipid-PEGs, a firefly luciferase-expressed HeLa cell line (Luc-HeLa) was used. The hybrid siRNA NPs without lipid-PEG coating was also used as a control. The cells were first transfected with NPs loaded with luciferase siRNA (siLuc). The reduction of luciferase expression was then measured to evaluate the siLuc NP-mediated silencing efficiency. Figure 3a show that the lipid-PEG plays a vital role in determining the silencing performance *in vitro*. All NPs exhibited silencing activity in a dose-dependent manner. At a siRNA concentration of 50 nM, most of the NPs demonstrated a nearly complete ( $> 95\%$ ) luciferase knockdown and they were significantly more effective than the commercial transfection reagent lipofectamine 2000 (Lipo2000), except the DSPE-PEG and DOPE-PEG NPs. The  $IC_{50}$  for *in vitro* silencing mediated by different NPs was calculated using the Phoenix® WinNonlin software (Figure 3b). In both neutral and anionic lipid-PEG categories, the NPs with faster lipid-PEG dissociation generally exhibited lower  $IC_{50}$ . It is also noteworthy that neutral lipid-PEG NPs exhibited higher silencing efficacy compared with their anionic counterparts, although similar lipid-PEG dissociation profiles were observed (Figure 2d-e). As a comparison, the PLGA/G0-C14 siRNA NPs (without PEGylation) showed slightly better or comparable *in vitro* knockdown efficiency

than the neutral lipid-PEG NPs with fast de-PEGylation rates (Figure S2).

To understand the effect of lipid-PEG on *in vitro* silencing, we explored the uptake kinetics of the hybrid NPs loaded with DY547-siRNA in Luc-HeLa cells. Similar to the silencing results, the NPs with faster dissociation of saturated lipid-PEGs exhibited higher cellular internalization for both lipid-PEG categories, and the non-PEGylated PLGA/G0-C14 siRNA NPs also showed very high cellular internalization (Figure 4a-c and Figure S3). The neutral lipid-PEG NPs also showed higher cellular uptake compared to their anionic counterparts at 24 h. This could be explained by the surface charge difference of these NPs, as negatively charged NPs (with anionic lipid-PEGs) generally have less interaction with cell membranes than positively charged ones (with neutral lipid-PEGs). For the NPs coated with saturated lipid-PEGs, the cellular uptake result displayed similar trend with that of the silencing experiments, suggesting that the hybrid NPs with higher cellular uptake may potentially result in

better luciferase silencing in Luc-HeLa cells. In addition to tumor cells, we also investigated the uptake of these NPs by macrophage cells (RAW264.7), which represent a major cell type in the MPS system for clearance of exogenous NPs. As shown in Figure 4d, the effect of lipid-PEGs on the macrophage uptake of NPs was consistent with that on Luc-HeLa cells. To further understand the correlation between the lipid-PEG dissociation and cellular uptake, we plotted the  $k_d$  of different lipid-PEGs against the corresponding amount of NP taken up by Luc-HeLa or macrophage cells (Figure 4e-f). Positive correlation was observed between the  $k_d$  and the cellular uptake for lipid-PEGs with saturated alkyl tails in both neutral and anionic categories, but not for unsaturated ceramide-PEG and DOPE-PEG. This study also indicates that a compromise between high tumor cell uptake (for efficient gene silencing) and low macrophage recognition (for long blood circulation) may be needed especially for the non-targeted hybrid siRNA NPs to achieve optimal *in vivo* silencing.

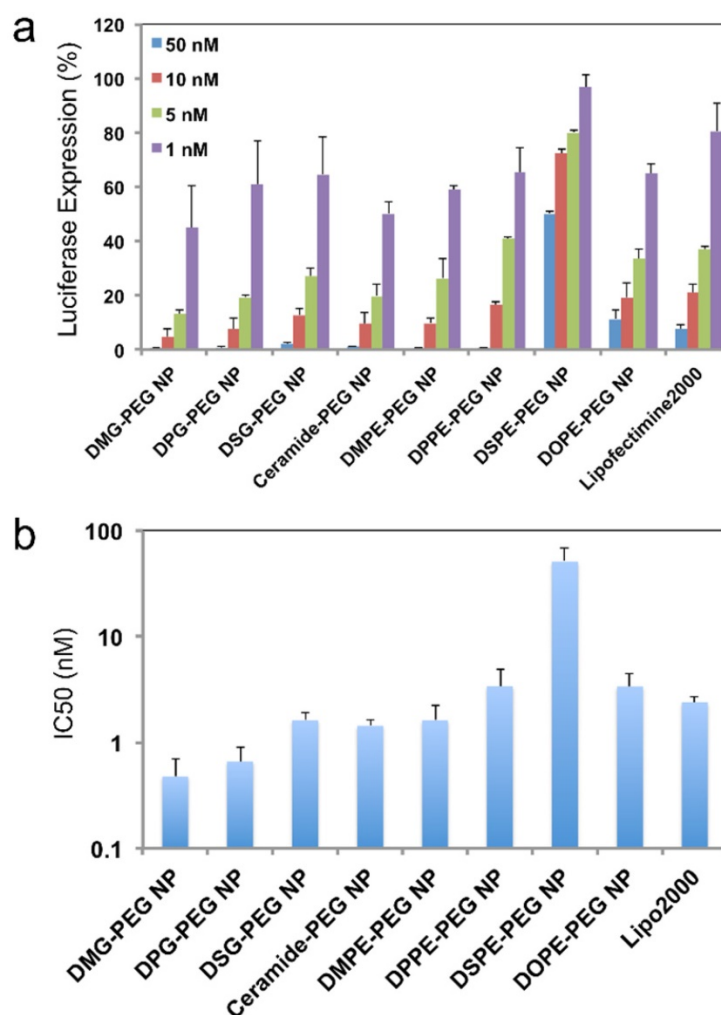


**Figure 3.** *In vitro* silencing efficacy of the hybrid NPs. (a) Luciferase expression in Luc-HeLa cells treated with NP (siLuc) composed of different lipid-PEGs. Lipo2000 was used as a positive control. (b) IC50 for the *in vitro* luciferase silencing from (a).

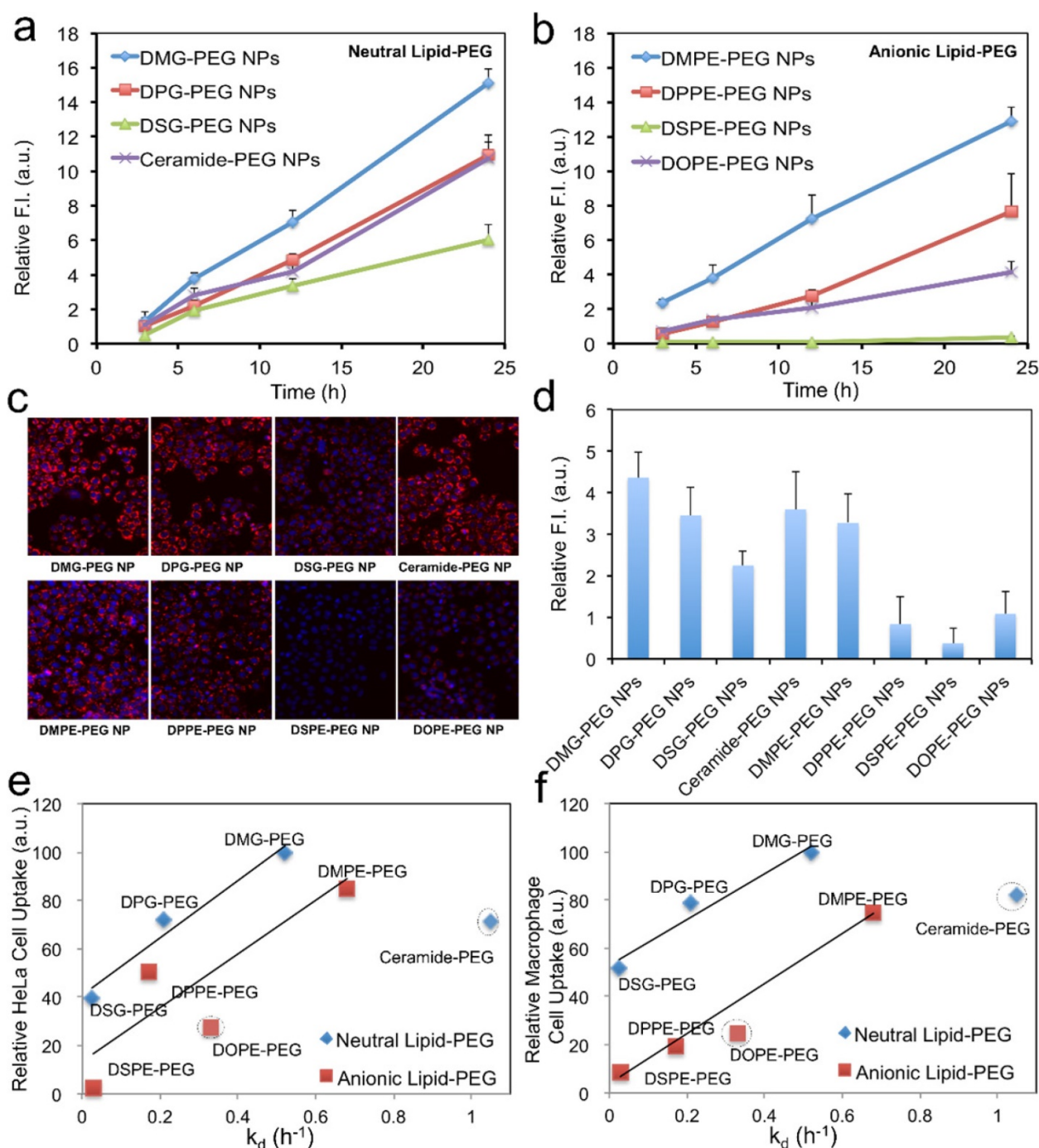


**Figure 4** Effect of lipid-PEG on NP uptake by tumor cells and macrophage cells. Uptake kinetics of siRNA NPs with (a) neutral and (b) anionic lipid-PEGs on Luc-HeLa cells. (c) Representative fluorescence images for the tumor cell uptake of NP (DY547-siRNA) with different lipid-PEGs after 24 h incubation. (d) NP uptake on macrophage cells (RAW264.7) after 12 h incubation. The correlation of (e) Luc-HeLa cell uptake and (f) macrophage cell uptake with the dissociation rate constant ( $k_d$ ) of different lipid-PEGs.

### Effect of lipid-PEG on systemic *in vivo* siRNA delivery

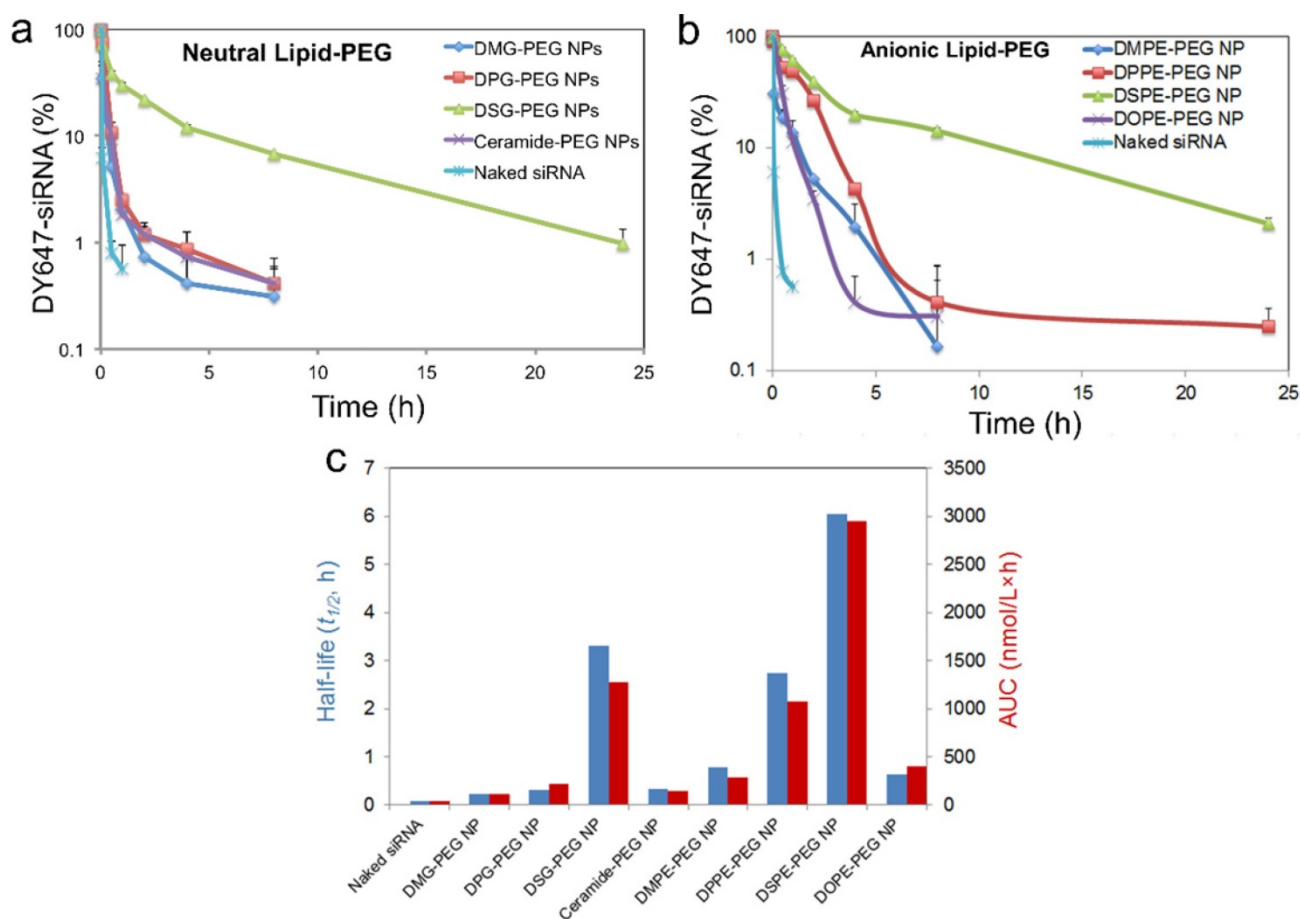
To assess the *in vivo* performance of these hybrid NPs for siRNA delivery, we first examined the PK by injecting NP (DY647-siRNA) to normal C57BL/6 mice through the tail vein. NPs with different lipid-PEGs were evaluated and compared with naked siRNA.

Figure 5a-b shows that naked siRNA was rapidly cleared from the systemic circulation within 30 min, while siRNA NPs stayed longer in blood. Drastically different PK behaviors were observed among these NPs and between the neutral and anionic categories. For the NPs coated with neutral lipid-PEGs, only the DSG-PEG NP exhibited a long circulation half-life ( $t_{1/2}$ ) ~ 3.3 h. All the other three NPs showed a  $t_{1/2}$  less

than 20 min (Figure 5c). The NPs with anionic lipid-PEGs demonstrated much longer circulation than the neutral counterparts. The trend found in the PK study for anionic lipid-PEG NPs analogously resembled that observed in the dissociation study. DSPE-PEG NPs exhibited the most impressive circulation property with  $t_{1/2} \sim 6$  h, and the area under the curve (AUC) is  $\sim 68$ -fold of that for naked siRNA (Figure 5c). Besides, NPs with unsaturated ceramide-PEG and DOPE-PEG exhibited relatively rapid blood clearance, as well as the bare PLGA NPs in the control group which were cleared more easily (Figure S4).

Next we checked the biodistribution (BioD) and tumor accumulation of the hybrid siRNA NPs upon intravenous (IV) injection into mice bearing subcutaneous Luc-HeLa tumor xenograft. As we have learned that, due to the EPR effect, NPs with long circulation lives could have higher chance to accumulate in tumor tissues than NPs with short PK [47-50]. Therefore, we herein selected all the three NPs with relatively long blood circulation (DOPE-PEG, DPPE-PEG, and DSPE-PEG NPs), and two NPs with short circulation (ceramide-PEG and DSG-PEG) and

naked siRNA as controls. For fluorescence imaging, the siRNA was labeled with near infrared dye DY677. Twenty-four hours post-IV injection, major organs and tumors were harvested and imaged (Figure 6a). It was observed that naked siRNA had low accumulation in all tissues except kidney. The NPs with longer circulating  $t_{1/2}$  generally led to higher tumor accumulation. This can be explained by the fact that only the NPs that were not rapidly cleared from the circulation will have a chance to encounter the leaky tumor vasculature. NPs prepared with DSG-PEG, DOPE-PEG, and DPPE-PEG achieved similar tumor accumulation, which is  $\sim 4.7$ - $6.1$ -fold higher than that of naked siRNA (Figure 6b). DSPE-PEG NPs with the longest circulating  $t_{1/2}$  exhibited a 14.5-fold higher tumor accumulation than naked siRNA. In comparison, the short-circulating ceramide-PEG NPs only increased the siRNA accumulation by a 2.2-fold. Interestingly, the NPs coated with neutral ceramide-PEG or DSG-PEG demonstrated a higher lung accumulation vs. other NPs. Further investigation on this observation might lead to other potential applications of the hybrid NPs.



**Figure 5.** Effect of lipid-PEG on PK of the hybrid siRNA NPs. (a, b) Circulation profile of naked siRNA and different siRNA NPs composed of neutral or anionic lipid-PEGs in normal C57BL/6 mice after IV injection. siRNA was labeled with fluorophore DY647. (c) Circulation half-life and AUC of naked siRNA and siRNA NPs composed of different lipid-PEGs.

The *in vivo* silencing efficacy of these hybrid siRNA NPs was also evaluated on athymic nude mice bearing subcutaneous Luc-HeLa xenograft tumor. The mice received daily IV injection of naked siLuc or NP (siLuc) for three consecutive days. Three NPs (DSG-PEG, DPPE-PEG, and DSPE-PEG) with relatively long blood circulation and high tumor accumulation, and one NP (ceramide-PEG) with low tumor accumulation, were selected in this study. Two days after the final injection, each mouse was injected intraperitoneally with 2 mg of D-Luciferin, and 5 min later, the animal was imaged for bioluminescence (Figure 6c). For quantification analysis, the animals were sacrificed, and then the protein extracts of tumor tissue were prepared using lysis buffer to measure the firefly luciferase level (Figure 6d). As can be seen, the animals treated with the rapidly cleared ceramide-PEG NPs exhibited an insignificant reduction of the luciferase level compared to those treated with naked siRNA. DSG-PEG and DPPE-PEG

NPs, which exhibited excellent *in vitro* silencing effect and relatively long blood circulation, were both effective in reducing bioluminescence intensity, and led to ~ 50% luciferase silencing *in vivo*. Interestingly, for DSPE-PEG NP, despite its low *in vitro* silencing efficiency (Figure 3a), ~ 40% knockdown of luciferase expression was achieved in tumor tissues. We speculated that the *in vivo* dissociation of lipid-PEG from NP surface might be faster than that *in vitro* owing to the more complicated environment and the blood flow. Our observations suggest that the *in vivo* gene silencing efficacy may depend on different aspects of the NPs, and neither *in vitro* data nor *in vivo* PK/BioD alone could be used to predict the *in vivo* efficacy. From these results, we postulate that lipid-PEGs with long and saturated lipophilic tails may be required for the lipid-polymer hybrid siRNA NPs to achieve effective gene silencing in tumor tissues after systemic administration.

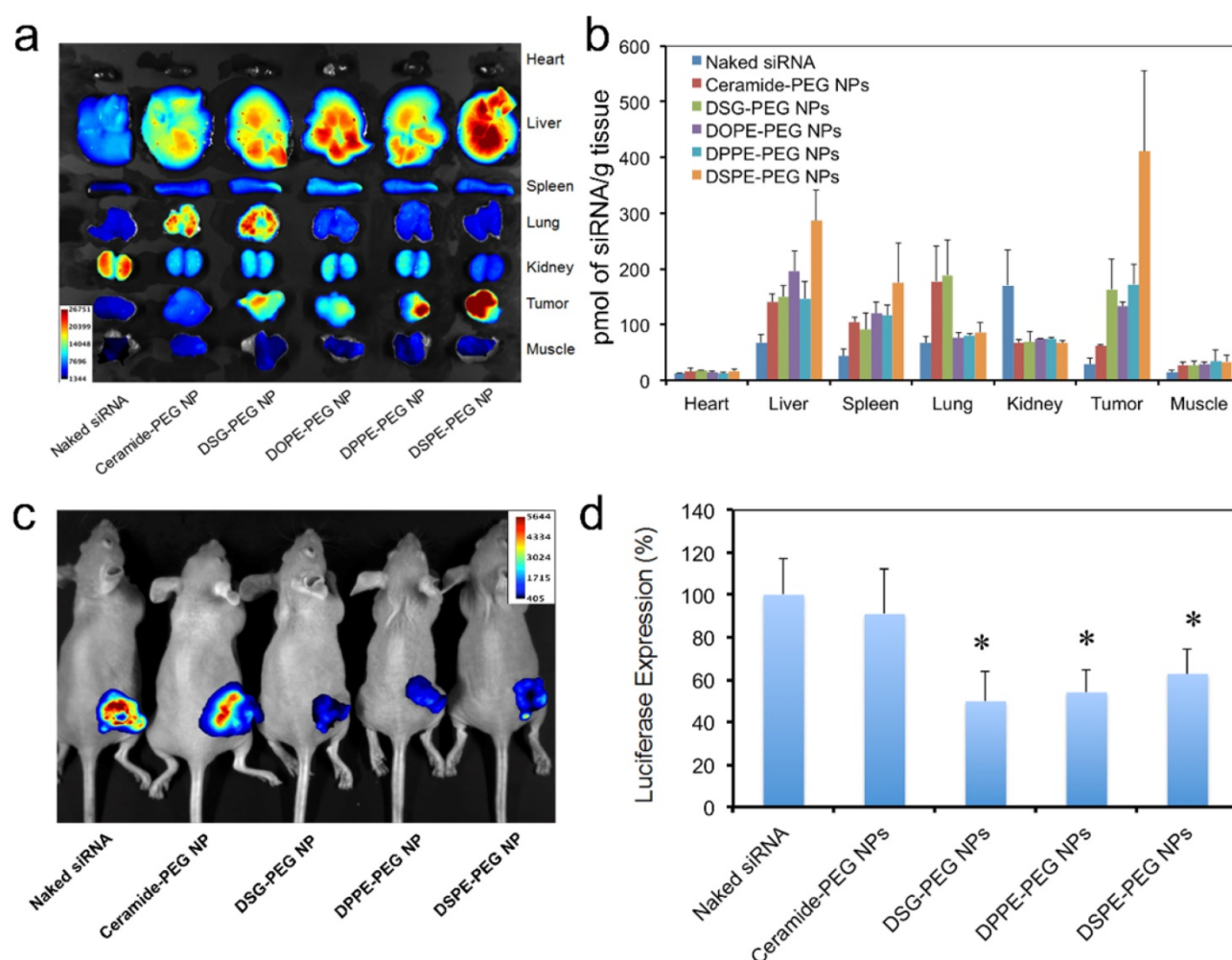


**Figure 6.** Biodistribution and *in vivo* gene-silencing efficacy. (a) *Ex vivo* fluorescence image of the tumor and major organs from athymic nude mice bearing Luc-HeLa tumor treated with naked DY677-siRNA vs. NP (DY677-siRNA) with different lipid-PEGs. (b) Quantitative analysis of biodistribution of NP (siRNA) in different tissues and the Luc-HeLa tumor (n=3). (c) *In vivo* bioluminescence imaging of mice bearing Luc-HeLa tumor following IV injection of free siLuc or NP (siLuc) for 3 consecutive days. Images were taken at 5 min after intraperitoneal injection of 2 mg of D-Luciferin per mouse. (d) Luciferase expression in the protein extracts of tumor tissue treated with NP (siLuc) vs. naked siLuc (n=4; \*  $p < 0.05$  vs. naked siRNA).

## Conclusions

Surface PEGylation can facilitate the long systemic circulation of therapeutic NPs by lowering MPS clearance and thus enhance NP extravasation into tumor tissues through the EPR effect, while de-PEGylation favors the intracellular transport of NPs, a critical step in the delivery of biomacromolecules such as siRNA to tumor cells. Therefore, when taking these factors into consideration, the PEG dissociation from NP surface needs to be carefully explored for optimal gene silencing in tumors. With the hybrid siRNA NP platform, we systematically investigated the effects of de-PEGylation on siRNA delivery. The lipid-PEG dissociation, which was controlled by the physicochemical characters of its lipid tails, correlated with the cellular uptake, gene silencing, and *in vivo* performance of these siRNA NPs. By selecting different lipid-PEGs in the NP formulation, the *in vitro* and *in vivo* behaviors of the hybrid siRNA NP system could be easily manipulated.

Different from the stimuli-triggered de-PEGylation strategies, our alternative approach avoids the design of TME stimuli-responsive chemistry, which may introduce additional complexities in the synthesis and scale-up of therapeutic NPs. Notably, the self-assembly of lipid-PEGs on the hybrid NP surface is also very robust, thus offering a convenient approach for high-throughput screening of lipid-PEG molecules. The optimization of other factors, such as the PEG length and the combination of multiple different lipid-PEGs, may further lead to better *in vivo* efficacy of the hybrid RNAi NPs. By enabling effective silencing of specific genes in tumor tissues following systemic administration, this NP platform could serve as a robust toolkit for fundamental cancer research and rapid *in vivo* validation of potential therapeutic targets in cancer pathogenesis, in particular those considered as 'undruggable'. In addition, the hybrid siRNA NPs can also simultaneously encapsulate small molecular drugs (e.g., taxanes and cisplatin prodrugs) within the PLGA polymer core[51-53], and the co-delivery of siRNA and drug combinations is expected to have a synergistic anti-tumor effect[33, 54]. In summary, we successfully demonstrated that surface lipid-PEG dissociation controls the *in vitro* and *in vivo* performance of the lipid-polymer hybrid siRNA NPs, and we expect this robust NP platform to be highly useful in cancer research and treatment.

## Materials and methods

### Materials

Methoxy-terminated DMPE-PEG, DPPE-PEG,

DSPE-PEG, DOPE-PEG, and ceramide-PEG were obtained from Avanti Polar Lipids, and methoxy-terminated DMG-PEG, DPG-PEG, and DSG-PEG were from NOF American. The PEG molecular weight is 2 kDa. Ethylenediamine core-poly (amidoamine) (PAMAM) generation 0 dendrimer (G0), D-Luciferin, and bovine serum albumin were purchased from Sigma-Aldrich. Ester-terminated poly(D,L-lactide-co-glycolide) (PLGA, viscosity of 0.26-0.54 dL/g) was obtained from Durect Corporation. Iodine solution was obtained from Alfa Aesar. Transfection agent lipofectamine2000 (Lipo2000) was purchased from Invitrogen. Steady-Glo luciferase assay system was purchased from Promega. Luciferase siRNA (siLuc) and fluorophore-labeled siRNA (DY547-siRNA, DY647-siRNA, and DY677-siRNA) were acquired from Dharmacon. The siLuc sequence is: 5'-CUU ACG CUG AGU ACU UCG AdTdT-3' (sense) and 5'-UCG AAG UAC UCA GCG UAA GdTdT-3' (antisense). DY547 and DY647 were labeled at the 5'-end of the sense strand of siLuc. DY677 was labeled at the 5'-end of both the sense and antisense strands of siLuc.

### Synthesis of G0-C14 compound

Cationic lipid-like G0-C14 compound was synthesized by the ring opening reaction of alkyl epoxides with PAMAM, according to a previously described procedure.[52, 55] PAMAM G0 and 1,2-epoxytetradecane were mixed at a molar ratio of 1:7, and reacted under vigorous stirring at 90 °C for 48 h. The crude reaction mixture was purified by silica chromatography with a gradient elution from CH<sub>2</sub>Cl<sub>2</sub> to 75:22:3 CH<sub>2</sub>Cl<sub>2</sub>/MeOH/NH<sub>4</sub>OH.

### Preparation and characterization of lipid-polymer hybrid siRNA NPs

The lipid-polymer hybrid siRNA NPs were formulated by a self-assembly nanoprecipitation method we recently developed with modifications [37]. In brief, 5 mg PLGA and 0.5 mg G0-C14 are dissolved in 1 mL organic solvent (e.g., DMF). A 50 µL siRNA (4 nmoles) aqueous solution is mixed with the organic solution by pipetting to form siRNA/G0-C14 nanocomplexes. Next, the organic solution with the nanocomplexes and polymers was added into a 20 mL aqueous solution containing 2 mg lipid-PEG (e.g., DSG-PEG). 0.2 mL of phosphate buffered saline (PBS) was subsequently added to stabilize the formed NPs. The suspension was then stirred at room temperature for 30 min. The hybrid NPs were finally washed in Amicon tubes (MWCO 100kDa; Millipore) to remove remaining organic solvents and free compounds with ice-cold water, and concentrated in 1 mL PBS solution. The PLGA/G0-C14 siRNA NPs without PEGylation

were prepared with the same method except that lipid-PEGs were replaced with stabilizer polyvinyl alcohol (0.5%, w/v). The particle size and surface charge (zeta potential) were determined by dynamic light scattering (DLS; 15-mW laser incident beam of 676 nm; Brookhaven Instruments Corporation). NP samples for transmission electron microscopy (TEM) imaging were stained with 1% uranyl acetate and imaged by a Tecnai G<sup>2</sup> Spirit BioTWIN microscope (FEI Company) operating at 80 kV.

### **Lipid-PEG quantification and dissociation kinetics**

The amount of lipid-PEG molecules on NP surface and the dissociation of lipid-PEG from NPs in PBS (with 4 w/v% bovine serum albumin), PBS without albumin, or FBS were quantified based on the spectrophotometric measurement of complexes formed between PEG and barium iodide [44]. For quantification of surface lipid-PEG amount, the freshly prepared NP solution after 30 min stirring was directly ultra-centrifuged and the pellet was re-suspended in water for reaction with the barium iodide solution (100  $\mu$ L DMSO, 20  $\mu$ L BaCl<sub>2</sub> (5%) and 20  $\mu$ L I<sub>2</sub> solution (0.1 N)). For the dissociation kinetics study, NPs were first incubated with PBS (with 4 w/v% bovine serum albumin), PBS without albumin, or FBS at 37 °C. At predetermined time points, NP suspension was ultra-centrifuged to remove supernatant, and the NP pellet was re-suspended in water. Then 100  $\mu$ L of NP solution (1.25 mg/ml at PLGA polymer weight) was mixed with 100  $\mu$ L DMSO, 20  $\mu$ L BaCl<sub>2</sub> (5 %) and 20  $\mu$ L I<sub>2</sub> solution (0.1 N). Calibration curve was prepared with corresponding lipid-PEG solution with same concentration of PLGA (1.25 mg/ml) and G0-C14 (0.125 mg/ml). After incubation at room temperature for 15 min, absorbance at 535 nm was measured on the microplate reader.

### **Cell culture**

Firefly luciferase-expressing HeLa (Luc-HeLa) and RAW264.7 macrophage were maintained in Dulbecco's Modified Eagle's Medium (DMEM; Invitrogen) with high glucose, 10% (v/v) fetal bovine serum (FBS; Gibco). Both cells were incubated at 37°C in 5% CO<sub>2</sub>.

### **In vitro luciferase silencing**

Luc-HeLa cells were seeded into 96-well plates (5,000 cells per well) and allowed to attach in cell culture medium at 37°C in a 5% CO<sub>2</sub> incubator overnight. Cells were then transfected with NPs or Lipo2000-siLuc complexes at siRNA concentration of 50 nM, 10 nM, 5 nM, and 1 nM for 24 h. Lipo2000-siLuc complexes were prepared according

to the manufacturer's protocol. Luc-HeLa cells were then washed with fresh medium and further cultured in medium for another 48 h. The expression of luciferase in HeLa cells was determined using Steady-Glo luciferase assay kits. Cell number was measured using AlamarBlue assay. The luminescence/fluorescence intensity was measured using a microplate reader. All the *in vitro* transfection experiments were performed in triplicate.

### **NP uptake**

For cellular uptake kinetics study, HeLa or RAW264.7 cells were seeded into 96-well plates and allowed to attach for 24 h. Next, the cells were incubated with NP (DY547-siRNA) at the siRNA concentration of 50 nM for different periods of time (3, 6, 12, and 24 h), and then washed with PBS, fixed with 4% paraformaldehyde, and stained with Hoechst 33342 (2  $\mu$ g/ml) for nuclei identification. Images were acquired on an inverted Fluorescence Microscope (Zeiss Axiovert 200) and analyzed using Fiji/Image-J software.

### **Animals**

All *in vivo* studies were performed in accordance with National Institutes of Health animal care guidelines and in strict pathogen-free conditions in the animal facility of Brigham and Women's Hospital. Animal protocol was approved by the Institutional Animal Care and Use Committees on animal care (Harvard Medical School). Mice were obtained from Charles River Laboratories. The animals were allowed free access to sterile food pellets and water.

### **Pharmacokinetic study**

For pharmacokinetic study, normal C57BL/6 mice were intravenously injected with fluorophore (DY647)-labeled siRNA NPs or naked DY647-siRNA through the tail vein. At different time points, blood was drawn retro-orbitally and siRNA fluorescence was measured using the BioTek microplate reader. Standard curve was generated by measuring the fluorescence intensity of different amounts of NP (DY647-siRNA) or free DY647-siRNA added in blood from untreated mice. The total blood volume was estimated as 58.5 ml blood per kg of bodyweight.

### **Luc-HeLa tumor xenograft model**

For the establishment of Luc-HeLa tumor xenograft model, 3 $\times$ 10<sup>6</sup> cells were suspended in 1:1 (v/v %) serum free media and Matrigel (BD Biosciences), and implanted subcutaneously into the flank of 5-week-old female athymic nude mice.

### **Biodistribution**

For biodistribution study, female athymic nude

mice bearing Luc-HeLa tumor were administered with (DY677)-labeled siRNA NPs or naked DY677-siRNA through the lateral tail vein injection. The mice were sacrificed 24 h after administration, and organs and tumors were harvested and imaged using the Syngene PXi imaging system (Synoptics Ltd). To quantify the accumulation of siRNA, organs and tumors harvested from mice were weighted and homogenized. Fluorescent intensity of the homogenate was measured using the Syngene PXi imaging system and quantified by Image-J [56].

### **In vivo luciferase silencing**

To evaluate *in vivo* silencing efficacy, female athymic nude mice bearing Luc-HeLa tumor were administered daily by IV injection of free siLuc or NP (siLuc) at a dose of 1.2 mg siRNA per kg of animal weight, for three consecutive days. Two days after the final injection, the animals were anesthetized and injected intraperitoneally with of 2 mg of D-Luciferin per mouse. Five minutes later, the animals were imaged for the bioluminescence using the Syngene PXi imaging system. For quantification analysis, the animals were sacrificed, and then the protein extracts of tumor tissue were prepared using lysis buffer. The luciferase level was measured using the Steady-Glo luciferase assay kit, and the total protein was quantified using BCA assay.

### **Statistical analysis**

Data are presented as mean  $\pm$  S.D., unless otherwise stated. Statistical analysis was performed using two-tailed student's *t* test. A *p*-value < 0.05 is considered statistically significant.

### **Supplementary Material**

Supplementary figures.

<http://www.thno.org/v07p1990s1.pdf>

### **Abbreviations**

siRNA: small interfering RNA

NP: nanoparticle

PEG: poly(ethylene glycol)

PK: pharmacokinetics

MPS: mononuclear phagocyte system

EPR: enhanced permeability and retention

TME: tumor microenvironment

MMP: matrix metalloproteinase

PLGA: poly(lactide-co-glycolide)

DMF: dimethylformamide

DMSO: dimethylsulfoxide

THF: tetrahydrofuran

DLS: dynamic light scattering

siLuc: luciferase siRNA

PBS: phosphate buffered saline

FBS: fetal bovine serum

DMEM: Dulbecco's Modified Eagle's Medium

$k_d$ : dissociation rate constant

$t_{1/2}$ : half-life

Lipo2000: lipofectamine 2000

DMPE: 1,2-Dimyristoyl-sn-glycero-3-phosphoethanolamine

DPPE: 1,2-Dipalmitoyl-sn-glycero-3-phosphoethanolamine

DSPE: 1,2-Distearoyl-sn-glycero-3-phosphoethanolamine

DOPE: 1,2-Dioleoyl-sn-glycero-3-phosphoethanolamine

DMG: 1,2-Dimyristoyl-sn-glycerol, methoxypolyethylene glycol

DPG: 1,2-Dipalmitoyl-sn-glycerol, methoxypolyethylene glycol

DSG: 1,2-Distearoyl-sn-glycerol, methoxypolyethylene glycol

PAMAM: Ethylenediamine core-poly (amidoamine)

G0-C14: Epoxytetradecane-modified PAMAM generation 0 dendrimer

TEM: Transmission Electron Microscopy

### **Acknowledgements**

This work was in part supported by the DoD grant (W81XWH-15-1-0728), the NIH grants (R00CA160350 and CA200900), the Movember-Prostate Cancer Foundation (PCF) Challenge Award, the David Koch-PCF program in nanotherapeutics, the J. Eustace Wolfington-PCF Young Investigator Award, the Shanghai Sailing Program (16YF1411300), and the Technology Development Grant of Pudong New Area (PKF2014-C01).

### **Competing Interests**

O.C.F. has financial interests in Selecta Biosciences, Tarveda Therapeutics and Placon Therapeutics. Other authors declare no competing financial interests.

### **References**

- [1] Knop K, Hoogenboom R, Fischer D, Schubert US. Poly(ethylene glycol) in drug delivery: pros and cons as well as potential alternatives. *Angew Chem Int Ed Engl.* 2010;49:6288-308.
- [2] Guo X, Huang L. Recent advances in nonviral vectors for gene delivery. *Acc Chem Res.* 2012;45:971-9.
- [3] Walkey CD, Olsen JB, Guo H, Emili A, Chan WC. Nanoparticle size and surface chemistry determine serum protein adsorption and macrophage uptake. *J Am Chem Soc.* 2012;134:2139-47.
- [4] Matsumura Y, Maeda H. A new concept for macromolecular therapeutics in cancer chemotherapy: mechanism of tumorotropic accumulation of proteins and the antitumor agent smancs. *Cancer Res.* 1986;46:6387-92.
- [5] Bertrand N, Wu J, Xu X, Kamaly N, Farokhzad OC. Cancer nanotechnology: the impact of passive and active targeting in the era of modern cancer biology. *Adv Drug Deliver Rev.* 2014;66:2-25.
- [6] Tao W, Zhang J, Zeng X, Liu D, Liu G, Zhu X, et al. Blended nanoparticle system based on miscible structurally similar polymers: a safe, simple, targeted, and surprisingly high efficiency vehicle for cancer therapy. *Adv Healthc Mater.* 2015;4:1203-14.

- [7] Zhang L, Gu FX, Chan JM, Wang AZ, Langer RS, Farokhzad OC. Nanoparticles in medicine: therapeutic applications and developments. *Clin Pharmacol Ther.* 2008;83:761-9.
- [8] Shi J, Xiao Z, Kamaly N, Farokhzad OC. Self-assembled targeted nanoparticles: evolution of technologies and bench to bedside translation. *Acc Chem Res.* 2011;44:1123-34.
- [9] Kamaly N, Xiao Z, Valencia PM, Radovic-Moreno AF, Farokhzad OC. Targeted polymeric therapeutic nanoparticles: design, development and clinical translation. *Chem Soc Rev.* 2012;41:2971-3010.
- [10] Li SD, Huang L. Stealth nanoparticles: high density but sheddable PEG is a key for tumor targeting. *J Control Release.* 2010;145:178-81.
- [11] Romberg B, Hennink WE, Storm G. Sheddable coatings for long-circulating nanoparticles. *Pharm Res.* 2008;25:55-71.
- [12] Remaut K, Lucas B, Braeckmans K, Demeester J, De Smedt SC. Pegylation of liposomes favours the endosomal degradation of the delivered phosphodiester oligonucleotides. *J Control Release.* 2007;117:256-66.
- [13] Peeters L, Sanders NN, Jones A, Demeester J, De Smedt SC. Post-pegylated lipoplexes are promising vehicles for gene delivery in RPE cells. *J Control Release.* 2007;121:208-17.
- [14] Whitehead KA, Langer R, Anderson DG. Knocking down barriers: advances in siRNA delivery. *Nat Rev Drug Discov.* 2009;8:129-38.
- [15] Yin H, Kanasty RL, Eltoukhy AA, Vegas AJ, Dorkin JR, Anderson DG. Non-viral vectors for gene-based therapy. *Nat Rev Genet.* 2014;15:541-55.
- [16] Islam MA, Reesor EK, Xu Y, Zope HR, Zetter BR, Shi J. Biomaterials for mRNA delivery. *Biomater Sci.* 2015;3:1519-33.
- [17] Zhang Y, Satterlee A, Huang L. In vivo gene delivery by nonviral vectors: overcoming hurdles? *Mol Ther.* 2012;20:1298-304.
- [18] Mura S, Nicolas J, Couvreur P. Stimuli-responsive nanocarriers for drug delivery. *Nat Mater.* 2013;12:991-1003.
- [19] Li W, Huang Z, MacKay JA, Grube S, Szoka FC, Jr. Low-pH-sensitive poly(ethylene glycol) (PEG)-stabilized plasmid nanoliposomes: effects of PEG chain length, lipid composition and assembly conditions on gene delivery. *J Gene Med.* 2005;7:67-79.
- [20] Shin J, Shum P, Thompson DH. Acid-triggered release via dePEGylation of DOPE liposomes containing acid-labile vinyl ether PEG-lipids. *J Control Release.* 2003;91:187-200.
- [21] Walker GF, Fella C, Pelisek J, Fahrmeir J, Boeckle S, Ogris M, et al. Toward synthetic viruses: endosomal pH-triggered deshielding of targeted polyplexes greatly enhances gene transfer in vitro and in vivo. *Mol Ther.* 2005;11:418-25.
- [22] Koren E, Apte A, Jani A, Torchilin VP. Multifunctional PEGylated 2C5-immunoliposomes containing pH-sensitive bonds and TAT peptide for enhanced tumor cell internalization and cytotoxicity. *J Control Release.* 2012;160:264-73.
- [23] Niu M, Naguib YW, Aldayel AM, Shi YC, Hursting SD, Hersch MA, et al. Biodistribution and in vivo activities of tumor-associated macrophage-targeting nanoparticles incorporated with doxorubicin. *Mol Pharm.* 2014;11:4425-36.
- [24] Hatakeyama H, Akita H, Kogure K, Oishi M, Nagasaki Y, Kihira Y, et al. Development of a novel systemic gene delivery system for cancer therapy with a tumor-specific cleavable PEG-lipid. *Gene Ther.* 2007;14:68-77.
- [25] Hatakeyama H, Akita H, Ito E, Hayashi Y, Oishi M, Nagasaki Y, et al. Systemic delivery of siRNA to tumors using a lipid nanoparticle containing a tumor-specific cleavable PEG-lipid. *Biomaterials.* 2011;32:4306-16.
- [26] Zhu L, Kate P, Torchilin VP. Matrix metalloproteinase 2-responsive multifunctional liposomal nanocarrier for enhanced tumor targeting. *ACS nano.* 2012;6:3491-8.
- [27] Zou Z, He X, He D, Wang K, Qing Z, Yang X, et al. Programmed packaging of mesoporous silica nanocarriers for matrix metalloproteinase 2-triggered tumor targeting and release. *Biomaterials.* 2015;58:35-45.
- [28] Takae S, Miyata K, Oba M, Ishii T, Nishiyama N, Itaka K, et al. PEG-detachable polyplex micelles based on disulfide-linked block cationomers as bioresponsive nonviral gene vectors. *J Am Chem Soc.* 2008;130:6001-9.
- [29] Wang K, Liu Y, Yi W-J, Li C, Li Y-Y, Zhuo R-X, et al. Novel shell-cross-linked micelles with detachable PEG corona for glutathione-mediated intracellular drug delivery. *Soft Matter.* 2013;9:692-9.
- [30] Cerritelli S, Velluto D, Hubbell JA. PEG-SS-PPS: reduction-sensitive disulfide block copolymer vesicles for intracellular drug delivery. *Biomacromolecules.* 2007;8:1966-72.
- [31] Gao W, Langer R, Farokhzad OC. Poly (ethylene glycol) with observable shedding. *Angew Chem Int Ed Engl.* 2010;49:6567-71.
- [32] Suma T, Miyata K, Anraku Y, Watanabe S, Christie RJ, Takemoto H, et al. Smart multilayered assembly for biocompatible siRNA delivery featuring dissolvable silica, endosome-disrupting polycation, and detachable PEG. *ACS nano.* 2012;6:6693-705.
- [33] Salzano G, Costa DF, Sarisozen C, Luther E, Mattheolabakis G, Dhargalkar PP, et al. Mixed Nanosized Polymeric Micelles as Promoter of Doxorubicin and miRNA-34a Co-Delivery Triggered by Dual Stimuli in Tumor Tissue. *Small.* 2016;10.1002/sml.201600925.
- [34] Yang X-Z, Du J-Z, Dou S, Mao C-Q, Long H-Y, Wang J. Sheddable Ternary Nanoparticles for Tumor Acidity-Targeted siRNA Delivery. *ACS Nano.* 2012;6:771-81.
- [35] Wang H-X, Yang X-Z, Sun C-Y, Mao C-Q, Zhu Y-H, Wang J. Matrix metalloproteinase 2-responsive micelle for siRNA delivery. *Biomaterials.* 2014;35:7622-34.
- [36] Gujrati M, Vaidya AM, Mack M, Snyder D, Malamas A, Lu ZR. Targeted Dual pH-Sensitive Lipid ECO/siRNA Self-Assembly Nanoparticles Facilitate In Vivo Cytosolic siRNA Delivery and Overcome Paclitaxel Resistance in Breast Cancer Therapy. *Adv Healthc Mater.* 2016;5:2882-95.
- [37] Zhu X, Xu Y, Solis LM, Tao W, Wang L, Behrens C, et al. Long-circulating siRNA nanoparticles for validating Prohibitin1-targeted non-small cell lung cancer treatment. *Proc Natl Acad Sci USA.* 2015;112:7779-84.
- [38] van der Vusse GJ. Albumin as Fatty Acid Transporter. *Drug Metabolism. Pharmacokinetics.* 2009;24:300-7.
- [39] Liu Z, Chen X. Simple bioconjugate chemistry serves great clinical advances: albumin as a versatile platform for diagnosis and precision therapy. *Chem Soc Rev.* 2016;45:1432-56.
- [40] Liu H, Moynihan KD, Zheng Y, Szeto GL, Li AV, Huang B, et al. Structure-based programming of lymph-node targeting in molecular vaccines. *Nature.* 2014;507:519-22.
- [41] Chan JM, Zhang L, Yuet KP, Liao G, Rhee J-W, Langer R, et al. PLGA-lecithin-PEG core-shell nanoparticles for controlled drug delivery. *Biomaterials.* 2009;30:1627-34.
- [42] Stylianopoulos T. EPR-effect: utilizing size-dependent nanoparticle delivery to solid tumors. *Ther Deliv.* 2013;4:421-3.
- [43] Simone E, Dziubla T, Shuvaev V, Muzykantov VR. Synthesis and characterization of polymer nanocarriers for the targeted delivery of therapeutic enzymes. *Free Radicals and Antioxidant Protocols.* 2010:145-64.
- [44] Cheng TL, Chuang KH, Chen BM, Roffler SR. Analytical measurement of PEGylated molecules. *Bioconjug Chem.* 2012;23:881-99.
- [45] Chene CJ, Saltzman WM. Enhanced siRNA delivery into cells by exploiting the synergy between targeting ligands and cell-penetrating peptides. *Biomaterials.* 2011;32:6194-203.
- [46] Koynova R, Caffrey M. Phases and phase transitions of the phosphatidylcholines. *Biochim Biophys Acta.* 1998;1376:91-145.
- [47] Alexis F, Pridgen E, Molnar LK, Farokhzad OC. Factors affecting the clearance and biodistribution of polymeric nanoparticles. *Mol Pharm.* 2008;5:505-15.
- [48] Shi J, Kantoff PW, Wooster R, Farokhzad OC. Cancer nanomedicine: progress, challenges and opportunities. *Nat Rev Cancer.* 2017;17:20-37.
- [49] Yu M, Zheng J. Clearance Pathways and Tumor Targeting of Imaging Nanoparticles. *ACS Nano.* 2015;9:6655-74.
- [50] Zeng X, Liu G, Tao W, Ma Y, Zhang X, He F, et al. A Drug-Self-Gated Mesoporous Antitumor Nanoparticle Based on pH-Sensitive Dynamic Covalent Bond. *Adv Funct Mater.* 2017; 10.1002/adfm.201605985.
- [51] Hrkach J, Von Hoff D, Mikkam Ali M, Andrianova E, Auer J, Campbell T, et al. Preclinical development and clinical translation of a PSMA-targeted docetaxel nanoparticle with a differentiated pharmacological profile. *Sci Transl Med.* 2012;4:128ra39.
- [52] Xu X, Xie K, Zhang XQ, Pridgen EM, Park GY, Cui DS, et al. Enhancing tumor cell response to chemotherapy through nanoparticle-mediated codelivery of siRNA and cisplatin prodrug. *Proc Natl Acad Sci USA.* 2013;110:18638-43.
- [53] Krishnamurthy S, Vaiyapuri R, Zhang L, Chan JM. Lipid-coated polymeric nanoparticles for cancer drug delivery. *Biomater Sci.* 2015;3:923-36.
- [54] Creixell M, Peppas NA. Co-delivery of siRNA and therapeutic agents using nanocarriers to overcome cancer resistance. *Nano Today.* 2012;7:367-79.
- [55] Love KT, Mahon KP, Levins CG, Whitehead KA, Querbes W, Dorkin JR, et al. Lipid-like materials for low-dose, in vivo gene silencing. *Proc Natl Acad Sci USA.* 2010;107:1864-9.
- [56] Tao W, Zeng X, Wu J, Zhu X, Yu X, Zhang X, et al. Polydopamine-Based Surface Modification of Novel Nanoparticle-Aptamer Bioconjugates for In Vivo Breast Cancer Targeting and Enhanced Therapeutic Effects. *Theranostics.* 2016; 6:470-84.

# Redox-Responsive Nanoparticle-Mediated Systemic RNAi for Effective Cancer Therapy

Xiaoding Xu, Jun Wu, Shuaishuai Liu, Phei Er Saw, Wei Tao, Yujing Li, Lisa Krygsman, Srinivasan Yegnasubramanian, Angelo M. De Marzo, Jinjun Shi,\* Charles J. Bieberich,\* and Omid C. Farokhzad\*

Biodegradable polymeric nanoparticles (NPs) have demonstrated significant potential to improve the systemic delivery of RNA interference (RNAi) therapeutics, such as small interfering RNA (siRNA), for cancer therapy. However, the slow and inefficient siRNA release inside tumor cells generally observed for most biodegradable polymeric NPs may result in compromised gene silencing efficacy. Herein, a biodegradable and redox-responsive NP platform, composed of a solid poly(disulfide amide) (PDSA)/cationic lipid core and a lipid–poly(ethylene glycol) (lipid–PEG) shell for systemic siRNA delivery to tumor cells, is developed. This newly generated NP platform can efficiently encapsulate siRNA under extracellular environments and can respond to the highly concentrated glutathione (GSH) in the cytoplasm to induce fast intracellular siRNA release. By screening a library of PDSA polymers with different structures and chain lengths, the optimized NP platform shows the unique features of i) long blood circulation, ii) high tumor accumulation, iii) fast GSH-triggered intracellular siRNA release, and iv) exceptionally effective gene silencing. Together with the facile polymer synthesis technique and robust NP formulation enabling scale-up, this new redox-responsive NP platform may become an effective tool for RNAi-based cancer therapy.

## 1. Introduction

Bioresponsive nanoparticles (NPs) that can respond to biological signals or pathological abnormalities, such as pH, enzyme, redox, and hypoxia,<sup>[1]</sup> have become appealing delivery platforms for the development of next-generation nanomedicines.<sup>[2]</sup> In particular, owing to the huge difference of reductive agent glutathione (GSH) concentration in the cytoplasm ( $\approx 2\text{--}10 \times 10^{-3}$  M) versus extracellular fluids ( $\approx 2\text{--}10 \times 10^{-6}$  M),<sup>[3]</sup> redox-responsive NPs have emerged as a fascinating tool for active intracellular delivery of various therapeutics, especially the bio-macromolecules that need to be delivered and released into the cytoplasm for therapeutic effects.

In the past decade, a variety of redox-responsive polymers have been successfully developed for in vivo delivery of small molecular drugs to achieve a better

Dr. X. Xu, Dr. J. Wu, Dr. P. E. Saw, Dr. W. Tao, Y. Li, L. Krygsman, Prof. J. Shi, Prof. O. C. Farokhzad  
Center for Nanomedicine and Department of Anesthesiology  
Brigham and Women's Hospital  
Harvard Medical School  
Boston, MA 02115, USA  
E-mail: jshi@bwh.harvard.edu; ofarokhzad@bwh.harvard.edu

Dr. X. Xu, Dr. P. E. Saw  
Guangdong Provincial Key Laboratory of Malignant  
Tumor Epigenetics and Gene Regulation  
Medical Research Center  
Sun Yat-Sen Memorial Hospital  
Sun Yat-Sen University  
Guangzhou 510120, China


Dr. J. Wu  
School of Biomedical Engineering  
Sun Yat-Sen University  
Guangzhou 510006, China

S. Liu, Prof. C. J. Bieberich  
Department of Biological Sciences  
University of Maryland  
Baltimore County, Baltimore, MD 21250, USA  
E-mail: bieberic@umbc.edu

Prof. S. Yegnasubramanian, Prof. A. M. De Marzo  
Sidney Kimmel Comprehensive Cancer Center  
Johns Hopkins University School of Medicine  
Baltimore, MD 21205, USA

Prof. A. M. De Marzo  
Department of Pathology  
Johns Hopkins University School of Medicine  
Baltimore, MD 21205, USA

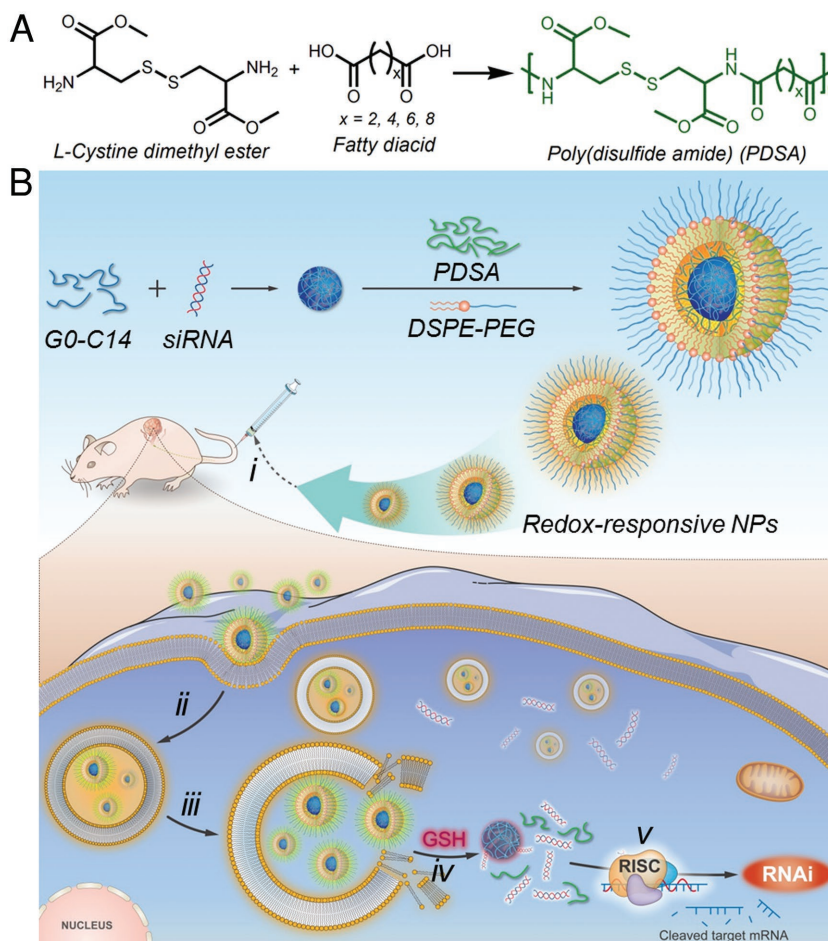
Prof. O. C. Farokhzad  
King Abdulaziz University  
Jeddah 21589, Saudi Arabia

 The ORCID identification number(s) for the author(s) of this article can be found under <https://doi.org/10.1002/sml.201802565>.

DOI: 10.1002/sml.201802565

therapeutic effect.<sup>[3d,4]</sup> One of the representative polymers is the disulfide bond-containing polymer, which can be rapidly degraded intracellularly by reductive agents such as GSH.<sup>[4c]</sup> This rapidly bioresponsive degradation behavior (from minutes to hours)<sup>[5]</sup> is distinct from the hydrolytically degradable polymers such as aliphatic polyesters and polycarbonates,<sup>[6]</sup> which usually show gradual degradation kinetics in body tissues with degradation period ranging from days to weeks even months.<sup>[4b,7]</sup> Despite the advantages of rapid degradation and fast intracellular cargo release, moderate effort has been made to construct redox-responsive NPs for systemic delivery of therapeutic nucleic acids such as small interfering RNA (siRNA), which represents a novel therapeutic modality for cancer treatment by silencing the expression of target gene(s), especially those that encode “undruggable” proteins.<sup>[8]</sup> Currently, redox-responsive polymers with the characteristic of GSH-triggered de-PEGylation<sup>[9]</sup> or de-crosslinking<sup>[4b,c,10]</sup> have been used to formulate NPs for systemic siRNA delivery, which can simultaneously achieve long blood circulation and fast intracellular siRNA release. Nevertheless, the applications of these polymers are subject to several limitations, such as complicated synthesis strategy and incomplete biodegradation issue, which may introduce difficulty in scale-up of therapeutic NP formulations.

We recently developed a facile and one-pot approach to synthesize a completely biodegradable and rapidly redox-responsive L-cysteine-based poly(disulfide amide) (PDSA) polymer.<sup>[11]</sup> The physiochemical properties of this multidisulfide bond-containing polymer (e.g., structure, molecular weight, and hydrophobicity) can be finely tuned by adjusting the structures and numbers of the repeat units in the polymeric chain. Inspired by this encouraging result, we speculate that the rapid redox response of the PDSA polymer may promote intracellular siRNA delivery and thus enhance the silencing of cancer-associated genes to achieve a better anticancer effect. To this end, we further prepare a library of PDSA polymers (Scheme 1A) in this work and systematically investigated the utility of these polymers in NPs for in vivo siRNA delivery. When mixing these polymers with cationic lipid, siRNA, and lipid-poly(ethylene glycol) (lipid-PEG), a new redox-responsive NP platform composed of a cationic lipid/siRNA complex-containing hydrophobic PDSA core and a lipid-PEG shell can be generated (Scheme 1B). With this new NP platform, we chose kinesin family member 11 (KIF11) and MYC as two proof-of-concept targets, and systematically evaluated our redox-responsive PDSA NPs for KIF11 (siKIF11) and MYC (siMYC) siRNA delivery and their anticancer efficacy. As an important member of the kinesin-like protein family, KIF11 controls mitosis, migration, and intracellular



**Scheme 1.** A) Synthesis scheme of the redox-responsive PDSA polymer. B) Schematic illustration of the redox-responsive PDSA NP platform for systemic siRNA delivery and cancer therapy. The PDSA polymer can coassemble with cationic lipid (G0-C14), siRNA, and DSPE-PEG to form stable NPs with G0-C14/siRNA complexes embedded in the hydrophobic PDSA core and DSPE-PEG covering on surface. i) After intravenous administration, the siRNA-loaded NPs can extravasate from leaky tumor vasculature and accumulate at the tumor site. After uptake by ii) tumor cells and iii) endosomal escape, the highly concentrated GSH in the cytoplasm can break the multiple disulfide bonds in the PDSA polymer and iv) induce the NP disassembly to rapidly release siRNA, thus v) resulting in efficient gene silencing to inhibit tumor growth.

transport through interaction with microtubules, and is involved in the development of malignant cancers and angiogenesis.<sup>[12]</sup> At present, KIF11 is regarded as one of the most promising new targets for antimitotic drugs and several small molecule inhibitors have entered Phase I and II clinical trials for solid tumors and hematological malignancies.<sup>[12c]</sup> MYC is a multifunctional, nuclear phosphoprotein that plays a role in cell cycle progression, apoptosis, and cellular transformation.<sup>[13]</sup> MYC overexpression is a common feature of many cancers including prostate adenocarcinoma, where increased MYC levels are detected at all stages of disease initiation and progression.<sup>[14]</sup> Moreover, it has recently been demonstrated that MYC overexpression is directly correlated with drug (e.g., cisplatin) resistance.<sup>[15]</sup> Our in vivo results show that systemic delivery of siKIF11 and siMYC with the redox-responsive PDSA NP platform can efficiently silence KIF11 and MYC expression in tumor cells and significantly inhibit prostate cancer (PCa) tumor growth.

## 2. Results and Discussion

### 2.1. Synthesis and Characterization of PDSA Polymers and RNA Interference (RNAi) NPs

Starting from the commercially available L-cystine dimethyl ester and fatty diacids with a different number of methylene groups ( $x = 2, 4, 6$ , and  $8$ ), hydrophobic PDSA polymers with different chemical structures (denoted PDSA $x$ ) were synthesized via one-step polycondensation reaction (Scheme 1A). In addition, we also chose sebacic acid ( $x = 8$ ) and changed the feed composition as well as reaction time to obtain another three PDSA polymers with different molecular weights (denoted PDSA8a, PDSA8b, and PDSA8c). Their molecular weights and chemical structures were examined by gel permeation chromatography (GPC, Figure 1A) and nuclear magnetic resonance (NMR, Figure S1, Supporting Information), respectively, to confirm successful synthesis. Due to the hydrophobic nature of these PDSA polymers, they can form hydrophobic interactions with amphiphilic cationic lipid, which have been widely used for complexing with siRNA.<sup>[8c,16]</sup> Therefore, a new RNA interference (RNAi) NP platform can be formulated through the self-assembly nanoprecipitation method by mixing the siRNA aqueous solution with the dimethylformamide (DMF) mixture of PDSA polymer, 1,2-distearoyl-*sn*-glycero-3-phosphoethanolamine-*N*-[methoxy (poly ethylene glycol)-3000] (DSPE-PEG<sub>3k</sub>), and amphiphilic cationic lipid G0-C14 (Figure S2, Supporting Information) that we had previously developed.<sup>[17]</sup> In this procedure, the cationic lipid can first complex the siRNA in the DMF solution via electrostatic interaction with the hydrophobic C14 chains positioned on the surface of the cationic lipid/siRNA complexes, which are subsequently encapsulated by the hydrophobic PDSA polymer via hydrophobic interaction to form PDSA cores when adding the DMF mixture to aqueous solution. Simultaneously, the amphiphilic DSPE-PEG<sub>3k</sub> molecules will be coated on the surface of the PDSA cores to form stable siRNA-loaded NPs. We designed and synthesized a library of PDSA polymers with different chemical structures and molecular weights to adjust the physicochemical properties of the siRNA-loaded NPs. As shown in Figure 1A, as the PDSA polymeric chain is increasing, the siRNA encapsulation efficiency (EE%) increases but the size and zeta potential ( $\zeta$ ) of the resulting NPs decrease, possibly because the increased PDSA length leads to an increased hydrophobicity that can condense the cationic

lipid/siRNA complexes to form much more compact hydrophobic core with improved siRNA loading ability and decreased zeta potential. Notably, due to the relatively low siRNA encapsulation efficiency (<20%) and large size (>200 nm) of the PDSA2 NPs, their redox response and gene silencing efficacy were not further evaluated in the subsequent experiments.

We chose PDSA8a polymer to evaluate its redox response. Figure 1B shows the molecular weight change of this polymer upon the addition of GSH. After incubating with  $10 \times 10^{-3}$  M

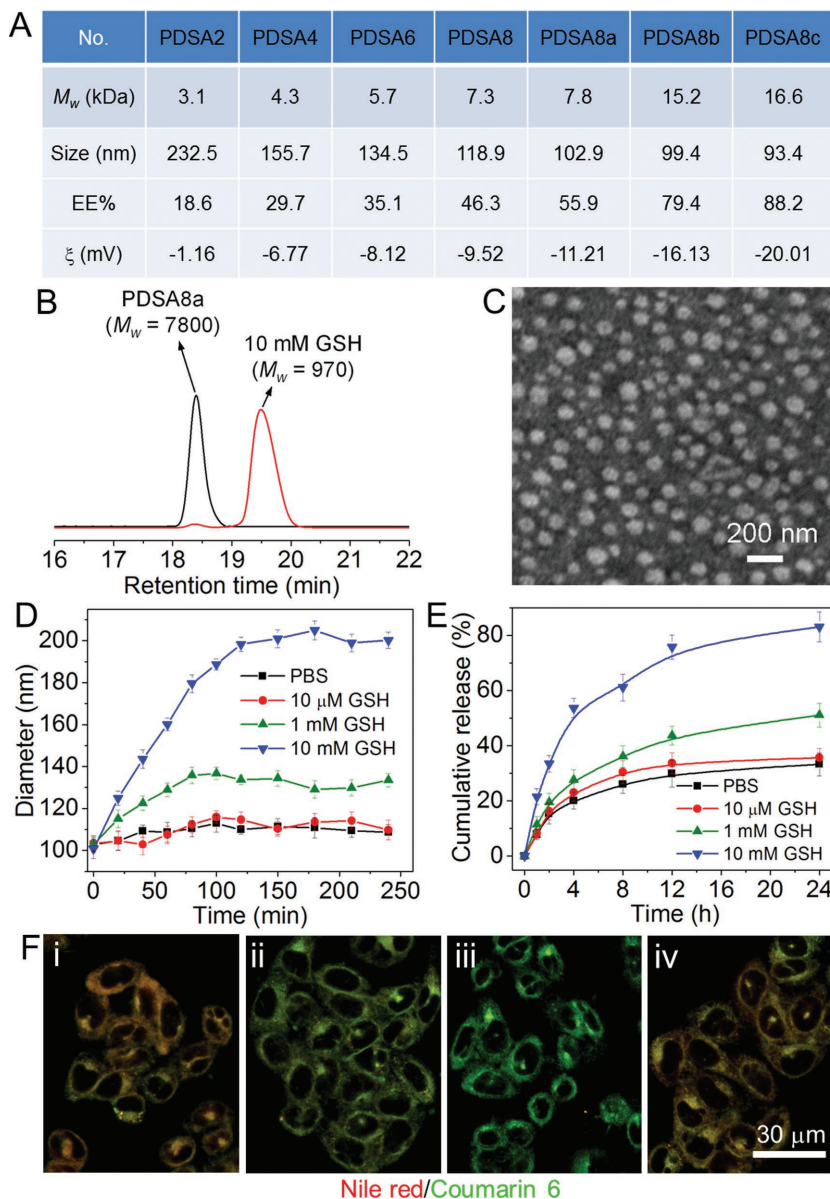


**Figure 1.** A) Molecular weight of the PDSA polymers and size, siRNA encapsulation efficiency (EE%), and zeta potential ( $\zeta$ ) of the siRNA-loaded NPs made with these PDSA polymers. B) GPC profile of the PDSA8a polymer incubated with  $10 \times 10^{-3}$  M GSH for 1 h. C) TEM image of the siLuc-loaded PDSA8a NPs. D) Size change of the siLuc-loaded PDSA8a NPs incubated with GSH at different concentrations. E) In vitro siRNA release profile of the DY547-siRNA-loaded PDSA8a NPs incubated with GSH at different concentrations. F) Fluorescent images of the Luc-HeLa cells incubated with the PDSA8a NPs loaded with coumarin 6 (green fluorescence) and Nile red (red fluorescence) for i) 1 h, ii) 2 h, and iii) 4 h, and iv) the cells first treated with  $50 \times 10^{-6}$  M NEM for 1 h followed by the PDSA8a NPs loaded with coumarin 6 and Nile red for 4 h.

GSH for 1 h, the molecular weight ( $M_w$ ) of polymer decreases from 7800 to 970 g mol<sup>-1</sup>, proving the redox-responsive characteristic of the PDSA8a polymer. With this GSH-triggered degradation, the morphology of the luciferase siRNA (siLuc)-loaded PDSA8a NPs changes from spherical shape (Figure 1C) into amorphous aggregates (Figure S3, Supporting Information) after 4 h incubation with  $10 \times 10^{-3}$  M GSH. However, the NPs maintain their spherical morphology when incubated with  $10 \times 10^{-6}$  M GSH for 24 h (Figure S3, Supporting Information). This result is consistent with the size change of the NPs upon the addition of GSH. As shown in Figure 1D, the NPs are stable, and no obvious size change can be observed when incubating the NPs with phosphate buffered saline (PBS) or GSH at a low concentration (e.g.,  $10 \times 10^{-6}$  M). In contrast, due to the degradation and aggregation triggered by the highly concentrated GSH (e.g.,  $10 \times 10^{-3}$  M), there is a significant increase in the NP size. This characteristic allows the NPs to show a redox-dependent release of DY547-labeled siLuc (DY547-siRNA). As shown in Figure 1E, more than 80% of the loaded siRNA has been released from the NPs incubated with  $10 \times 10^{-3}$  M GSH for 24 h, which is much higher than that of the NPs incubated with PBS ( $\approx 33\%$ ),  $10 \times 10^{-6}$  M GSH ( $\approx 35\%$ ), or  $1 \times 10^{-3}$  M GSH ( $\approx 51\%$ ).

We next investigated the intracellular redox response of the PDSA NPs. Förster resonance energy transfer (FRET) pairs of hydrophobic coumarin 6 ( $400_{\text{Ex}}/510_{\text{Em}}$ ) and Nile red ( $520_{\text{Ex}}/590_{\text{Em}}$ ) were encapsulated into the PDSA8a NPs and then incubated with the Luc-expressing HeLa (Luc-HeLa) cells. In this system, upon excitation of the donor dye (coumarin 6), its emitted energy can be transferred to the acceptor dye (Nile red) due to its close proximity ( $<10$  nm), and thus red fluorescence corresponding to the Nile red can be observed.<sup>[11,18]</sup> After the NP disassembly triggered by the intracellular GSH, the FRET pair can be separated, and green fluorescence corresponding to coumarin 6 can be observable under an excitation of 400 nm. Figure 1F shows the fluorescent images of the Luc-HeLa cells incubated with the PDSA8a NPs loaded with the FRET pair for different times. After 1 h of incubation, obvious NP uptake and FRET effect can be observed (Figure 1Fi). Two hours later, the red fluorescence resulting from the FRET decreases, whereas the green fluorescence corresponding to coumarin 6 increases (Figure 1Fii). After 4 h incubation, cells show a dominant green fluorescence and nearly no red fluorescence can be detected (Figure 1Fiii). However, if cells are pretreated with *N*-ethylmaleimide (NEM,  $50 \times 10^{-6}$  M) that can react with thiols and thus reduce the effective concentration of intracellular GSH,<sup>[19]</sup> the FRET effect still maintains (Figure 1Fiv) despite the fact that some internalized NPs have entered the cytoplasm (Figure S4, Supporting Information). All these data indicate that the PDSA polymers can respond to the intracellular redox environment, leading to fast degradation of the polymeric chains and disassembly of their NPs.

## 2.2. In Vitro Gene Silencing

Having confirmed the redox response of the PDSA NPs, we then evaluated their gene silencing efficacy using Luc-HeLa cells. The siLuc was used to selectively suppress Luc

expression. As shown in Figure 2A, all siRNA-loaded NPs can efficiently suppress Luc expression and  $\geq 80\%$  knockdown in Luc expression can be achieved at a  $10 \times 10^{-9}$  M siRNA dose. In particular, the NPs made with PDSA8a polymer can suppress the Luc expression by  $\approx 95\%$  without obvious cytotoxicity (Figure S5A, Supporting Information). The possible reason is that the PDSA8a NPs show moderate zeta potential (e.g., higher than PDSA8b and 8c NPs) and siRNA loading ability (e.g., stronger than PDSA4, 6, and 8 NPs). Therefore, PDSA8a NPs were selected for the following experiments. To verify the contribution of the redox response to efficient gene silencing of PDSA NPs, we used commercially available poly(lactic-co-glycolic acid) (PLGA) with a similar molecular weight (viscosity,  $0.1\text{--}0.25$  dL g<sup>-1</sup>) as that of the PDSA8a polymer to prepare non-responsive PLGA NPs, then examined their gene silencing efficacy. Without redox response, the PLGA NPs show much lower gene silencing efficacy compared to the PDSA8a NPs, and more than 40% Luc can still be expressed in the treated cells (Figure 2A), which is similar to the Luc expression in the cells first treated by  $50 \times 10^{-6}$  M NEM for 1 h followed by transfection with siLuc-loaded PDSA8a NPs. This result strongly demonstrates the importance of redox response to the efficient gene silencing rendered by the PDSA NPs.

After screening the NP platform with optimal silencing efficacy (PDSA8a NPs) and low cytotoxicity (Figure S5B, Supporting Information), we then examined whether this RNAi NP platform can be used to silence KIF11 in PCa cells. KIF11 is a motor protein that belongs to the kinesin-like protein family and is involved in the development of malignant cancers including PCa.<sup>[12]</sup> As an attractive anticancer target, inhibition of KIF11 by small molecules has demonstrated the ability to induce mitotic arrest and apoptosis of multiple cancers.<sup>[12c]</sup> The prostate cancer (PC3) cells were used as a model cell line to examine the KIF11 silencing efficacy of the PDSA8a NPs. Figure 2B shows the western blot analysis of KIF11 expression in the PC3 cells. The siKIF11-loaded NPs can dramatically suppress the KIF11 expression and nearly no KIF11 can be detected at a very low siRNA dose (e.g.,  $5 \times 10^{-9}$  M). The immunofluorescence staining analysis (Figure 2C) further demonstrates efficient KIF11 silencing by the PDSA8a NPs. After the treatment with siKIF11-loaded NPs at a  $5 \times 10^{-9}$  M siRNA dose, red fluorescence corresponding to the KIF11 is absent (Figure 2Cii), indicating almost 100% knockdown of the KIF11 expression. To further extend the application of the PDSA8a NPs for gene silencing and cancer treatment, we also evaluated their ability to downregulate the expression of MYC, a cancer-associated protein overexpressed in the earliest phase of PCa and metastatic PCa.<sup>[14]</sup> As shown in Figure 2D, the siMYC-loaded NPs can efficiently suppress MYC expression ( $\approx 60\%$  knockdown) at a  $15 \times 10^{-9}$  M siRNA dose. At a  $25 \times 10^{-9}$  M siRNA dose, MYC expression is nearly extinguished ( $<2\%$ ; Figure S6, Supporting Information). Similar results can also be found in the immunofluorescence staining analysis (Figure 2Eii). With this suppressed KIF11 or MYC expression, the proliferation rate of PC3 cells is significantly inhibited (Figure 2F,G). Particularly, only 25% of the cells treated with the siKIF11-loaded NPs for 24 h at a  $10 \times 10^{-9}$  M siRNA dose are alive after 8 days (Figure 2F), while there is about tenfold increase in the number of cells treated with the siLuc-loaded PDSA8a NPs (Control). Notably,

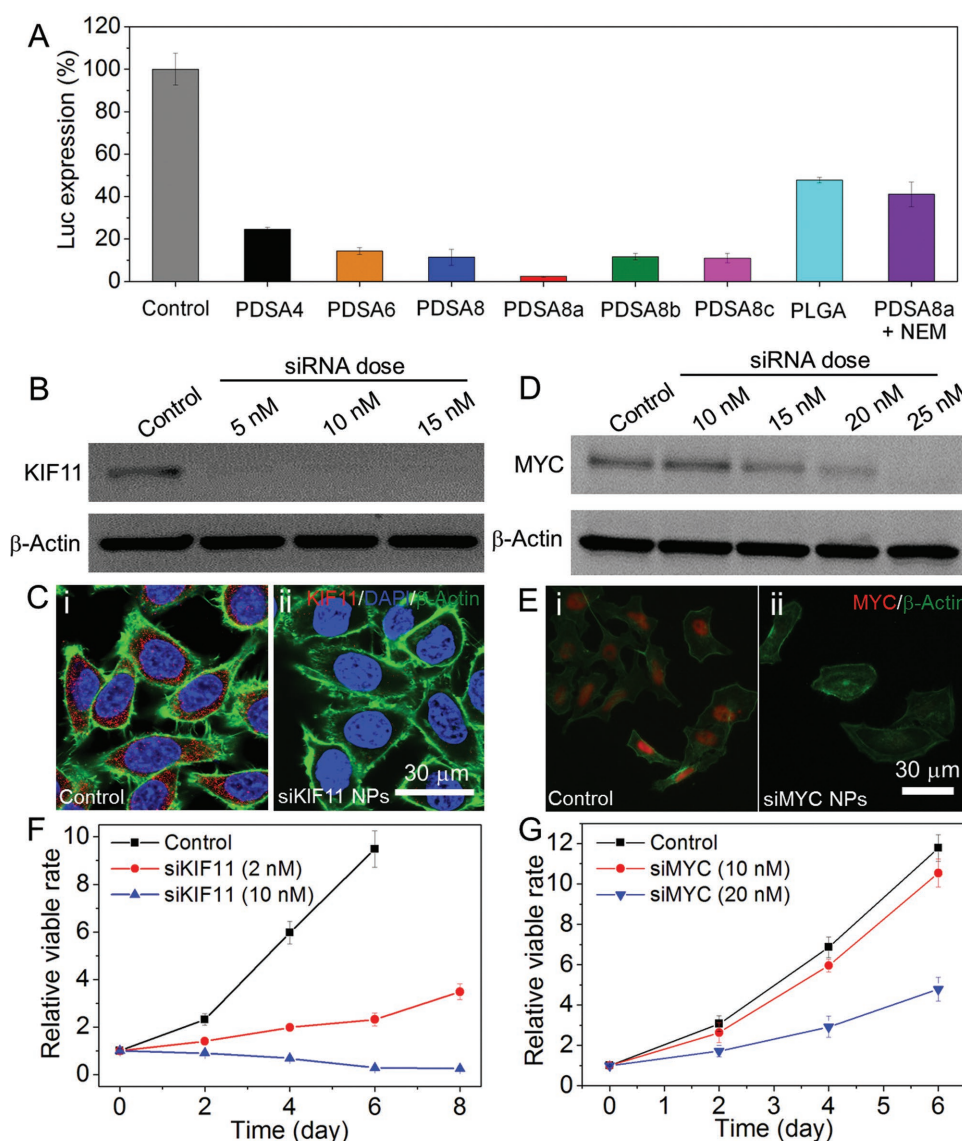


**Figure 2.** A) Luc expression in the Luc-HeLa cells treated with the siLuc-loaded PDSA NPs, PLGA NPs, and  $50 \times 10^{-6}$  M NEM for 1 h followed by the siLuc-loaded PDSA NPs at a  $10 \times 10^{-9}$  M siRNA dose. B) Western blot analysis of KIF11 expression in PC3 cells treated with the siKIF11-loaded PDSA8a NPs. C) Immunofluorescence staining analysis of KIF11 expression in PC3 cells treated with i) control NPs and ii) siKIF11-loaded PDSA8a NPs at a  $5 \times 10^{-9}$  M siRNA dose. D) Western blot analysis of MYC expression in PC3 cells treated with the siMYC-loaded PDSA8a NPs. E) Immunofluorescence staining analysis of MYC expression in PC3 cells treated with i) control NPs and ii) siMYC-loaded PDSA8a NPs at a  $25 \times 10^{-9}$  M siRNA dose. F,G) Proliferation profiles of PC3 cells treated with F) siKIF11- or G) siMYC-loaded PDSA8a NPs. siLuc-loaded PDSA8a NPs were used as the control in these experiments.

because the very low expression of KIF11 and MYC in the normal human prostate epithelial cells (HPrEc), the silencing of KIF11 or MYC does not affect the fate of HPrEc cells significantly (Figure S7, Supporting Information).

### 2.3. Pharmacokinetics and Biodistribution

After validating the efficient gene silencing of the PDSA8a NPs in vitro, we next assessed their pharmacokinetics (PK) and biodistribution (BioD). PK was examined by intravenous injection of DY677-siRNA-loaded NPs to normal adult

Balb/c mice (1 nmol siRNA dose per mouse,  $n = 3$ ). As shown in **Figure 3A**, the NPs show long blood circulation with a half-life ( $t_{1/2}$ ) of  $\approx 4.92$  h. In contrast, the naked siRNA is rapidly cleared from the blood and its blood  $t_{1/2}$  is less than 10 min. This prolonged blood circulation is mainly due to the protection of PEG outer layer.<sup>[20]</sup> The BioD was evaluated by intravenously injecting DY677-siRNA-loaded NPs into athymic nude mice bearing PC3 xenograft tumors. **Figure 3B** shows the fluorescent image of the mice at 24 h post injection. Given the long blood circulation characteristic of the PDSA8a NPs, they show a much higher tumor accumulation than the naked siRNA (**Figure 3C**). The tumors and major organs were

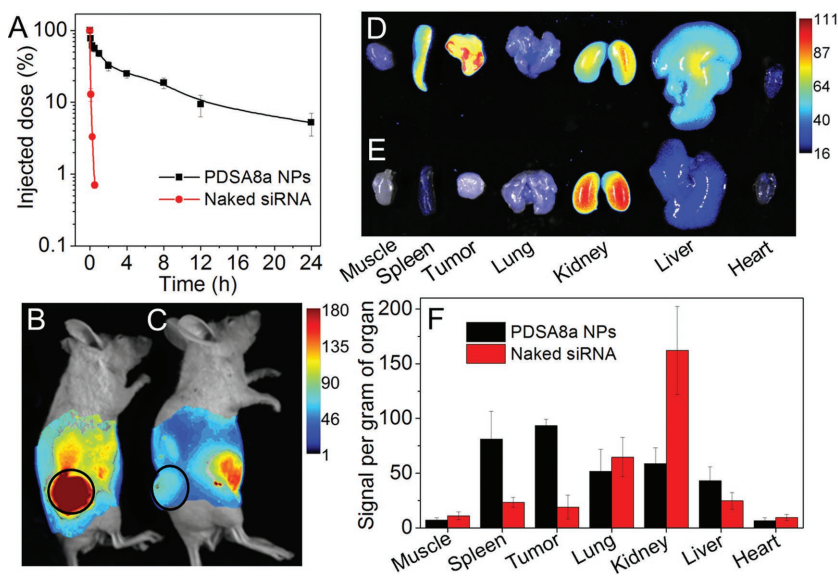


**Figure 3.** A) Pharmacokinetics of naked DY677-siRNA and DY677-siRNA-loaded PDSA8a NPs. B,C) Overlaid fluorescent image of the PC3 xenograft tumor-bearing nude mice at 24 h post injection of B) DY677-siRNA-loaded PDSA8a NPs and C) naked DY677-siRNA. Tumors are indicated by ellipses. D,E) Overlaid fluorescent image of the tumors and main organs of the PC3 xenograft tumor-bearing nude mice sacrificed at 24 h post injection of the D) DY677-siRNA-loaded PDSA8a NPs and E) naked DY677-siRNA. F) Biodistribution of the NPs quantified from panels (D) and (E).

harvested at 24 h post injection (Figure 3D,E), and the quantification of BioD is shown in Figure 3F. The siRNA-loaded NPs show about sixfold higher accumulation in tumors than the naked siRNA.

## 2.4. In Vivo Gene Silencing and Antitumor Efficacy

With the promising in vitro and PK/BioD results described above, we further evaluated whether our redox-responsive siRNA delivery platform can silence KIF11 and MYC expressions in vivo and show anticancer effects. To this end, the siRNA-loaded PDSA8a NPs were intravenously injected into the PC3 xenograft tumor-bearing athymic nude mice (1 nmol siRNA dose per mouse,  $n = 3$ ) for three consecutive days. As shown in Figure 4A–C, the siKIF11- or siMYC-loaded NPs lead to  $\approx 85\%$  knockdown in KIF11 protein expression (Figure 4A) or  $\approx 55\%$  knockdown in MYC protein expression (Figure 4B) compared to the control NPs. A similar decrease of KIF11 and MYC expressions was also observed by immunohistochemical (IHC) analysis (Figure S8, Supporting Information). To confirm whether the NP-mediated KIF11 and MYC silencing has an anticancer effect, the siRNA-loaded NPs were intravenously injected into the PC3 xenograft tumor-bearing mice once every 2 days at a 1 nmol siRNA dose per mouse ( $n = 5$ ). After four consecu-

tive injections of the siKIF11-loaded NPs, the tumor growth was significantly inhibited compared to the mice treated with PBS, naked siKIF11, or control NPs loaded with siLuc (Figure 4D,E). Within a long evaluation period of 40 days, there is less than

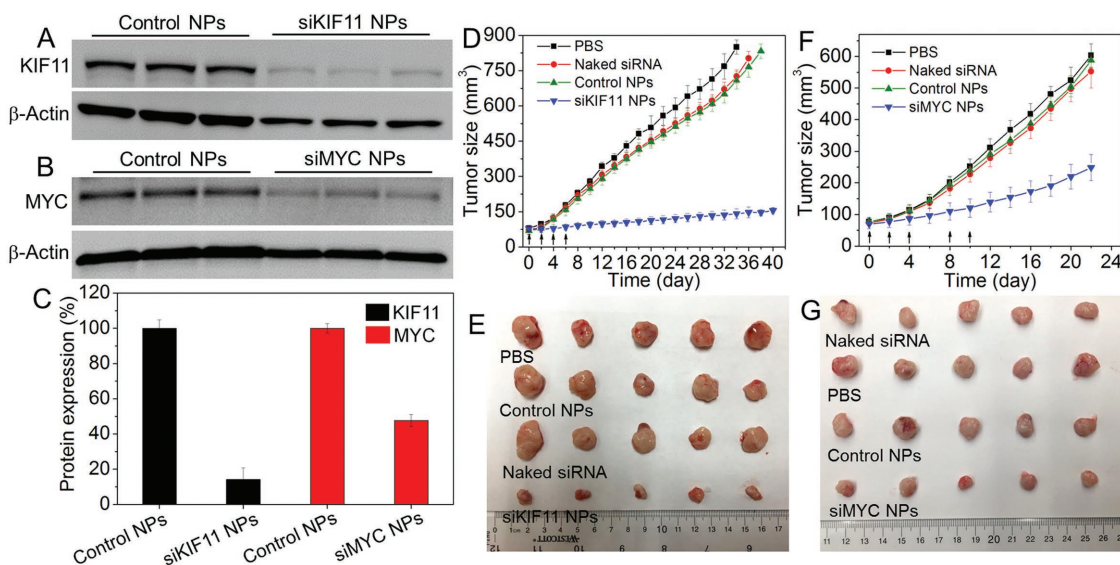


**Figure 4.** A–C) Western blot analysis of A) KIF11 and B) MYC expression in the PC3 xenograft tumor tissue after systemic treatment by control NPs and siKIF11- or siMYC-loaded PDSA8a NPs. D) Tumor size of the PC3 xenograft tumor-bearing nude mice ( $n = 5$ ) after systemic treatment by PBS, naked siKIF11, control NPs, and siKIF11-loaded PDSA8a NPs. The intravenous injections are indicated by the arrows. E) Photograph of the harvested PC3 xenograft tumors after 40 days of evaluation of the mice in panel (D). F) Tumor size of the PC3 xenograft tumor-bearing nude mice ( $n = 5$ ) after systemic treatment by PBS, naked siMYC, control NPs, and siMYC-loaded PDSA8a NPs. The intravenous injections are indicated by the arrows. G) Photograph of the harvested PC3 xenograft tumors after 22 day evaluation of the mice in panel (F). siLuc-loaded PDSA8a NPs were used as control NPs.

twofold increase (from  $\approx 78$  to  $\approx 155$  mm<sup>3</sup>) in tumor size of the mice treated with the siKIF11-loaded NPs (Figure 4D). However, the tumor size in the three control groups is  $\approx 6$ -fold larger than that of the mice treated with siKIF11-loaded NPs. The NP-mediated MYC silencing also shows an impressive anticancer effect. As shown in Figure 4F,G, after five intravenous injections of the siMYC-loaded NPs into PC3 xenograft tumor-bearing mice, the tumor growth rate is efficiently inhibited. A 3.5-fold increase in tumor size (from  $\approx 70$  to 278 mm<sup>3</sup>) was observed at day 22 in mice that received siMYC-loaded NPs, which is a much smaller increase than that seen in mice treated with PBS naked siMYC or siLuc-loaded NPs ( $\approx 8$ -fold increase in tumor size). It is important to note that the siKIF11-loaded NPs show neglectable in vivo side effects, and there is no obvious influence on mouse body weight (Figure S9, Supporting Information). To further evaluate the potential in vivo side effects, the PDSA8a NPs loaded with siKIF11 or siMYC were intravenously injected to normal adult mice (1 nmol siRNA dose per mouse,  $n = 3$ ). Blood serum analysis showed that tumor necrosis alpha (TNF- $\alpha$ ), interferon gamma (IFN- $\gamma$ ), interleukin-6 (IL-6), and interleukin-12 (IL-12) levels were in the normal range at 24 h post injection of the siKIF11- or siMYC-loaded NPs (Figure S10, Supporting Information). After three daily injections, no noticeable histological changes were noticed in the tissues from heart, liver, spleen, lung, or kidney (Figure S11, Supporting Information). All of these results indicate the good biocompatibility of this redox-responsive NP platform.

### 3. Conclusion

In summary, we have designed and developed a new-generation redox-responsive NP platform for systemic siRNA delivery and effective cancer therapy. This new NP platform is comprised of a cationic lipid/siRNA complex-containing hydrophobic PDSA core and a lipid-PEG shell. The physiochemical properties of this nanoplateform can be finely tuned by adjusting the two biocompatible repeat units in the PDSA polymeric chain. In vitro results show that the PDSA NP platform can respond to the cytosolic GSH to achieve fast intracellular siRNA release, leading to efficient silencing of two target proteins (KIF11 and MYC) in PCa cells. In vivo results show that this NP platform with long blood circulation has a high tumor accumulation, can efficiently suppress the KIF11 and MYC expression in tumor tissue, and can significantly inhibit PCa tumor growth with negligible toxicities. Combined with the facile polymer synthesis technique and robust NP formulation enabling scale-up, we expect this long-circulating, biodegradable and fast redox-responsive RNAi NP platform to be of high interest for the treatment of a wide range of solid tumors.

### 4. Experimental Section

**Preparation of the PDSA NPs:** The PDSA polymer was dissolved in DMF to form a homogeneous solution with a concentration of 20 mg mL<sup>-1</sup>. To prepare the siRNA-loaded NPs, a mixture of 1 nmol siRNA (0.1 nmol  $\mu$ L<sup>-1</sup> aqueous solution) and 50  $\mu$ L of G0-C14 (5 mg mL<sup>-1</sup> in DMF) in a N/P molar ratio of 1:20 was prepared and added to the mixture of 200  $\mu$ L of PDSA polymer solution and 140  $\mu$ L

of DSPE-PEG<sub>3k</sub> solution (20 mg mL<sup>-1</sup> in DMF). Under vigorously stirring (1000 rpm), the mixture was added dropwise to 5 mL of deionized water. The formed NP dispersion was transferred to an ultrafiltration device (EMD Millipore, MWCO 100 K), and centrifuged to remove the organic solvent and free compounds. After washing with deionized water (3  $\times$  5 mL), the siRNA-loaded NPs were dispersed in 1 mL of pH 7.4 PBS buffer. To prepare the NPs loaded with FRET pair of coumarin 6 and Nile red, a mixture of 2.5  $\mu$ L of coumarin 6 ( $20 \times 10^{-3}$  M in DMF) and 12  $\mu$ L of Nile red ( $50 \times 10^{-3}$  M in DMF) in a molar ratio of 1:12 was added to the mixture of 200  $\mu$ L of PDSA polymer and 140  $\mu$ L of DSPE-PEG<sub>3k</sub> solution (20 mg mL<sup>-1</sup> in DMF). Under vigorously stirring (1000 rpm), the mixture was added dropwise to 5 mL of deionized water. The formed NPs were washed according to the method described above and finally dispersed in 1 mL of pH 7.4 PBS buffer.

**Characterizations of the PDSA NPs:** Size and zeta potential of the NPs were determined by dynamic light scattering (DLS, Brookhaven Instruments Corporation). The morphology of NPs was visualized on a Tecnai G<sup>2</sup> Spirit BioTWIN transmission electron microscope (TEM). Before observation, the sample was stained with 1% uranyl acetate and dried under air. To determine siRNA encapsulation efficiency (EE%), DY547-labeled siLuc (DY547-siRNA) loaded NPs were prepared according to the method aforementioned. A small volume (5  $\mu$ L) of the NP solution was withdrawn and mixed with 20-fold dimethyl sulfoxide (DMSO). The fluorescence intensity of DY547-siRNA was measured using a Synergy HT multi-mode microplate reader. The amount of loaded siRNA in the NPs was calculated according to the standard curve.

**Evaluation of the Reduction Response of the PDSA NPs:** The siLuc-loaded PDSA NPs were prepared according to the method described above and then dispersed in 1 mL of pH 7.4 PBS buffer containing GSH at different concentrations. At a predetermined interval, the size of the NPs was examined by DLS, and the morphology of the NPs was observed by TEM. To examine the influence of reduction response on the siRNA release, DY547-labeled siLuc-loaded NPs were prepared according to the method as described above. Subsequently, the NPs were dispersed in 1 mL of pH 7.4 PBS buffer and then transferred to a Float-a-lyzer G2 dialysis device (MWCO = 100 kDa, Spectrum) that was immersed in PBS buffer containing GSH at 37 °C. At a predetermined interval, 5  $\mu$ L of the NP solution was withdrawn and mixed with 20-fold DMSO. The fluorescence intensity of DY547-labeled siRNA was determined using a microplate reader.

**Cell Culture:** Luc-HeLa and PC3 cells were incubated in Roswell Park Memorial Institute (RPMI) 1640 medium with 10% fetal bovine serum (FBS) at 37 °C in a humidified atmosphere containing 5% CO<sub>2</sub>.

**Confocal Laser Scanning Microscope (CLSM):** Luc-HeLa (50 000 cells) were seeded in disks and incubated in 2 mL of RPMI 1640 medium containing 10% FBS for 24 h. After replacing the medium with 2 mL of fresh medium, DY547-labeled siLuc-loaded NPs were added, and the cells were allowed to incubate for different times. After removing the medium and subsequently washing with PBS buffer thrice, lysotracker green and Hoechst 33342 were added to stain the endosomes and nuclei, respectively. The cells were finally viewed under a FV1000 CLSM (Olympus).

**Evaluation of Intracellular Reduction Response of the PDSA NPs:** Luc-HeLa (50 000 cells) were seeded in disks and incubated in 2 mL of RPMI 1640 medium containing 10% FBS for 24 h. After replacing the medium with 2 mL of fresh medium, NPs loaded with FRET pair of coumarin 6 and Nile red were added, and the cells were allowed to incubate for different times. After removing the medium and subsequently washing with PBS buffer thrice, the cells were fixed with 4% paraformaldehyde and finally viewed under CLSM.

**Luc Silencing:** Luc-HeLa cells were seeded in 96-well plates (5000 cells per well) and incubated in 0.1 mL of RPMI 1640 medium with 10% FBS for 24 h. Thereafter, the medium was replaced by fresh medium, and siLuc-loaded NPs were added. After 24 h incubation, the cells were washed with PBS buffer and allowed to incubate in fresh medium for another 48 h. The Luc expression was determined using Steady-Glo luciferase assay kits. Cytotoxicity was measured using AlamarBlue

assay according to the manufacturer's protocol. The luminescence or fluorescence intensity was measured using a microplate reader, and the average value of five independent experiments was collected.

**In Vitro KIF11 and MYC Silencing:** PC3 cells were seeded in 6-well plates (50 000 cells per well) and incubated in 2 mL of RPMI 1640 medium containing 10% FBS for 24 h. Subsequently, the medium was replaced by fresh medium, and then siKIF11- or siMYC-loaded NPs were added. After incubation for 24 h, the cells were washed with pH 7.4 PBS buffer and further incubated in fresh medium for another 48 h. For the cells treated with siKIF11-loaded NPs, they were digested by trypsin and the proteins were extracted using modified radioimmunoprecipitation assay lysis buffer ( $50 \times 10^{-3}$  M Tris-HCl pH 7.4,  $150 \times 10^{-3}$  M NaCl, 1% NP-40 substitute, 0.25% sodium deoxycholate,  $1 \times 10^{-3}$  M sodium fluoride,  $1 \times 10^{-3}$  M  $\text{Na}_3\text{VO}_4$ ,  $1 \times 10^{-3}$  M ethylenediaminetetraacetic acid (EDTA)), supplemented with protease inhibitor cocktail and  $1 \times 10^{-3}$  M phenylmethanesulfonyl fluoride (PMSF). For the cells treated with siMYC-loaded NPs, the cells were incubated with the medium containing  $10 \times 10^{-6}$  M lactacystin and  $10 \mu\text{g mL}^{-1}$  calpain inhibitor I to prevent MYC degradation for 1 h and then digested by trypsin. Subsequently, the proteins were extracted according to the protocol described above. The expressions of KIF11 and MYC were examined using western blot described below.

**Western Blot:** Equal amount of protein, as determined with a bicinchoninic acid (BCA) protein assay kit (Pierce/Thermo Scientific) according to the manufacturer's instruction, was added to sodium dodecyl sulfate polyacrylamide gel electrophoresis (SDS-PAGE) gels and separated by gel electrophoresis. After transferring the protein from gel to polyvinylidene difluoride membrane, the blot was blocked with 3% bovine serum albumin (BSA) in tris buffered saline with Tween 20 (TBST) ( $50 \times 10^{-3}$  M Tris-HCl pH 7.4,  $150 \times 10^{-3}$  M NaCl, and 0.1% Tween 20), and then incubated with a mixture of primary rabbit antibody (polyclonal anti-KIF11 (Abcam, ab61199), monoclonal anti-MYC (Abcam, ab32072), and monoclonal anti-cMYC (Cell Signaling, D84C12), and polyclonal anti- $\beta$ -actin (Cell Signaling, 13E5)). The expression of KIF11 and MYC was detected with horseradish peroxidase (HRP)-conjugated secondary antibody (anti-rabbit immunoglobulin G (IgG) HRP-linked antibody, Cell Signaling) and an enhanced chemiluminescence (ECL) detection system (Pierce).

**Immunofluorescence Staining:** PC3 cells (50 000 cells) were seeded in disks and incubated in 2 mL of RPMI 1640 medium containing 10% FBS for 24 h. After replacing the medium with fresh medium, siKIF11- or siMYC-loaded NPs were added, and the cells were allowed to incubate with the siRNA-loaded NPs for 24 h. Subsequently, the cells were washed with pH 7.4 PBS buffer thrice and then incubated with fresh medium for another 48 h. Thereafter, the cells were fixed with 4% paraformaldehyde, and then permeabilized by incubation in 0.2% Triton X-100 in pH 7.4 PBS buffer for 5 min, followed by washing with pH 7.4 PBS buffer ( $3 \times 5$  min). Subsequently, the cells were blocked with blocking buffer (2% normal goat serum, 2% BSA, and 0.2% gelatin in pH 7.4 PBS buffer) at room temperature for 1 h. After washing the cells with pH 7.4 PBS buffer ( $3 \times 5$  min), KIF11 or MYC rabbit antibody diluted in 1% BSA solution was added and the cells were incubated for 1 h. Subsequently, the cells were with pH 7.4 PBS buffer ( $3 \times 5$  min), and then further incubated with Alex Fluor 647-linked secondary antibody (Life Technologies, A-11011) and Alex Fluor 488-conjugated phalloidin (Life Technologies, A12379) for another 1 h. After washing with pH 7.4 PBS buffer ( $3 \times 5$  min), the cells were viewed under a FV1000 CLSM.

**In Vitro Cell Proliferation:** PC3 cells were seeded in 6-well plates (20 000 cells per well) and incubated in 2 mL of RPMI 1640 medium containing 10% FBS for 24 h. After replacing the medium with fresh medium, siKIF11- or siMYC-loaded NPs were added and the cells were allowed to incubate with the siRNA-loaded NPs for 24 h. Thereafter, the cells were washed with pH 7.4 PBS buffer thrice and fresh medium was added for further incubation. At predetermined intervals, the cytotoxicity was measured by AlamarBlue assay according to the manufacturer's protocol. After each measurement, the AlamarBlue agent was removed and 2 mL of fresh medium was added for further incubation.

**Animals:** Healthy male BALB/c mice and athymic nude mice (4–5 weeks old) were purchased from Charles River Laboratories. All in vivo studies were performed in accordance with National Institutes of Health animal care guidelines and in strict pathogen-free conditions in the animal facility of Brigham and Women's Hospital and University of Maryland. Animal protocol was approved by the Institutional Animal Care and Use Committees on animal care (Harvard Medical School and the University of Maryland Baltimore County).

**Pharmacokinetics Study:** Healthy male BALB/c mice were randomly divided into two groups ( $n = 3$ ) and given an intravenous injection of either i) DY677-labeled siLuc-loaded NPs or ii) DY677-labeled naked siLuc at a 1 nmol siRNA dose per mouse. At a predetermined time interval, orbital vein blood (20  $\mu\text{L}$ ) was withdrawn using a tube containing heparin, and the wound was pressed for several seconds to stop the bleeding. The fluorescence intensity of DY677-labeled siRNA in the blood was determined by a microplate reader.

**PC3 Xenograft Tumor Model:** The PC3 xenograft tumor model was constructed by subcutaneous injection with 200  $\mu\text{L}$  of PC3 cell suspension (a mixture of RPMI 1640 medium and Matrigel in 1:1 volume ratio) with a density  $2 \times 10^6$  cells  $\text{mL}^{-1}$  into the back region of healthy male athymic nude mice. When the tumor volume reached 50–70  $\text{mm}^3$ , the mice were used for the following in vivo experiments.

**Biodistribution:** PC3 xenograft tumor-bearing mice were randomly divided into two groups ( $n = 3$ ) and given an intravenous injection of either i) DY677-labeled naked siLuc or ii) DY677-labeled siLuc-loaded NPs at a 1 nmol siRNA dose per mouse. Twenty-four hours after the injection, the mice were imaged using the Maestro 2 In-Vivo Imaging System (Cri Inc). Main organs and tumors were then harvested and imaged. To quantify the accumulation of siRNA-loaded NPs in the tumors and main organs, the fluorescence intensity of each tissue was quantified by Image-J.

**In Vivo KIF11 Silencing:** PC3 xenograft tumor-bearing mice were randomly divided into two groups ( $n = 3$ ) and intravenously injected with i) siLuc-loaded NPs or ii) siKIF11-loaded NPs for three consecutive days. Twenty-four hours after the final injection, mice were sacrificed and tumors were harvested for western blot analysis and immunohistochemistry staining. For the western blot analysis, the proteins in the tumor were extracted using modified radioimmunoprecipitation assay lysis buffer ( $50 \times 10^{-3}$  M Tris-HCl pH 7.4,  $150 \times 10^{-3}$  M NaCl, 1% NP-40 substitute, 0.25% sodium deoxycholate,  $1 \times 10^{-3}$  M sodium fluoride,  $1 \times 10^{-3}$  M  $\text{Na}_3\text{VO}_4$ ,  $1 \times 10^{-3}$  M EDTA), supplemented with protease inhibitor cocktail and  $1 \times 10^{-3}$  M PMSF. Western blot was performed according to the method described above.

**IHC Staining:** IHC staining was performed on formalin-fixed paraffin-embedded tumor sections. Briefly, tumor slides were first heated to 60 °C for 1 h, desparaffinized with xylene ( $3 \times 5$  min), and washed with different concentrations of alcohol. After retrieval of antigen using DAKO target retrieval solution at 95–99 °C for 40 min, followed by washing, the slides were blocked with peroxidase blocking buffer (DAKO Company) for 5 min. After washing buffer (DAKO Company), the slides were incubated with KIF11 rabbit antibody diluted in DAKO antibody solution for 1 h. The slides were then washed and incubated with peroxidase-labeled polymer for 30 min. After washing and staining with DAB+ substrate–chromogen solution and hematoxylin, the slides that remounted and viewed under a MVX10 MacroView Dissecting scope equipped with an Olympus DP80 camera.

**In Vivo MYC Silencing:** PC3 xenograft tumor-bearing mice were randomly divided into two groups ( $n = 3$ ) and intravenously injected with i) siLuc-loaded NPs or ii) siMYC-loaded NPs for three consecutive days. Twenty-four hours after the final injection, 40  $\mu\text{L}$  of PBS containing  $10 \times 10^{-6}$  M lactacystin and  $10 \mu\text{g mL}^{-1}$  calpain inhibitor I was administered by intratumoral injection to prevent MYC degradation. One hour later, the mice were sacrificed and tumors were harvested for western blot analysis and immunohistochemistry staining according to the method described above.

**Immune Response:** Healthy male BALB/c mice were randomly divided into five groups ( $n = 3$ ) and given an intravenous injection

of either i) PBS, ii) naked siKIF11, iii) naked siMYC, iv) siKIF11- or v) siMYC-loaded NPs at a 1 nmol siRNA dose per mouse. Twenty-four hours after injection, blood was collected and serum was isolated for measurements of representative cytokines (TNF- $\alpha$ , IL-6, IL-12, and IFN- $\gamma$ ) by enzyme-linked immunosorbent assay (ELISA, PBL Biomedical Laboratories and BD Biosciences) according to the manufacturer's instruction.

**Histology:** Healthy male BALB/c mice were randomly divided into five groups ( $n = 3$ ) and administered daily intravenous injections of either i) PBS, ii) naked siKIF11, iii) naked siMYC, iv) siKIF11-, or v) siMYC-loaded NPs at a 1 nmol siRNA dose per mouse. After three consecutive injections, the main organs were collected 24 h post the final injection, fixed with 4% paraformaldehyde, and embedded in paraffin. Tissue sections were stained with hematoxylin–eosin (H&E) and then viewed under an optical microscope.

**Inhibition of Tumor Growth:** PC3 xenograft tumor-bearing mice were randomly divided into four groups ( $n = 5$ ) and intravenously injected with i) PBS, ii) naked siKIF11 or siMYC, iii) siLuc-loaded NPs, or iv) siKIF11 or siMYC-loaded NPs at a 1 nmol siRNA dose per mouse once every 2 days. The tumor growth was monitored every 2 days by measuring perpendicular diameters using a caliper, and tumor volume was calculated as follows

$$V = W^2 \times L/2 \quad (1)$$

where  $W$  and  $L$  are the shortest and longest diameters, respectively.

**Statistical Analysis:** Statistical significance was determined by a two-tailed Student's *t*-test assuming equal variance. A *p*-value of <0.05 is considered statistically significant.

## Supporting Information

Supporting Information is available from the Wiley Online Library or from the author.

## Acknowledgements

X.X., J.W., and S.L. contributed equally to this work. This work was supported in part by the Department of Defense Prostate Cancer Research Program Synergistic Idea Development Award (W81XWH-15-1-0728); the National Institutes of Health grants (HL127464, CA200900); the David H. Koch-Prostate Cancer Foundation (PCF) Program in Cancer Nanotherapeutics and the Movember-PCF Challenge Award; the Thousand Talents Program for Distinguished Young Scholars; and the Science and Technology Planning Project of Guangdong Province (2016A010103015) and Shenzhen City (JCYJ20170307141438157). O.C.F. has financial interest in Selecta Biosciences, Tarveda Therapeutics, and Placon Therapeutics.

## Conflict of Interest

The authors declare no conflict of interest.

## Keywords

biodegradable nanoparticle, cancer therapy, redox-responsive, siRNA delivery

Received: July 2, 2018


Revised: August 21, 2018

Published online: September 17, 2018

- [1] a) S. Wang, P. Huang, X. Chen, *Adv. Mater.* **2016**, *28*, 7340; b) S. Wang, P. Huang, X. Chen, *ACS Nano* **2016**, *10*, 2991; c) Y. Lee, S. Lee, D. Y. Lee, B. Yu, W. Miao, S. Jon, *Angew. Chem., Int. Ed.* **2016**, *55*, 10676; d) E. J. Kwon, J. H. Lo, S. N. Bhatia, *Proc. Natl. Acad. Sci. USA* **2015**, *112*, 14460; e) L. Zhu, T. Wang, F. Perche, A. Taigind, V. P. Torchilin, *Proc. Natl. Acad. Sci. USA* **2013**, *110*, 17047; f) X. Xu, P. E. Saw, W. Tao, Y. Li, X. Ji, S. Bhasin, Y. Liu, D. Ayyash, J. Rasmussen, M. Huo, J. Shi, O. C. Farokhzad, *Adv. Mater.* **2017**, *29*, 1700141.
- [2] a) J. Shi, P. W. Kantoff, R. Wooster, O. C. Farokhzad, *Nat. Rev. Cancer* **2017**, *17*, 20; b) Y. Lu, A. A. Aimetti, R. Langer, Z. Gu, *Nat. Rev. Mater.* **2017**, *2*, 16075.
- [3] a) P. Castellani, E. Balza, A. Rubartelli, *Antioxid. Redox Signaling* **2014**, *20*, 1086; b) F. Q. Schafer, G. R. Buettner, *Free Radicals Biol. Med.* **2001**, *30*, 1191; c) G. Wu, Y. Z. Fang, S. Yang, J. R. Lupton, N. D. Turner, *J. Nutr.* **2004**, *134*, 489; d) H. Sun, F. Meng, R. Cheng, C. Deng, Z. Zhong, *Antioxid. Redox Signaling* **2014**, *21*, 755.
- [4] a) H. Sun, F. Meng, R. Cheng, C. Deng, Z. Zhong, *Expert Opin. Drug Delivery* **2013**, *10*, 1109; b) F. Meng, W. E. Hennink, Z. Zhong, *Biomaterials* **2009**, *30*, 2180; c) R. Cheng, F. Feng, F. Meng, C. Deng, J. Feijen, Z. Zhong, *J. Controlled Release* **2011**, *152*, 2.
- [5] a) H. F. Gilbert, *Methods Enzymol.* **1995**, *251*, 8; b) S. Raina, D. Missiakas, *Annu. Rev. Microbiol.* **1997**, *51*, 179.
- [6] a) C. Yang, N. Panwar, Y. Wang, B. Zhang, M. Liu, H. Toh, H. S. Yoon, S. C. Tjin, P. H. J. Chong, W.-C. Law, C.-K. Chen, K.-T. Yong, *Nanoscale* **2016**, *8*, 9405; b) G. Lin, C.-K. Chen, F. Yin, C. Yang, J. Tian, T. Chen, G. Xu, C. He, M. C.-M. Lin, J. Wang, F. Lu, X. Wang, K.-T. Yong, *J. Mater. Chem. B* **2017**, *5*, 3327.
- [7] a) S. A. M. Ali, S. P. Zhong, P. J. Doherty, D. F. Williams, *Biomaterials* **1993**, *14*, 648; b) G. G. Pitt, M. M. Gratzl, G. L. Kimmel, J. Surles, A. Sohindler, *Biomaterials* **1981**, *2*, 215; c) H. Sun, L. Mei, C. Song, X. Cui, P. Wang, *Biomaterials* **2006**, *27*, 1735.
- [8] a) J. E. Zuckerman, M. E. Davis, *Nat. Rev. Drug Discovery* **2015**, *14*, 843; b) R. Kanasty, J. R. Dorkin, A. Vegas, D. Anderson, *Nat. Mater.* **2013**, *12*, 967; c) Y.-C. Tseng, S. Mozumdar, L. Huang, *Adv. Drug Delivery Rev.* **2009**, *61*, 721; d) M. E. Davis, J. E. Zuckerman, C. H. J. Choi, D. Seligson, A. Tolcher, C. A. Alabi, Y. Yen, J. D. Heidel, A. Ribas, *Nature* **2010**, *464*, 1067; e) X. Xu, J. Wu, Y. Liu, M. Yu, L. Zhao, X. Zhu, S. Bhasin, Q. Li, E. Ha, J. Shi, O. C. Farokhzad, *Angew. Chem., Int. Ed.* **2016**, *55*, 7091; f) X. Xu, J. Wu, Y. Liu, P. E. Saw, W. Tao, M. Yu, H. Zope, M. Si, A. Victorious, J. Rasmussen, D. Ayyash, O. C. Farokhzad, J. Shi, *ACS Nano* **2017**, *11*, 2618; g) Y. D. Yao, T. M. Sun, S. Y. Huang, S. Dou, L. Lin, J. N. Chen, J. B. Ruan, C. Q. Mao, F. Y. Yu, M. S. Zeng, J. Y. Zang, Q. Liu, F. X. Su, P. Zhang, J. Lieberman, J. Wang, E. Song, *Sci. Transl. Med.* **2012**, *4*, 130r48.
- [9] a) H. J. Kim, M. Oba, F. Pittella, T. Nomoto, H. Cabral, Y. Matsumoto, K. Miyata, N. Nishiyama, K. Kataoka, *J. Drug Targeting* **2012**, *20*, 33; b) K. Wang, Q. Hu, W. Zhu, M. Zhao, Y. Ping, G. Tang, *Adv. Funct. Mater.* **2015**, *25*, 3380; c) S. An, D. He, E. Wagner, C. Jiang, *Small* **2015**, *11*, 5142.
- [10] a) J. Li, X. Yu, Y. Wang, Y. Yuan, H. Xiao, D. Cheng, X. Shuai, *Adv. Mater.* **2014**, *26*, 8217; b) Y. Zou, M. Zheng, W. Yang, F. Meng, K. Miyata, H. J. Kim, K. Kataoka, Z. Zhong, *Adv. Mater.* **2017**, *29*, 1703285.
- [11] J. Wu, L. Zhao, X. Xu, N. Bertrand, W. I. Choi, B. Yameen, J. Shi, V. Shah, M. Mulvale, J. L. MacLean, O. C. Farokhzad, *Angew. Chem., Int. Ed.* **2015**, *54*, 9218.
- [12] a) X. Liu, H. Gong, K. Huang, *Cancer Sci.* **2013**, *104*, 651; b) P. Exertier, S. Javerzat, B. Wang, M. Franco, J. Herbert, N. Platonova, M. Winandy, N. Pujol, O. Nivelles, S. Ormenese, V. Godard, J. Becker, R. Bicknell, R. Pineau, J. Wilting, A. Bikfalvi, M. Hagedorn, *Oncotarget* **2013**, *4*, 2302; c) O. Rath, F. Kozielski, *Nat. Rev. Cancer* **2012**, *12*, 527; d) M. Venere, C. M. Horbinski, J. F. Crish, X. Jin, A. Vasanji, J. Major, A. Burrows, C. Chang,

- J. Prokop, Q. Wu, P. A. Sims, P. Canoll, M. K. Summers, S. S. Rosenfeld, J. N. Rich, *Sci. Transl. Med.* **2015**, 7, 304ra143.
- [13] a) D. M. Miller, S. D. Thomas, A. Islam, D. Muench, K. Sedoris, *Clin. Cancer Res.* **2012**, 18, 5546; b) J. A. Nilsson, J. L. Cleveland, *Oncogene* **2003**, 22, 9007; c) Z. E. Stine, Z. E. Walton, B. J. Altman, A. L. Hsieh, C. V. Dang, *Cancer Discovery* **2015**, 5, 1024.
- [14] a) C. M. Koh, C. J. Bieberich, C. V. Dang, W. G. Nelson, S. Yegnasubramanian, A. M. De Marzo, *Genes Cancer* **2010**, 1, 617; b) G. K. Hubbard, L. N. Mutton, M. Khalili, R. P. McMullin, J. L. Hicks, D. Bianchi-Frias, L. A. Horn, I. Kulac, M. S. Moubarek, P. S. Nelson, S. Yegnasubramanian, A. M. De Marzo, C. J. Bieberich, *Cancer Res.* **2016**, 76, 283.
- [15] a) G. Casinelli, J. LaRosa, M. Sharma, E. Cherok, S. Banerjee, M. Branca, L. Edmunds, Y. Wang, S. Sims-Lucas, L. Churley, S. Kelly, M. Sun, D. Stolz, J. A. Graves, *Cell Death Discovery* **2016**, 2, 16082; b) S. Pyndiah, S. Tanida, K. M. Ahmed, E. K. Cassimere, C. Choe, D. Sakamuro, *Sci. Signaling* **2011**, 4, ra19.
- [16] X. Zhu, Y. Xu, L. M. Solis, W. Tao, L. Wang, C. Behrens, X. Xu, L. Zhao, D. Liu, J. Wu, N. Zhang, I. I. Wistuba, O. C. Farokhzad, B. R. Zetter, J. Shi, *Proc. Natl. Acad. Sci. USA* **2015**, 112, 7779.
- [17] X. Xu, K. Xie, X.-Q. Zhang, E. M. Pridgen, G. Y. Park, D. S. Cui, J. Shi, J. Wu, P. W. Kantoff, S. J. Lippard, R. Langer, G. C. Walker, O. C. Farokhzad, *Proc. Natl. Acad. Sci. USA* **2013**, 110, 18638.
- [18] Z. Yang, J. Cao, Y. He, J. H. Yang, T. Kim, X. Peng, J. S. Kim, *Chem. Soc. Rev.* **2014**, 43, 4563.
- [19] a) J. D. Gregory, *J. Am. Chem. Soc.* **1955**, 77, 3922; b) S. Bhuniya, S. Maiti, E. J. Kim, H. Lee, J. L. Sessler, K. S. Hong, J. S. Kim, *Angew. Chem., Int. Ed.* **2014**, 53, 4469; c) X. D. Xu, Y. J. Cheng, J. Wu, H. Cheng, S. X. Cheng, R. X. Zhuo, X. Z. Zhang, *Biomaterials* **2016**, 76, 238.
- [20] a) K. Knop, R. Hoogenboom, D. Fischer, U. S. Schubert, *Angew. Chem., Int. Ed.* **2010**, 49, 6288; b) X. Xu, P. E. Saw, W. Tao, Y. Li, X. Ji, M. Yu, M. Mahmoudi, J. Rasmussen, D. Ayyash, Y. Zhou, O. C. Farokhzad, J. Shi, *Nano Lett.* **2017**, 17, 4427.

# Characterization of novel cell lines derived from a MYC-driven murine model of lethal metastatic adenocarcinoma of the prostate

Mark C. Markowski MD, PhD<sup>1</sup>  | Gretchen K. Hubbard PhD<sup>2</sup> |  
Jessica L. Hicks MS<sup>2</sup> | Qizhi Zheng MD<sup>2</sup> | Alexia King BS<sup>2</sup> | David Esopi BS<sup>1</sup> |  
Apurv Rege MS<sup>3</sup> | Srinivasan Yegnasubramanian MD, PhD<sup>1</sup> |  
Charles J. Bieberich MD<sup>3</sup> | Angelo M. De Marzo MD, PhD<sup>1,2,4</sup>

<sup>1</sup> Department of Oncology, Sidney Kimmel Comprehensive Cancer Center at Johns Hopkins, Baltimore, Maryland

<sup>2</sup> Department of Pathology, Johns Hopkins University School of Medicine, Baltimore, Maryland

<sup>3</sup> Department of Biological Sciences, University of Maryland Baltimore County, Baltimore, Maryland

<sup>4</sup> Department of Urology, Johns Hopkins University School, Baltimore, Maryland

## Correspondence

Mark C. Markowski, MD, PhD, Department of Oncology, Sidney Kimmel Cancer Center CRB I, Room 1M87, 1650 Orleans St. Baltimore, MD 21287.  
Email: mmarko12@jhmi.edu

## Funding information

Prostate Cancer Foundation, Grant numbers: Challenge Award, Young Investigator Award; Congressionally Directed Medical Research Programs, Grant numbers: W81XWH-15-1-0432, W81XWH-15-1-0729; American Society of Clinical Oncology, Grant number: Young Investigator Award; National Cancer Institute, Grant numbers: P30 CA006973, P50 CA058236, R01 CA183965, U01 CA196390; Patrick C. Walsh Prostate Cancer Research Fund

**Background:** Loss or mutation of *PTEN* alleles at 10q23 in combination with 8q24 amplification (encompassing *MYC*) are common findings in aggressive, human prostate cancer. Our group recently developed a transgenic murine model of prostate cancer involving prostate-specific *Pten* deletion and forced expression of *MYC* under the control of the *Hoxb13* promoter. *MYC* overexpression cooperated with *Pten* loss to recapitulate lethal, human prostate cancer.

**Method:** We now report on the generation of two mouse prostate cancer cell lines, BMPC1 and BMPC2, derived from a lymph node, and liver metastasis, respectively.

**Results:** Both cell lines demonstrate a phenotype consistent with adenocarcinoma and grew under standard tissue culture conditions. Androgen receptor (AR) protein expression is minimal (BMPC1) or absent (BMPC2) consistent with AR loss observed in the BMPC mouse model of invasive adenocarcinoma. Growth in media containing charcoal-stripped serum resulted in an increase in AR mRNA in BMPC1 cells with no effect on protein expression, unless androgens were added, in which case AR protein was stabilized, and showed nuclear localization. AR expression in BMPC2 cells was not effected by growth media or treatment with androgens. Treatment with an anti-androgen/castration or androgen supplemented media did not affect in vitro or in vivo growth of either cell line, irrespective of nuclear AR detection.

**Discussion:** These cell lines are a novel model of androgen-insensitive prostatic adenocarcinoma driven by *MYC* over-expression and *Pten* loss.

## KEYWORDS

AR indifferent, mouse model, prostate cancer

## 1 | BACKGROUND

Prostate cancer is the most common epithelial malignancy in men and second leading cause of cancer-related death.<sup>1</sup> The genomic and molecular pathogenesis of prostate cancer is complex, making it

difficult to differentiate lethal from more indolent forms of the disease.<sup>2–6</sup> Frequent copy number alterations are found during prostate cancer carcinogenesis including loss of chromosome 8p (NKX3.1), amplification of 8q24 (MYC), and deletion of *PTEN* on chromosome 10q23.<sup>7–9</sup> Loss of *PTEN* occurs in approximately 50% of lethal prostate cancers and has been shown in multiple studies to be linked to disease aggressiveness and prostate cancer specific death.<sup>10–15</sup> Similarly, amplification of the *MYC* locus has been correlated with poor outcomes and disease recurrence after prostatectomy.<sup>16–18</sup> Patients whose tumors harbored concurrent *MYC* amplification and *PTEN* loss were at increased the risk of prostate cancer specific mortality suggesting that the combination of both genetic events may cooperatively drive aggressive disease.<sup>19</sup>

The development of mouse models which recapitulate human prostate cancer has been limited due to absence of metastatic disease, atypical histologic features (ie, neuroendocrine or sarcomatoid phenotype), lack of genomic instability, or the use of driver genes rarely altered genetically in human prostate cancer.<sup>20,21</sup> In prior studies, loss of both *Pten* alleles or activation of *MYC* alone in the mouse prostate resulted in PIN and early invasive carcinoma with rare instances of metastatic disease.<sup>20</sup> In the Z-MYC model, prostate-specific overexpression of *MYC* resulted in low-grade PIN, but invasive carcinomas were observed only upon deletion of one or both *Pten* alleles suggestive of a potential cooperative effect of *Pten* loss and *MYC* activation.<sup>22</sup> This genetically engineered model did not result in widespread metastatic disease and genetic instability was not examined.

Recently, our group developed a mouse model (referred to as BMPC) that undergoes forced overexpression of *MYC* and deletion of both copies of *Pten* in the mouse prostate using *Hoxb13* transcriptional control elements.<sup>23</sup> These mice invariably develop lethal metastatic castration resistant prostatic adenocarcinomas that recapitulate key histopathologic and phenotypic (eg, activation of Akt) features of human prostate cancer initiation and progression.<sup>23</sup> In BMPC mice, metastatic sites of disease include lymph node involvement, with less frequent lung, and liver dissemination. Although very rare, bone metastases have also been observed, similar to human prostate cancer. Importantly, the prostate cancers that develop in the BMPC mice have widespread genome copy number alterations, a feature that is reminiscent of human disease, and not recapitulated in most other well-studied prostate cancer mouse models.<sup>23–27</sup> For instance, one of the only other mouse models demonstrating genomic instability required forced telomere shortening in the context of *Tp53* and *Pten* deletion.<sup>28</sup> However, mice with combined *Tp53* and *Pten* deletion commonly develop invasive prostatic tumors with sarcomatoid differentiation rather than adenocarcinoma.<sup>20</sup> The primary and metastatic carcinomas in the BMPC mice lack both neuroendocrine and sarcomatoid differentiation, features uncommon in untreated, human prostate cancers. The use of commonly altered driver genes in the human disease, the kinetics of disease initiation and progression, the metastases to relevant physiological sites, and the emergence of genetic instability in this model provide an opportunity to test new therapeutic strategies to prevent and treat lethal forms of human prostate cancer.<sup>23</sup>

To extend the utility of the BMPC model, in the present study we generated two mouse cell lines (BMPC1 and BMPC2) from metastatic sites of prostate cancer. The BMPC1 cell line was derived from prostate adenocarcinoma identified in a pelvic lymph node of a BMPC mouse. A liver metastasis served as the parental source for the BMPC2 cell line. Herein, we present an initial phenotypic characterization, along with a traditional karyotype and in vitro and in vivo growth conditions, including the influence of androgens, of these novel murine cell lines.

## 2 | METHODS

### 2.1 | Reagents

BMPC1, BMPC2, and MYC-CaP cells were routinely cultured in Dulbecco modified Eagle medium (DMEM) (Corning Inc., Corning, NY) supplemented with 10% Fetal Bovine Serum (FBS) (Gemini Bio-Products, Sacramento, CA) at 37°C in 5% CO<sub>2</sub>. PC3 cells were cultured under similar conditions in RPMI media. Ten percent Charcoal-stripped Calf Serum (CCS) (Gemini Bio-Products) supplemented media was used in select experiments. Enzalutamide and R1881 were purchased via Selleck Chemicals (Houston, TX) and Sigma-Aldrich (St. Louis, MO), respectively.

### 2.2 | Quantitative reverse transcriptase PCR (RT-PCR)

Total RNA was extracted using a Qiagen RNeasy mini kit, as described in the manufacturers protocol. RNA was treated with DNase I (RNase-free; Ambion, Waltham, MA) and cDNA synthesis was performed using the SuperScript First Strand Synthesis System for RT-PCR (Invitrogen, Carlsbad, CA) following standard protocol for “First-Strand Synthesis Using Random Primers.” Quantitative PCR was performed with SYBR Green Supermix (Bio-Rad, Hercules, CA). Mouse AR primers were purchased (RT2 qPCR Primer Assay, Qiagen, Hilden, Germany). Confirmation of AR RT-PCR results were confirmed with an alternative pair of primers for mouse AR (Forward (5′ to 3′)-GAATTCGGTGAAGC-TACAGACAAG; Reverse (5′ to 3′)-AGCTGCTCTCAGGGTGGCCCTCGGA). GAPDH was used as a housekeeping gene for normalization (Forward (5′ to 3′) –CGACTTCAACAGCAACTCCCACTCTTCC; Reverse (5′ to 3′)-TGGGTGGTCCAGGGTTTCTTACTCCTT). The fold differences in expression levels of AR in BMPC1 and BMPC2 cells were determined using the  $\Delta\Delta C_t$  method, relative to GAPDH. Statistical analysis comparing mean fold change (samples run in triplicate) in AR mRNA was performed using a paired, two-tailed *t*-test. *P* values <0.05 were considered statistically significant.

### 2.3 | Immunohistochemistry

Antigen unmasking was performed by steaming in high-temperature target retrieval solution (Target Retrieval Solution; Dako, Santa Clara, CA) for 50 min (p63, CK5, FOXA2) or in EDTA for 45 min (FOXA1, PTEN, c-MYC, AR, Nkx3.1) or in Citrate for 25 min (CK18).

Immunohistochemistry analysis was performed using antibodies that include: rabbit anti-human CK18 antibody (Novus, Littleton, CO, Cat# NB100-91844; 1:400 dilution), rabbit anti-human p63 antibody (Cell Signaling, Danvers, MA, D2K8X XP, Cat# 13109; 1:400 dilution), rabbit anti-human PTEN antibody (Cell Signaling, D4.3 XP, Cat # 9188; 1:200 dilution), rabbit anti human CK5 antibody (Covance, Princeton, NJ, Cat # MK5; 1:15000 dilution), rabbit anti-human FOXA2 antibody (Abcam, Cambridge, United Kingdom, Cat #; 1:400 dilution), rabbit anti-human FOXA1 antibody (Abcam, Cat # 23738; 1:600 dilution), rabbit anti-human Vimentin antibody (Cell Signaling, D21H3 XP, Cat # 5741; 1:6000), mouse anti-human smooth muscle actin (Agilent, Santa Clara, CA, M085129; 1:4000 dilution), rabbit anti-human c-MYC antibody (Abcam, Cat # 32072; 1:600 dilution), mouse anti-human Chromogranin A (Millipore Sigma, Burlington, MA, Cat # MAB5268; 1:8000 dilution), rabbit anti-human AR antibody (Cell Signaling, D6F11 XP, Cat #: 5153; 1:400 dilution), rabbit anti-mouse Nkx3.1 antibody (generous gift of Charles Bieberich [UMBC]; 1:3,000 dilution).

## 2.4 | RNA in situ hybridization

Chromogenic RNA in situ hybridization was performed by using ACD RNAscope 2.0 Brown assays with ACD target probes: Mm-AR (Cat# 316991), or Mm-NKx3-1 (Cat# 472111) or Mm-Hoxb13 (Cat# 434821) or Mm-Terc (Cat# 425201) or Mm-45S (Cat# 417331) or Hs-MYC (Cat# 311761). All hybridization and incubation steps were performed using the complete HybEZ Hybridization System following the manufacturer's protocol.

## 2.5 | Generation of BMPC cell lines

Two BMPC male mice with advanced, metastatic prostate cancer were euthanized. A palpable pelvic lymph node (mouse one) and an ~5 mm liver metastasis (mouse two) were harvested. After tissue disruption using a Miltenyi gentleMACS dissociator, cells were plated in T75 flasks in Dulbecco's modified Eagle's medium (DMEM) plus 20% FBS in the presence of antibiotics. Upon confluence, cells were passaged as a bulk tumor cell population and frozen at each passage. The bulk populations from both the liver and lymph node metastases continued robust growth beyond passage. Cells were then plated to single cell density in 100 mm culture dishes (Corning) in DMEM supplemented with 10% FBS until individual colonies were visualized. Cell media was then aspirated and discarded. Using sterilized, cloning cylinders (Corning) with silicone grease, individual colonies were isolated, and harvested using 0.25% trypsin. Cells were transferred into a six-well plate containing DMEM +10% FBS and subsequently passaged into T75 flasks. This process was carried out for cells derived from both lymph node and liver metastases. Five clones of each BMPC1 and BMPC2 were expanded in cell culture media. MYC/PTEN protein expression as well as Nkx3.1 and AR mRNA were measured and found to be comparable between individual clones. One clone of each cell line was chosen for further analysis. The clonal cell lines were named BMPC1 (lymph node metastasis) and BMPC2 (Liver metastasis). BMPC1 and BMPC2 cells were routinely cultured in 10% FBS supplemented media. Cell growth remained consistent through

multiple passages (>60) without senescence. Aliquots of early passage cells were stored in liquid nitrogen for future use. The generation of FFPE cell plugs was as described.<sup>29</sup>

## 2.6 | Cell growth assay

PC3 (500 cells/well), MYC-CaP (1000 cells/well), BMPC1 (500 cells/well), BMPC2 (500 cells/well) were plated in 48-well plates (Corning) containing media supplemented with 10% FBS. After 24 h, the cells were treated as indicated and grown under normal tissue culture conditions. Cell count and confluence was measured using live imaging software (IncuCyte ZOOM Live-Cell Analysis, Essen BioScience).

## 2.7 | Western blotting

Cells were plated in T75 flasks to 75% confluence in media containing 10% FBS. Prior to treatment with R1881 (Sigma-Aldrich), the media was replaced with a 10% CCS supplemented media for 48 h. R1881 was added to a final concentration of 1 nM or 10 nM for 24 h. Protein extracts were collected in RIPA buffer (50 mM Tris-HCl [pH 7.4], 150 mM NaCl, 1 mM EDTA, 1% [v/v] Triton X-100, 1% [w/v] sodium deoxycholate, One percent [w/v] Sodium dodecyl sulfate [SDS]) with protease inhibitors (Complete Mini, Roche, Switzerland). Western blot analysis was performed using the following antibodies: rabbit anti-human AR 1:1000 (Cell Signaling), mouse monoclonal anti-human beta-actin 1:1000 (Sigma). Membranes were revealed with HRP-linked goat anti-rabbit IgG 1:2000 (Cell Signaling) or horse anti-mouse IgG 1:2000 (Cell Signaling) using SuperSignal West Femto Maximum Sensitivity Substrate (Thermo Fisher Scientific, Waltham, MA).

## 2.8 | Allograft/in vivo growth

Twenty five ~42 days old male homozygous athymic nude mice (CrI: NU[NCr]-FOX1<sup>nu</sup>) from Charles river (Wilmington, MA) were acquired. The mice were allowed to acclimatize for seven days. PCR-based mouse and human pathogen testing on BMPC1 cells was negative (IMPACT I testing was performed which included: Ectromelia, EDIM, Hantaan, K virus, LCMV, LDEV, MAV1, MAV2, mCMV, MHV, MNV, MPV, MTV, MVM, Mycoplasma pulmonis, Mycoplasma sp., Polyoma, PVM, REO3, Sendai, TMEV. IXEDD Bioresearch, www.idexxbioresearch.com. A total of 100  $\mu$ L ( $10^6$  cells) BMPC1 cell suspension in DMEM media was injected on the left flank of each mouse subcutaneously. The allograft tumors were measured every alternate day using digital calipers and allowed to grow to a volume greater than 200 mm<sup>3</sup> before being enrolled in the study. An unpaired, two-tailed *t*-test was used to compare across groups at each time point. *P* values <0.05 were considered statistically significant

## 2.9 | Mouse surgical procedures

To achieve sustained delivery, 5 $\alpha$ -dihydrotestosterone (DHT) was loaded into ~2 cm lengths of sterile medical grade silastic tubing (Corning, O.D. = 3.18 mm) and the tubing was sealed using medical grade adhesive.

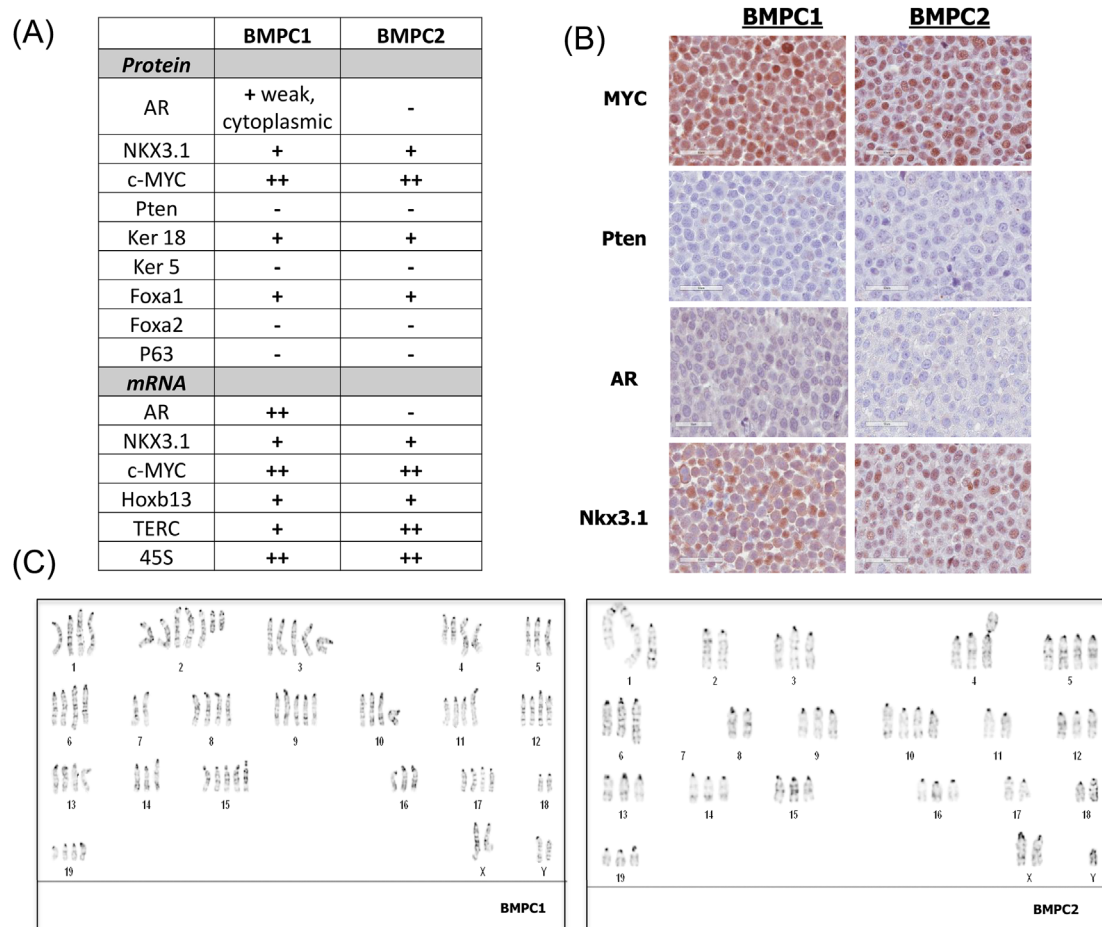


**FIGURE 1** Molecular and genetic characterization of murine cell lines, BMPC1 and BMPC2. A, Summary of IHC and RNAish staining results delineating tissue of origin and cell subtype. (- = negative, + = low, ++ = high). B, IHC staining of key proteins involved in prostate carcinogenesis and disease progression. ker 5, keratin 5; ker 18 is keratin 18. C, Standard karyotype of BMPC1 (top) and BMPC2 (bottom). [Color figure can be viewed at [wileyonlinelibrary.com](http://wileyonlinelibrary.com)]

Mice were anesthetized using intraperitoneal injection with Avertin. Once deep anesthesia had been achieved, a 5 mm incision was made perpendicular to the dorsal midline at the cervico-thoracic junction. Using blunt scissors, the skin and fascia were gently dissected from the underlying muscle to create a ~2 cm pocket extending posteriorly along the dorsal midline. Using sterile forceps, the silastic tubing was inserted into the subcutaneous pocket, and the incision was closed with 6-0 nylon suture. Animals were placed in a cage on a heating pad and monitored until they were ambulatory. The animals were then returned to the animal facility where they remained till the end of the study.

Twenty-one of the 25 mice injected developed allograft tumors, and the mice with tumors were then randomly assigned to five groups; Control (3), Sham castration (3), Castration (5), test vehicle (5), and test drug (5) (DHT), as their tumors reached the 200 mm<sup>3</sup> volume. The test vehicle group was implanted with empty silastic tubing whereas the test drug group was implanted with DHT filled silastic tubing. For castration and sham castration procedures mice were anesthetized using Avertin by intraperitoneal injection. Once deep anesthesia had been achieved the castration procedure was performed as described earlier by Yoo et al.<sup>30</sup> For sham castration the same procedure was performed but the testicles were not removed. Animals were placed in a cage on a heating pad and

monitored until they were ambulatory. The animals were provided with ibuprofen in drinking water for 48 h for post-operative analgesia.

### 3 | RESULTS

Each cell line was initially characterized for phenotype using immunohistochemistry (IHC) and RNA in situ hybridization (RNAish) (Figures 1A and 1B) on cells that were fixed in formalin and embedded into paraffin blocks (formalin fixed and paraffin embedded or FFPE). MYC mRNA and protein was uniformly detected at high levels whereas Pten protein was absent in both cell lines, consistent with the trigenic model. To confirm prostatic origin, we examined the expression of Nkx3.1, Hoxb13, and AR. Both BMPC1 and BMPC2 had detectable levels of Nkx3.1 mRNA and protein as well as Hoxb13 mRNA. AR protein was present at very low levels in both the cytoplasm and nucleus of BMPC1 cells. The weak AR staining observed in the BMPC1 cell line under normal tissue culture conditions did not show predominantly nuclear localization. BMPC2 cells did not have detectable levels of AR protein by IHC. AR mRNA was readily detected in BMPC1 cells (Figure 1A, Figure 2C) and was undetectable in BMPC2

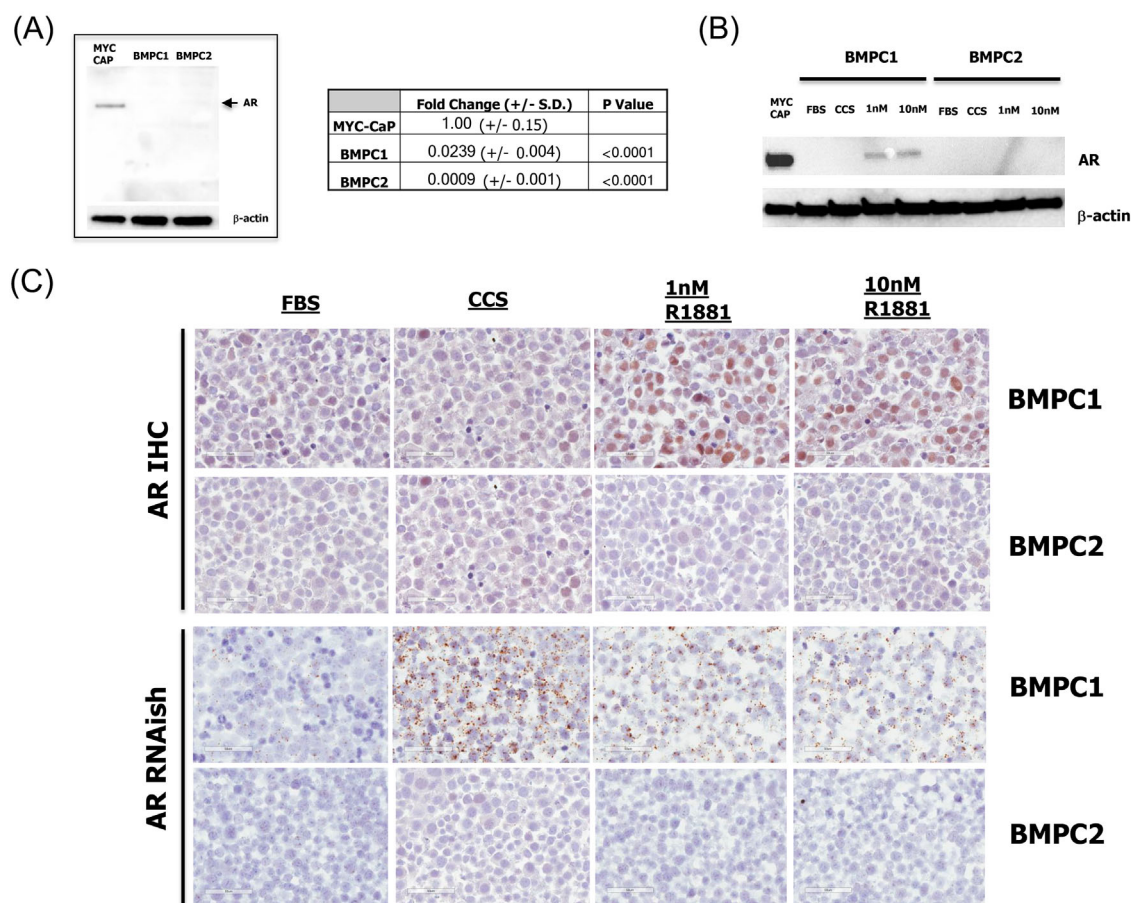


**FIGURE 2** AR mRNA and protein expression in BMPC1 and BMPC2 Cell Lines. A, Left—Western blot analysis of AR protein expression across MYC-CaP, BMPC1, and BMPC2 cell lines. Right—Quantitative mRNA of AR expression in BMPC1 and BMPC2 cell lines. BMPC1 and BMPC2 AR mRNA levels are reported as fold difference relative to the MYC-CaP cell line. B, BMPC1 and BMPC2 cell lines were treated with 1 nM or 10 nM R1881 for 24 h in charcoal stripped media. AR protein expression was measured by Western blot. B-actin levels are shown as a loading control. C, IHC staining and chromogenic RNAish for AR in BMPC1 and BMPC2 formalin fixed paraffin embedded cell plugs following treatment with R1881. [Color figure can be viewed at [wileyonlinelibrary.com](http://wileyonlinelibrary.com)]

cells. Epithelial markers (ie, keratin 18 and Foxa1) were positive across BMPC1 and BMPC2. Moreover, neuroendocrine markers (Foxa2 and chromogranin A) and stromal elements (vimentin and smooth muscle actin) were negative (Supplementary Figure S1). Also absent from both cell lines was the basal cell marker, P63.

Standard Giemsa stained karyotypes revealed highly abnormal chromosomal copy numbers with a modal number of 72–80 chromosomes and 52–102 chromosomes in the BMPC1 and BMPC2 cell lines, respectively. Numerous chromosomal aberrations including small fragments, chromosomal associations, and deletions were observed, with a higher tendency for such events in the BMPC2 cell line. Representative karyotypes of the BMPC1 and BMPC2 cells are shown in Figure 1C. Additional whole genomic characterizations will be presented separately.

We then further characterized AR expression and androgen responsiveness in both cell lines. Although AR protein was observed in BMPC1 cells at low levels via IHC, a band corresponding to the correct size of AR was not detected by western blot (Figure 2A, Left). We interpret this to indicate that IHC is more sensitive than the Western blotting when using whole cell lysates in the absence of AR enrichment (eg, by prior immunoprecipitation). To further validate that the IHC

staining is specific for AR protein, we stained a number of FFPE cell lines and human tissues with known AR status (Supplementary Figure S2). The known AR-negative cell lines PC3 and DU145 showed absence of AR immunoreactivity, while the known AR-positive cell lines LNCaP, VCaP, and CWR-22Rv1 showed strong immunoreactivity. Likewise, normal prostatic luminal, and stromal cells showed the expected strong immunoreactivity for AR. Using quantitative RT-PCR, BMPC1 had detectable levels of AR mRNA, but the levels were ~35–50x's fold lower than AR mRNA in the mouse line, MYC-CaP (Figure 2A, Right). Levels of AR mRNA in BMPC1 cells were significantly more than BMPC2, which was barely detectable by quantitative RT-PCR.

As BMPC1 cells expressed AR mRNA yet very little AR protein, which was not concentrated within nuclei, we hypothesized that AR protein in BMPC1 cells may be unstable and rapidly degraded in the absence of ligand. In an effort to stabilize AR protein and induce nuclear translocation, we treated BMPC1 cells with increasing doses of the synthetic androgen, R1881, following serum starvation. By Western blot, AR protein was detectable in the BMPC1 cell line following exposure to androgen (Figure 2B). Using IHC on FFPE cell pellets, we confirmed an R1881-induced increase in AR protein in

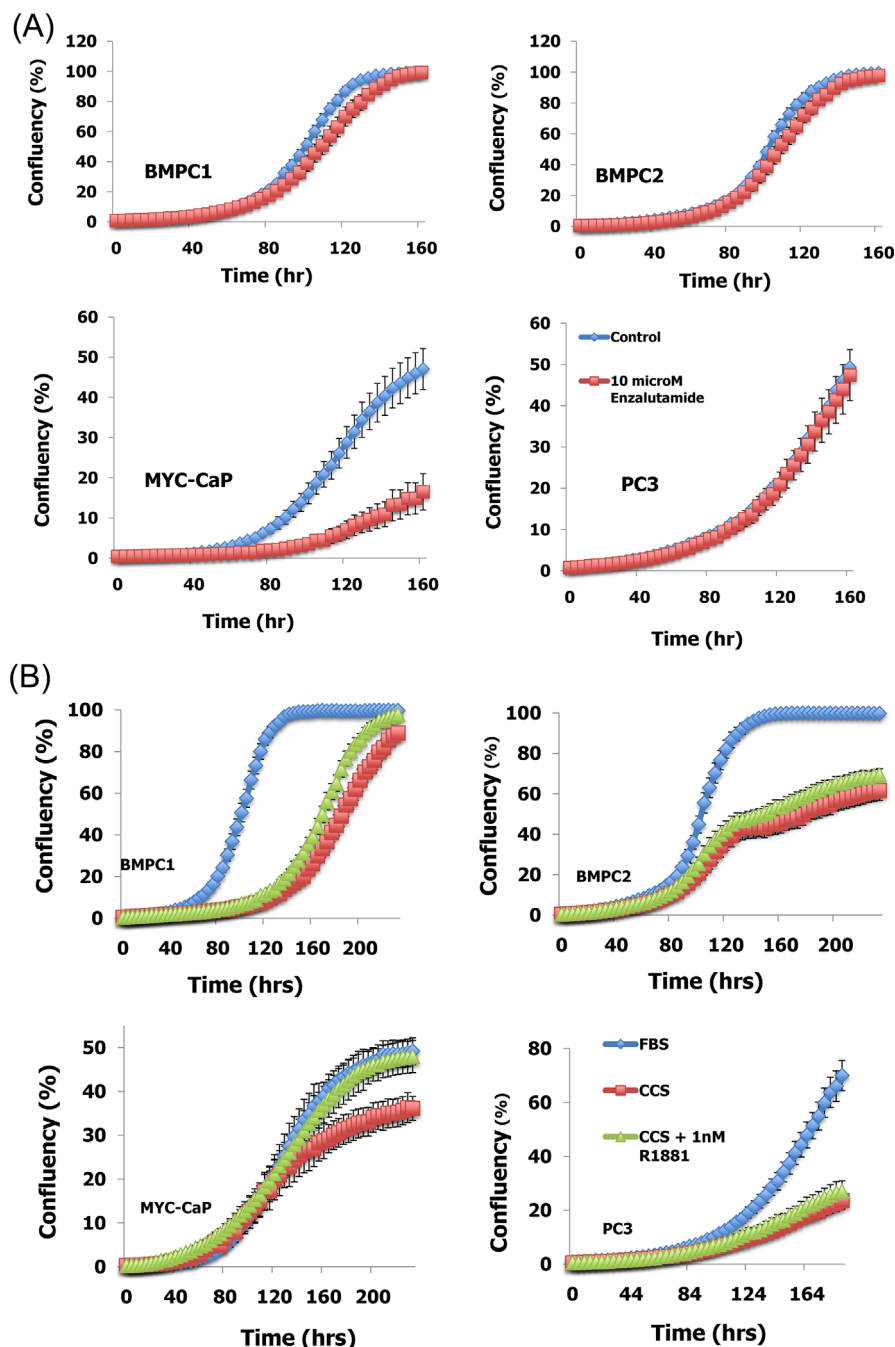


**FIGURE 3** Effect of R1881 and enzalutamide on BMPC1 and BMPC2 Cell Growth. Using Incucyte imaging software, cell growth (% confluency) was measured over a time course of up to 200 h following treatment with (A). Enzalutamide 10  $\mu$ M and (B) 1 nM and 10 nM R1881. Growth of BMPC1 and BMPC2 cell lines were not significantly affected by treatment with an anti-androgen or restoration of androgen. [Color figure can be viewed at [wileyonlinelibrary.com](http://wileyonlinelibrary.com)]

BMPC1 cells and observed nuclear translocation of the receptor (Figure 2C). At the mRNA level in BMPC1 cells, culture in media containing charcoal-stripped serum resulted in increased AR mRNA compared to full serum with no appreciable change in protein expression in the absence of R1881 (Figure 2C). The expression of *Nkx3.1*, a known prostate specific AR-responsive gene, was not effected by charcoal stripped media or the presence of R1881 (data not shown). No effect of charcoal stripped serum or addition of R1881

was observed on changes in AR protein or mRNA expression in the BMPC2 cell line.

Given the effect of R1881 on AR protein levels in BMPC1, we examined the effect of both R1881 supplementation and anti-androgen treatment in a series of in vitro growth experiments. We examined the cell growth of both BMPC1 and BMPC2 in the presence and absence of the anti-androgen, enzalutamide (Figure 3A). BMPC1 and BMPC2 cell growth was not affected by the addition of enzalutamide,

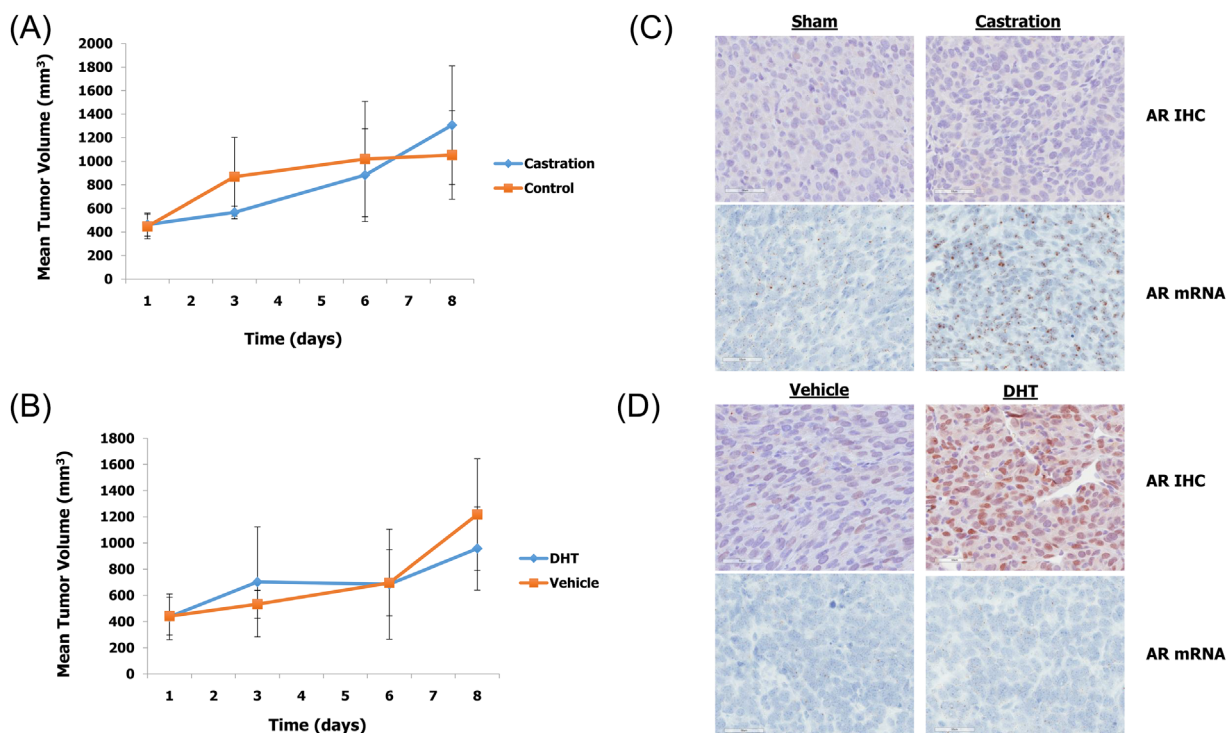


**FIGURE 4** In vivo effect of castration and DHT supplementation on BMPC1 allograft growth and AR expression in nude mice. Nude mice were inoculated with BMPC1 and grown to 500cc<sup>3</sup>. A, Mice underwent sham castration or castration and tumor volume was measured daily until euthanasia. No effect of castration was observed ( $P > 0.05$  across all time points). B, Empty or DHT-containing silastic tubing was placed subcutaneously in BMPC1 bearing nude mice. Tumor volume was measured daily until euthanasia. DHT did not increase allograft growth ( $P > 0.05$  across all time points). C, AR mRNA levels increased following castration. No change in AR protein was observed. D, AR protein levels were increased in the presence of DHT and localized to the nucleus. No change in AR mRNA was detected. [Color figure can be viewed at [wileyonlinelibrary.com](http://wileyonlinelibrary.com)]

comparable to the effect on the AR-negative, human prostate cancer cell line, PC3. As AR protein levels were stabilized in the presence of androgen, we sought to determine the growth effect of androgen supplementation. BMPC1 and BMPC2 cells were grown in media supplemented with charcoal stripped serum which reduced the growth of all cell lines tested, including PC3 (Figure 3B). The addition of 10 nM R1881 rescued the growth of the androgen-sensitive, mouse cell line, MYC-CaP, but did not affect the growth of BMPC1, BMPC2, or PC3 cells.

We next performed in vivo studies assessing the androgen responsiveness of the BMPC1 cell line in allografts in immunocompromised mice, given the in vitro increase of AR protein levels in the presence of R1881. BMPC1 allografts were allowed to grow in nude mice to a tumor volume of 500 mm<sup>3</sup> before initiating treatment. Initially, we evaluated BMPC1 allograft growth following castration. To control for an effect of iatrogenic stress, control animals underwent a sham castration. No significant effect on BMPC1 allograft growth was observed following castration ( $n = 5$ ) over an 8-day time course compared to the sham control ( $n = 3$ ) (Figure 4A). Since AR protein was stabilized in the presence of the AR agonist in our in vitro studies, we measured BMPC1 allograft growth after the addition of DHT. Silastic tubing containing DHT ( $n = 5$ ) or blank tubing ( $n = 5$ ) was placed subcutaneously in the tumor-bearing mice on Day 0. No significant difference in BMPC1 allograft volume was observed between either group, similar to the results of the castration experiment (Figure 4B). At necropsy, BMPC1 allografts from the DHT and castration

experiments were formalin-fixed and paraffin embedded for further study of AR expression. Following castration, AR mRNA levels in the allografts increased relative to both control (no surgery) and sham specimens (Figure 4C). IHC staining for AR protein remained virtually undetectable irrespective of castration status. Mice that harbored DHT-containing or blank silastic tubing (which were not castrated) had AR mRNA levels that did not change in the presence of DHT (Figure 4D). As in the cell lines treated with R1881 in vitro, AR protein was readily detected in BMPC-1 allografts from DHT-treated mice and located in the nucleus. No effect of castration or DHT supplementation was observed on Nkx3.1 expression.

## 4 | DISCUSSION

BMPC1 and BMPC2 cell lines were generated in a mouse model reliant on Hoxb13 transcriptional control elements, which direct gene expression in the prostate, and distal large intestine/rectum.<sup>31</sup> We confirmed the prostatic origin of both lines via detection of the prostate-specific homeodomain protein, Nkx3.1, as well as AR mRNA. In comparison to MYC-CaP cells, BMPC1 had significantly less AR mRNA and BMPC2 was negative by in situ hybridization, and slightly positive by RT-PCR. Whereas AR protein expression in BMPC2 was absent, BMPC1 make low levels of AR under normal growth

conditions, indicating heterogeneity for AR between lines. Similarly, in the BMPC model, AR expression was lost upon the development of invasive carcinoma consistent with the findings in both cell lines.<sup>23</sup> The dynamic interplay between AR expression/signaling and *Pten* loss in murine model of prostate cancer has been well established. Upon *Pten* loss or inactivation in luminal cells, the resulting activation of the Pi3k signaling pathway has been shown to negatively regulate AR expression and downstream signaling.<sup>32,33</sup> Interestingly, Pi3k inhibition did not result in increased AR expression in either BMPC1 or BMPC2 cells (unpublished observations). Loss of AR expression is relatively common in murine models of prostate cancer.<sup>20,34</sup>

We explored whether manipulating androgen levels would affect AR expression in these cell lines. Media supplemented with charcoal stripped media (ie, androgen depleted) resulted in increased AR mRNA in the BMPC1 cell line suggesting a negative, autoregulation of AR expression. Despite an increase in mRNA, no change in AR protein was observed. AR protein has been shown to be more stable in the presence of ligand prompting further investigation of the role of androgens on the posttranslational regulation of AR protein.<sup>35</sup> The addition of a synthetic androgen (R1881) increased the level of AR protein and resulted in nuclear localization in only the BMPC1 Line. We did not measure circulating testosterone levels in the intact, castrated, or DHT-supplemented mice which is an acknowledged weakness of this study. However, we speculate that circulating levels of androgens in the mouse models may not be sufficient to stabilize AR protein contributing to this loss. This hypothesis is supported by our in vivo data, which showed increased/stable AR protein levels in BMPC1 allografts following the implantation of DHT without a corresponding increase in mRNA. Castration of these mice lead to an increase in BMPC1 AR mRNA, but not protein, consistent with the in vitro findings. Testosterone levels in mice are decreased in the presence of disease states such as cancer, suggesting a possible mechanism for diminished AR expression in the BMPC, and other mouse models of prostate cancer.<sup>36</sup> In the absence of androgen in hormone sensitive prostate cancer cells (ie, LNCaP), AR protein is unstable leading to decreased levels, which is consistent with the BMPC1 in vitro model.<sup>37</sup>

Although AR protein can be stabilized and translocated to the nucleus, BMPC1 cell growth was not affected by the presence of R1881 or treatment with an anti-androgen. We also did not observe a change in *Nkx3.1* mRNA or protein levels in both the in vitro and in vivo experimental system in the presence of androgens. This suggests that AR, although present, is not transcriptionally active and/or significantly affecting cell growth. The mechanism for this phenomenon is unclear and may be related to the low levels of AR mRNA and protein at baseline. The term “androgen indifferent” prostate cancer has been coined by Aparicio and colleagues to describe a variant of prostate adenocarcinoma. This subtype of prostate cancer is characterized, in part, by absent or low levels of AR protein.<sup>38</sup> Such cancers typically have a short duration of response to hormonal therapies and may benefit from platinum based chemotherapy.<sup>39</sup> BMPC1 and BMPC2 may model AR-indifferent prostate cancer as demonstrated by a lack of sensitivity to androgen stimulation as well as exposure to an anti-androgen. These cell lines may then serve as

an in vitro tool for further study of a lethal subtype of prostate adenocarcinoma.

## ACKNOWLEDGMENTS

This work was partially supported by the Sidney Kimmel Comprehensive Cancer Center at Johns Hopkins NIH grant P30 CA006973, P50 CA058236, U01 CA196390, R01 CA183965 (SY), the Prostate Cancer Foundation Young Investigator Award (MCM), and Challenge Award (SY), Department of Defense W81XWH-15-1-0432 Postdoctoral Award (MCM), ASCO/CCF Young Investigator Award (MCM), and Department of Defense W81XWH-15-1-0729 Synergistic Idea Development Award (AMD). The Patrick C. Walsh Prostate Cancer Research Fund (AMD and CJB) The content is solely the responsibility of the authors and does not necessarily represent the official views of the National Cancer Institute or the National Institutes of Health.

## CONFLICTS OF INTEREST

All authors have no conflicts of interest to disclose.

## ORCID

Mark C. Markowski  <http://orcid.org/0000-0003-2780-5100>

## REFERENCES

1. Siegel RL, Miller KD, Jemal A. Cancer statistics. *CA Cancer J Clin*. 2016;66:7–30.
2. Taylor BS, Schultz N, Hieronymus H, et al. Integrative genomic profiling of human prostate cancer. *Cancer Cell*. 2010;18:11–22.
3. Grasso CS, Wu YM, Robinson DR, et al. The mutational landscape of lethal castration-resistant prostate cancer. *Nature*. 2012;487:239–243.
4. Berger MF, Lawrence MS, Demicheli F, et al. The genomic complexity of primary human prostate cancer. *Nature*. 2011;470:214–220.
5. Schrecengost R, Knudsen KE. Molecular pathogenesis and progression of prostate cancer. *Semin Oncol*. 2013;40:244–258.
6. Cancer genome atlas research N. the molecular taxonomy of primary prostate cancer. *Cell*. 2015;163:1011–1025.
7. Wang SI, Parsons R, Ittmann M. Homozygous deletion of the PTEN tumor suppressor gene in a subset of prostate adenocarcinomas. *Clin Cancer Res*. 1998;4:811–815.
8. Jenkins RB, Qian J, Lieber MM, Bostwick DG. Detection of c-myc oncogene amplification and chromosomal anomalies in metastatic prostatic carcinoma by fluorescence in situ hybridization. *Cancer Res*. 1997;57:524–531.
9. Visakorpi T, Kallioniemi AH, Syvanen AC, et al. Genetic changes in primary and recurrent prostate cancer by comparative genomic hybridization. *Cancer Res*. 1995;55:342–347.
10. McMenamin ME, Soung P, Perera S, Kaplan I, Loda M, Sellers WR. Loss of PTEN expression in paraffin-embedded primary prostate cancer correlates with high Gleason score and advanced stage. *Cancer Res*. 1999;59:4291–4296.
11. Lotan TL, Gurel B, Sutcliffe S, et al. PTEN protein loss by immunostaining: analytic validation and prognostic indicator for a high risk surgical cohort of prostate cancer patients. *Clin Cancer Res*. 2011;17:6563–6573.

12. Yoshimoto M, Cunha IW, Coudry RA, et al. FISH analysis of 107 prostate cancers shows that PTEN genomic deletion is associated with poor clinical outcome. *Br J Cancer*. 2007;97:678–685.
13. Reid AH, Attard G, Ambrosine L, et al. Molecular characterisation of ERG, ETV1 and PTEN gene loci identifies patients at low and high risk of death from prostate cancer. *Br J Cancer*. 2010;102:678–684.
14. Cuzick J, Yang ZH, Fisher G, et al. Prognostic value of PTEN loss in men with conservatively managed localised prostate cancer. *Br J Cancer*. 2013;108:2582–2589.
15. Ahearn TU, Pettersson A, Ebot EM, et al. Aprospective investigation of PTEN loss and ERG expression in lethal prostate cancer. *J Natl Cancer Inst*. 2016;108:1–9.
16. Fromont G, Godet J, Peyret A, et al. 8q24 amplification is associated with Myc expression and prostate cancer progression and is an independent predictor of recurrence after radical prostatectomy. *Hum Pathol*. 2013;44:1617–1623.
17. Sato K, Qian J, Slezak JM, et al. Clinical significance of alterations of chromosome 8 in high-grade, advanced, nonmetastatic prostate carcinoma. *J Natl Cancer Inst*. 1999;91:1574–1580.
18. Ribeiro FR, Henrique R, Martins AT, Jeronimo C, Teixeira MR. Relative copy number gain of MYC in diagnostic needle biopsies is an independent prognostic factor for prostate cancer patients. *Eur Urol*. 2007;52:116–125.
19. Liu W, Xie CC, Thomas CY, et al. Genetic markers associated with early cancer-specific mortality following prostatectomy. *Cancer*. 2013;119:2405–2412.
20. Ittmann M, Huang J, Radaelli E, et al. Animal models of human prostate cancer: the consensus report of the New York meeting of the Mouse Models of Human Cancers Consortium Prostate Pathology Committee. *Cancer Res*. 2013;73:2718–2736.
21. Irshad S, Abate-Shen C. Modeling prostate cancer in mice: something old, something new, something premalignant, something metastatic. *Cancer Metastasis Rev*. 2013;32:109–122.
22. Kim J, Eltoum IE, Roh M, Wang J, Abdulkadir SA. Interactions between cells with distinct mutations in c-MYC and Pten in prostate cancer. *PLoS Genet*. 2009;5:e1000542.
23. Hubbard GK, Mutton LN, Khalili M, et al. Combined MYC activation and pten loss are sufficient to create genomic instability and lethal metastatic prostate cancer. *Cancer Res*. 2016;76: 283–292.
24. Williams JL, Greer PA, Squire JA. Recurrent copy number alterations in prostate cancer: an in silico meta-analysis of publicly available genomic data. *Cancer Genet*. 2014;207:474–488.
25. Sun J, Liu W, Adams TS, et al. DNA copy number alterations in prostate cancers: a combined analysis of published CGH studies. *Prostate*. 2007;67:692–700.
26. Hieronymus H, Schultz N, Gopalan A, et al. Copy number alteration burden predicts prostate cancer relapse. *Proc Natl Acad Sci USA*. 2014;111:11139–11144.
27. Bianchi-Frias D, Hernandez SA, Coleman R, Wu H, Nelson PS. The landscape of somatic chromosomal copy number aberrations in GEM models of prostate carcinoma. *Mol Cancer Res*. 2015;13:339–347.
28. Ding Z, Wu CJ, Jaskelioff M, et al. Telomerase reactivation following telomere dysfunction yields murine prostate tumors with bone metastases. *Cell*. 2012;148:896–907.
29. Holdhoff M, Guner G, Rodriguez FJ, et al. Absence of cytomegalovirus in glioblastoma and other high-grade gliomas by real-time PCR, immunohistochemistry, and In situ hybridization. *Clin Cancer Res*. 2017;23:3150–3157.
30. Yoo YE, Ko CP. Dihydrotestosterone ameliorates degeneration in muscle, axons and motoneurons and improves motor function in amyotrophic lateral sclerosis model mice. *PLoS ONE*. 2012;7:e37258.
31. McMullin RP, Mutton LN, Bieberich CJ. Hoxb13 regulatory elements mediate transgene expression during prostate organogenesis and carcinogenesis. *Dev Dyn*. 2009;238:664–672.
32. Carver BS, Chapinski C, Wongvipat J, et al. Reciprocal feedback regulation of PI3K and androgen receptor signaling in PTEN-deficient prostate cancer. *Cancer cell*. 2011;19:575–586.
33. Mulholland DJ, Tran LM, Li Y, et al. Cell autonomous role of PTEN in regulating castration-resistant prostate cancer growth. *Cancer Cell*. 2011;19:792–804.
34. Cho H, Herzka T, Zheng W, et al. RapidCaP, a novel GEM model for metastatic prostate cancer analysis and therapy, reveals myc as a driver of Pten-mutant metastasis. *Cancer Discov*. 2014;4: 318–333.
35. Zhou ZX, Lane MV, Kempainen JA, French FS, Wilson EM. Specificity of ligand-dependent androgen receptor stabilization: receptor domain interactions influence ligand dissociation and receptor stability. *Mol Endocrinol*. 1995;9:208–218.
36. Nelson JF, Latham KR, Finch CE. Plasma testosterone levels in C57BL/6J male mice: effects of age and disease. *Acta Endocrinol (Copenh)*. 1975;80:744–752.
37. Gregory CW, Johnson RT, Jr., Mohler JL, French FS, Wilson EM. Androgen receptor stabilization in recurrent prostate cancer is associated with hypersensitivity to low androgen. *Cancer Res*. 2001; 61:2892–2898.
38. Beltran H, Tomlins S, Aparicio A, et al. Aggressive variants of castration-resistant prostate cancer. *Clin Cancer Res*. 2014;20: 2846–2850.
39. Aparicio AM, Harzstark AL, Corn PG, et al. Platinum-based chemotherapy for variant castrate-resistant prostate cancer. *Clinical Cancer Res*. 2013;19:3621–3630.

## SUPPORTING INFORMATION

Additional supporting information may be found online in the Supporting Information section at the end of the article.

**How to cite this article:** Markowski MC, Hubbard GK, Hicks JL, et al. Characterization of novel cell lines derived from a MYC-driven murine model of lethal metastatic adenocarcinoma of the prostate. *The Prostate*. 2018; 78:992–1000. <https://doi.org/10.1002/pros.23657>